A New Surface Resistance Measurement Method with Ultrahigh Sensitivity

by

Changnian Liang

Dissertation submitted to the Faculty of the
Virginia Polytechnic Institute and State University
in partial fulfillment of the requirements for the degree of
DOCTOR OF PHILOSOPHY
in
Physics

APPROVED:

Ronald M. Sundelin

Ronald Sundelin, Chairman

Larry Phillips

Larry Phillips

David Jenkins

David Jenkins

Luke Mo

Luke Mo

Richard Zallen

Richard Zallen

May, 1993

Blacksburg, Virginia

A New Surface Resistance Measurement Method with Ultrahigh Sensitivity

by

Changnian Liang

Committee Chairman: Ronald Sundelin

Physics

(ABSTRACT)

A superconducting niobium triaxial cavity has been designed and fabricated to study residual surface resistance of planar superconducting materials. Unlike many other structures where the test samples are placed in strong magnetic field positions, the edge of a 25.4 mm or larger diameter sample in the triaxial cavity is located outside the strong field region. Therefore, the edge effects and possible losses between the thin film and the substrate have been minimized in this design, ensuring that the induced RF losses are intrinsic to the test material. The fundamental resonant frequency of the cavity is 1.5 GHz, the same as the working frequency of CEBAF cavities. The cavity has a compact size compared to its TE_{011} counterpart, which makes it more sensitive to the sample's loss.

For even higher sensitivity, a calorimetry method has been used to measure the RF losses on the superconducting sample. At 2 K, a 2 μK temperature change can be resolved by using carbon resistor sensors. The temperature distribution caused by RF heating is measured by 16 carbon composition resistor sensors. A 0.05 μW heating power can be detected at such a resolution, which translates to a surface resistance of 0.02 nΩ at a surface magnetic field of 52 Oe. This is the most sensitive device for surface resistance measurements to date. In addition, losses due to the indium seal, coupling probes, field emission sites other than the sample, and all of the high field resonator surfaces, are excluded in the measurement.

Surface resistance of both niobium and high-T_c superconducting thin films has been measured. A low R_s of 35.2 $\mu\Omega$ was measured for a 25.4 mm diameter $YBa_2Cu_3O_7$ thin film at 1.5 GHz and at 2 K. The measurement result is the first result for a large area epitaxially

grown thin film sample at such a low RF frequency, and it reflects the status of the thin film fabrication technology. The calorimetry method is proven to be an accurate, reliable, and ultra-sensitive method.

The abrupt disappearance of multipacting between two parallel plates has been observed and monitored with the 16 temperature mapping sensors. Field emission or some field dependent anomalous RF losses on the niobium plate have also been observed. These results confirm that the calorimetric measurement is a useful tool to study the field-limiting phenomena quantitatively.

Acknowledgements

I would first like to thank my thesis adviser, Ron Sundelin, for his guidance in my thesis research and his patience in making numerous corrections of my thesis writing. During the course of my study, I have benefited greatly from his rich background and deep insight in the SRF field and his attitude toward every piece of work, no matter little or big. From him, I have learned not only the detailed experimental skills in superconducting RF technology, but also the basic rules of scientific work. I am truly fortunate to have an advisor like him.

Without Larry Phillips, my second advisor, the thesis could not have become a reality. Larry not only helped me to start my project in every detail but also helped me to overcome many other problems in real life. His support was so precious to me because, as a newcomer to the capitalist system, I was totally confused in many minor things at the beginning of my research. He never let me feel discouraged regardless of what happened.

The third person I would like to thank is Larry Doolittle, a quasi-advisor and a friend who gave me many valuable interactive "pulses". Without him, my experience at CEBAF would have been much less exciting.

My accomplishment would have amounted to much less without the help from the following scientists. Peter Kneisel, who taught me the RF measurement techniques and shared with me his calorimetric measurement experience. His full support in allowing me to use his RF measurement equipment deserves my sincere thanks, since no one knew what would

result from use by an inexperienced user. My thanks also go to Ganapati Myneni for his help in cryogenic measurements, Viet Nguyen for his advice in many aspects, Charlie Reece for his support in arrangement of the equipment and the experiment, and Joe Susta for his assistance in scheduling the VTA activity. In addition, the experience of working with these people will be a valuable asset in my future profession.

Special thanks also go to Jay Benesch, Ricky Campisi, Fred Dylla, Kenji Saito, and Byung Yunn for their valuable support and discussions.

Getting help from technicians and engineers is quite a different experience, which I appreciated as well as enjoyed very much. It was Tom Elliott who helped me to learn many skills like machining, welding, etc. He has also been a faithful consultant for any kind of problem I have had during these years. Two other most patient and helpful teachers throughout these years are Bob Bennett and John Brawley. I have learned a great deal from them in developing my technical skills at work as well as in my understanding about daily experiences. In particular, John did a wonderful job in welding the triaxial niobium cavity, which is the central part of my thesis. Tom Powers laid out the printed circuit board of the scanning electronics for me, and Bruce Almeida, my officemate and friend, helped me very much in electronics and computer hardware.

My acknowledgement list also includes Frank Folsom and Sam Morgan for machining; Ralph Afanador, Jody Brock, Eric Hanson, and Brett Lewis for cryogenic operation; Jerry Pauley, Dan Riel, and Josh Strong for chemical treatment; Kevin Jordan, Peter Kushnick, and John Mammosser in RF setup; Larry Turlington for cavity machining; Charlie Hughes and Gary Dezern for welding; John Heckman for vacuum; and numerous favors from Jay Wall, Ning Luo, Mike Spata, Linda Summers, Jeff Mazyck, Henry Whitehead, Kathy Yopp, Jim Pace, Keith Finger, etc.

My sincere thanks also go to all the administrative staff at CEBAF. I have obtained very satisfactory assistance from the library, computer center, machine shop, and the finance

and procurement departments. Special thanks go to Julie Oyer, Lyn Wells, and Maria Thornton, who have done a great deal of administrative work for me during these years. So have Gayle Sundeen, Uni Brown, and many others.

Last and one of the most important things I want to mention is Dirk Walecka's class at CEBAF. I not only learned about the basic concepts and laws in physics but also acquired the confidence and courage to question as well as the motivation to find solutions. The style and organization of this thesis, in my opinion, has been influenced by his wonderful teaching of physics.

At Virginia Tech, I would like to thank my advisory committee members, David Jenkins, Luke Mo, and Richard Zallen. Their support and encouragement are valuable to this thesis. The help and friendship from Chris Thomas has been very important to me during these years. Her wonderful work and understanding have made my graduate student life, as well as that of other graduate students', much easier and more pleasant.

I would like to thank William DeSisto of Naval Research Laboratory and Ross Muenchausen of Los Alamos Natinoal Laboratory for providing me YBCO samples. My thanks also go to Jan Southard for her excellent work in reading and editing my thesis

Finally, I thank my wife, Gebi, for her love and support during these years. She has done her best to make our life smooth and joyful, while she works full time and goes to graduate school at the same time.

This thesis is dedicated to those who worked, who are working, and who will work in the field of SRF technology.

Contents

List of Figures

List of Tables

Chapter 1

RF Surface Resistance

1.1 Introduction

The Continuous Electron Beam Accelerator Facility (CEBAF) is now being built in Newport News, Virginia. Upon completion, it will accelerate a 200 μA electron beam to an energy of 4 GeV with a duty factor of 100%. The initial operation for nuclear physics research is scheduled in late 1994 [1].

The beam is accelerated by 338 superconducting niobium cavities which are operated at a field gradient of 5 MV/m and $Q_0 \geq 2.4 \cdot 10^9$ at 2 K. Under such conditions, a 0.5 m long, 5-cell cavity working at 1.5 GHz only consumes 5.43 W power on the surface of its wall. On the other hand, a copper counterpart consumes 0.56 MW power at room temperature, which explains why most normal cavity accelerators have to work in pulse mode. Taking the application at CEBAF as an example, given that the efficiency of a cryogenic refrigerator is 0.13% and the static heat dissipation in helium is 1.6 W per cavity, the power dissipation per cavity converted to room temperature is only 5.4 kW, which yields one hundred times net saving. The huge difference between the normal conducting cavity and the superconducting cavity comes from the difference in surface resistance. In the

superconducting state, BCS surface resistance decreases exponentially with the temperature decrease until residual losses (normally in the range of a few tens of nΩ) start to play a role. While in a normal conducting state, the anomalous effect prevents any further improvement of the surface resistance (several mΩ of R_s normally) when the mean free path is larger than its skin depth.

The discovery of high-T_c superconductors in 1986 [2] makes the application of superconducting materials even more attractive. The operating cost for any large scale application would be further reduced by a factor of 20 due to the possibly higher working temperature. Since their discovery, great progress has been made in the fabrication, characterization, and application of high-T_c superconducting oxides, although there is still no final answer about their superconducting mechanism.

Measuring surface resistance of superconductors not only gives material parameter information for device applications, but also provides information for understanding of superconducting mechanisms, such as energy gap and electromagnetic interaction with quasiparticles. In addition, surface resistance is directly related to material quality such as grain size, alignment, impurity phases, and surface morphology. Many groups around the world have developed different RF measurement methods to study microwave properties of high-T_c superconductors. However, due to the large surface area ratio of the cavity to the sample, all the cavity methods used to measure high T_c superconducting samples have a detection limit of at least tens of $\mu\Omega$ independent of their resonant frequency, while the surface resistance of the best epitaxial film has been reduced to the $\mu\Omega$ range. As the quality of high-T_c superconductors improves with improvements in fabrication methods, a reliable, accurate, and highly sensitive measurement method becomes a necessity.

We have designed and fabricated a new type of superconducting niobium triaxial cavity to meet the need of the rapid development in material properties and device applications. It employs two independent measurement methods to measure surface resistance, i.e., both the microwave method and the calorimetry method. Careful consideration has been taken

concerning the cavity structure, field distribution, and sample location, which guarantees the measured losses are only from the tested sample. Using the highly sensitive calorimetry method, the detection limit is pushed down by several orders of magnitude to as low as 0.02 nΩ at a surface magnetic field of 52 Oe. With such a device, measurements of residual resistance of high-T_c superconductors can be done accurately, and are expected to provide useful material information for device design and a quantitative understanding of the weak link effect on residual resistance of granular superconducting cuprates.

The unique features of the triaxial cavity are as follows:

(1) It has negligible edge effect and film-to-substrate interface losses;

(2) Its size is compact for a 1.5 GHz cavity, which concentrates a significant fraction of the stored energy near the test sample;

(3) Its sensitivity is high due to 2 μK resolution of the calorimetric measurement;

(4) Its measurement result is accurate and reliable because of the 16-sensor temperature mapping;

(5) The data aquisition and calibration process is computer-controlled;

(6) The cavity, plus the sample being tested, is cylindrically symmetric, which makes it straightforward to compare the experimental results with the theoretical calculations;

(7) The working temperature is at 2 K.

Due to the fact that the mechanism of high-T_c superconductors is still unknown, the concept of surface resistance will be briefly reviewed in Chapter 1. The high residual resistance of superconducting cuprates will be discussed in the last section. In Chapter 2, commonly used surface resistance measurement techniques will be reviewed from the design and measurement point of view, which is where the new triaxial cavity design begins. In chapter 3, the design, fabrication, and processing of the triaxial cavity will be described. RF test

be included in Chapter 4. Finally, the experimental results of high-T_c superconductors will be presented and the measurement method itself will be discussed as a whole in Chapter 5.

1.2 Surface Resistance of Normal Conductors

In the following two sections, the definition of surface resistance will be given. Fundamentals of loss mechanisms will be discussed. Standard International (SI) units are used.

1.2.1 Surface Resistance

From Maxwell's equations and Ohm's law [3], the magnetic and electric fields ($\mathbf{H}_c$ and $\mathbf{E}_c$) inside a semi-infinite conductor obey:

$$\mathbf{H}_c = \mathbf{H}_s e^{-(1+j)z/\delta} \tag{1.1}$$

$$\mathbf{E}_c \simeq \sqrt{\frac{\mu\omega}{2\sigma}}(1+j)(\mathbf{n}\times\mathbf{H}_c)\, e^{-(1+j)z/\delta} \tag{1.2}$$

where $\mathbf{H}_s$ is the tangential magnetic field on the surface, μ is the magnetic permeability and σ is the conductivity of the conductor, $\omega = 2\pi f$ is the angular frequency of the electromagnetic wave, z is the distance from the surface and its direction is towards the inside of the conductor, $\mathbf{n}$ is pointing to the outside from the inside (shown in Figure 1-1), and δ is the so called *skin depth*, given by:

$$\delta = \left(\frac{2}{\mu\sigma\omega}\right)^{1/2} \tag{1.3}$$

These formulas are correct for any good conductor ($\sigma/\varepsilon\omega \gg 1$), where the displacement current is neglected. δ is inversely proportional to $\omega^{1/2}$, which is 1.7 μm for copper at 1.5 GHz and at room temperature. As can be seen from (1.1), the skin depth defines the region into which electric and magnetic fields penetrate.

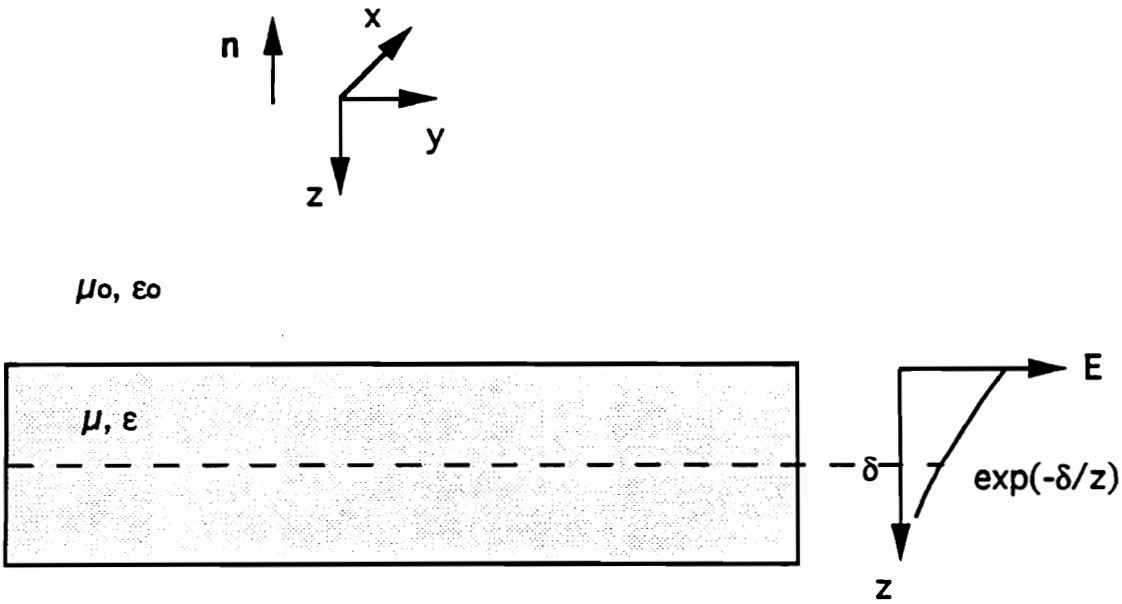

Figure 1-1: Field distribution inside a good conductor

The surface impedance of a conducting material, Z_s, is defined as:

$$Z_s \equiv \frac{E_x(z=0)}{H_y(z=0)} = R_s + j\,X_s \tag{1.4}$$

where R_s is the surface resistance and X_s is the surface reactance. The power dissipated per unit area inside the conductor can be calculated with the Poynting theorem, which is equal to the energy flux on the surface:

$$P_{loss} = \frac{1}{2} Re(E_{x0} H_{y0}) = \frac{1}{2} R_s H_s^2 \tag{1.5}$$

Note the fields here are their peak values. The RF loss is proportional to the surface resistance and the square of the surface magnetic field. For the application of cavities in high energy particle accelerators, the surface magnetic field H_s is proportional to the accelerating field gradient E_{acc}, which is usually larger than 5 MV/m in superconducting cavities. This would create prohibitive heat loss on the cavity wall if normal conducting cavities were used in CW mode. Therefore, reducing R_s is a direct solution for applications like those at CEBAF.

The surface impedance and the surface resistance of a good conductor can be obtained from (1.2):

$$Z_s = \sqrt{\frac{j\mu\omega}{\sigma}} \tag{1.6}$$

$$R_s = \sqrt{\frac{\mu\omega}{2\sigma}} = \frac{1}{\sigma\delta} \tag{1.7}$$

If an integration of $\mathbf{J} \cdot \mathbf{E}$ is done in the z direction inside the conductor, the per unit area Joule loss inside the conductor is given by:

$$P_{loss} = \frac{1}{2\sigma\delta} H_s^2 = \frac{1}{2} R_s H_s^2 \tag{1.8}$$

The agreement of (1.7) and (1.8) indicates that the energy flux getting into the conductor dissipates in the form of Joule heating. This is true only for the solutions (1.1) and (1.2), where conduction carriers are the sole source responsible for field decay inside the conductor.

For copper at 1.5 GHz, the surface resistance is 10.0 mΩ. At CEBAF's working conditions, this would produce an amount of useless power dissipation of 1.2 MW/m.

From the above discussions, the following points can be further said about the concept of *surface resistance*:

(1) It is defined as the real part of the coefficient of E_t (in the x direction) and H_t (in the y direction). Noticing $H_y(z=0) = K_{eff} = \int_0^\infty J_x(z)\,dz$ is the line current density, and their dimensions are [V/m] and [A/m], the definition can be viewed as an extension of $R = V/I$, or

$$R_s = Re\,(\frac{E_t}{H_t}) = \frac{V/l}{I/w} = \frac{1}{\sigma}\frac{l}{w\delta}\frac{w}{l} = \frac{1}{\sigma\delta} \tag{1.9}$$

For a given area of conductor, the total power loss is given by:

$$P_{loss} = \int \frac{1}{2} R_s H_s^2\, da \tag{1.10}$$

(2) For a good conductor, the surface resistance is the same as the dc resistance of a plane conductor of depth δ (eq. 1.9). It also seems as if all the RF losses come from the region of δ (eq. 1.8). This simplified picture is still valid in the anomalous skin effect and in the simplified picture of the two-fluid model.

(3) The loss mechanisms for a dc current and an RF wave are the same. They are both related to the conductivity σ, which comes from electron-lattice scattering, or electron - phonon scattering. Mathematically, the loss term simply can be treated as a phenomenological damping force for each individual electron [4]. The penetration depth specifies the region where these energy transferring scattering events happen.

(4) Equations (1.4) and (1.5) are universal, while equations (1.3) and (1.6) can be generalized if an effective conductivity σ' is used, or even an effective dielectric constant ε' is used to include both conductor losses and dielectric losses. Nevertheless, the loss mechanism from conducting electrons is a leading term in most cases.

(5) The energy loss mechanism from conducting electrons can be described simply as follows. An electron absorbs *photons* from the electromagnetic wave in the region of δ, then it interacts with the positive ions electrostatically and releases its absorbed photon energy to the lattice through *phonons*. The ion lattice then vibrates with larger amplitude, which corresponds to a higher temperature of the material. If any one of the steps disappears in the process, the losses will be zero. (There are no phonon - electron exchanges for $\sigma \to \infty$ and no free electrons for $\sigma = 0$.) As a whole, electromagnetic energy which flows into the conductor converts to Joule loss, using electrons as intermediate particles.

(6) Finally, for thin films whose thickness is smaller than a skin depth, solutions for semi-infinite conductors are no longer valid. Corrections need to be done in this case, depending on the film thickness [5].

1.2.2 Anomalous Skin Effect

One way to reduce the surface resistance of a conductor, according to equation (1.7), would be to increase its conductivity by lowering the temperature. However, experimental results have shown that when copper is cooled from 300 K to 4.2 K, its conductivity is improved by four orders of magnitude, but its surface resistance is only reduced by four times [6]. Further reduction of surface resistance is limited by the so called *anomalous skin effect.*

The anomalous skin effect happens in pure metals when cooled down to low temperatures. Electrons in such metals have a long mean free path due to less lattice scattering. When the mean free path is not small compared to the penetration depth, Ohm's law $\mathbf{J} = \sigma\mathbf{E}$ is no longer valid. A non-local relation between the current density and the electric field must be used as a substitution, which is given by Chamber's relation [7]:

$$\mathbf{J}(\mathbf{r}) = \frac{3\sigma}{4\pi\ell}\int \frac{\mathbf{R}\,[\mathbf{R}\cdot\mathbf{E}(\mathbf{r}')]\,e^{-R/\ell}}{R^4}\,d\mathbf{r}' \tag{1.11}$$

where $\mathbf{R} = \mathbf{r} - \mathbf{r}'$; the current density at point $\mathbf{r}$ is now related to field $\mathbf{E}(\mathbf{r}')$ throughout a volume of radius ℓ about $\mathbf{r}'$; ℓ is the mean free path and σ is the conductivity defined

when the field **E** is uniform in the range of ℓ. The expression of the surface resistance can be derived as [6]:

$$R_s = \frac{8}{9}\left(\frac{\sqrt{3}}{16\pi}\frac{\mu^2\omega^2\ell}{\sigma}\right)^{1/3} \tag{1.12}$$

As it can be seen, R_s no longer decreases with the decreasing temperature because σ/ℓ is constant. In addition, R_s is proportional to $\omega^{2/3}$ instead of $\omega^{1/2}$.

If an effective conductivity, $\sigma_{eff} = \beta(\delta/\ell)\sigma$, is defined, Ohm's law, equation (1.2), and (1.6) can still be used to get the same result as (1.12) except for the undetermined constant β. This gives a simple phenomenological description, since it is as if only those electrons which are in the region of δ_{eff} contributed to the RF loss [8].

It must be noted that the simplified picture does not mean that Ohm's law is universal and is thus extended. Ohm's law is used because it is more recognized and easily accepted. Moreover, an average value of σ can always be found to satisfy equation (1.11), which is why the "fudge factor" β exists. This effective conductivity should not be treated seriously at any rate because there is no such uniform field E to define conductivity. In the limit of $\ell \rightarrow 0$, equation (1.11) yields Ohm's law, indicating Ohm's law is a special case of Chamber's relation.

The physics origin of the anomalous skin effect comes from two compromising factors. One is the increasing mean free path which enhances the current flow for a given field and tends to reduce the skin depth. The other is the decreasing number of electrons existing in the decreasing skin depth layer which reduces the current and prevents further reduction of the skin depth. For situations where the field B(z) is not exponential, the skin depth is generally defined as [9]:

$$\delta = \frac{1}{B(0)}\int_0^\infty B(z)\,dz \tag{1.13}$$

1.3 Surface Resistance of Conventional Superconductors

1.3.1 Historical Background

In 1911, three years after the liquification of the last "permanent" gas of helium, H. Kamerlingh Onnes [10] first observed the disappearance of resistivity of mercury below 4.15 K, which he named *superconductivity* due to $\rho = 0$. In 1933, Meissner and Ochsenfeld [11] discovered the so-called *Meissner effect* when they observed that magnetic flux was expelled from a superconducting lead rod, i.e., the phenomenon of *perfect diamagnetism* ($\mu = 0$). As is known today, these two phenomena define any existing superconductor. In 1935, the brothers H. and F. London [12] proposed two equations, working in weak fields, to explain these two unique electrodynamic properties after the Gorter and Casimir's two-fluid model [13]. In 1950, Ginzburg and Landau [14] worked out a phenomenological theory, using an order parameter $n_s = |\psi|^2$ to deal with variation of superconducting electron density and strong field cases. In the same year, the isotopic effect was observed by Maxwell and Reynold [15], which confirmed that phonons were involved in the superconductivity mechanism. In 1957, Bardeen, Cooper, and Schrieffer (BCS) [16] finally worked out the problem, 46 years after its discovery. It was then understood that Cooper pairs, which are bound states of paired electrons formed at low temperature due to phonon mediation, are the superconducting charge carriers. Based on BCS theory, all aspects of superconducting properties have been explored. It was generally accepted that the phonon-mediation mechanism had a T_c upper limit of 40 K, until the breakthrough of high-T_c superconductors [17].

Although Onnes predicted large scale electrical applications in 1911, the applications had not been started until 1960, when Hulm, Kunzler, and Matthias [18] found out that a large critical field and a large critical current could coexist in type II superconductors, such as Nb_3Sn. This stable structure was understood three years before by Abrikosov [19] by using the Ginzburg-Landau theory. In 1962, Josephson effect was discovered [20], which started a new round of device revolution, such as the development of high precision devices like

SQUIDs (Superconducting Quantum Interference Device). Among the large scale and high field application studies, research of superconducting cavities in newly developed microwave accelerator technology was started at Stanford [21], which led to today's application at CEBAF [1].

The endeavor to implement large scale applications could be seen partially from the examples in superconducting radio-frequency technology [22]. The two challenging tasks have been: (1) lower the surface resistance in order to reduce the RF losses on the cavity wall, and (2) increase the accelerating field gradient. The first has been achieved quite satisfactorily by improving surface treatment methods to reduce residual resistance. A low number of 2 nΩ has been achieved at different frequencies in different laboratories. The other problem appeared to be more troublesome. Thermal magnetic breakdown, multipacting, field emission, etc., have slowed the pace to approach the 60 MV/m theoretical critical field barrier for niobium. New material fabrication methods, welding procedures, high temperature treatments, chemical processing, etc., were extensively studied before reaching today's application specifications.

1.3.2 BCS Surface Resistance

Within superconductors, there are two equations to describe their electromagnetic properties, known as London's equations [9]:

$$\mathbf{E} = \Lambda \frac{\partial \mathbf{J}}{\partial t} \tag{1.14}$$

$$\mathbf{B} = -\Lambda (\nabla \times \mathbf{J}) \tag{1.15}$$

where $\Lambda = m/ne^2$, e is the electron charge, n is density of the electrons, and m is the mass. Both equations represent the perfect conductivity and the perfect diamagnetism respectively.

From Maxwell's equations and London's equations, the solution of field distribution inside

a semi-infinite superconductor has a similar form as in (1.1):

$$\mathbf{H}_c = \mathbf{H}_s e^{-z/\lambda_L} \tag{1.16}$$

λ_L is called London penetration depth, which is expressed as:

$$\lambda_L = \left(\frac{m}{\mu_0 n_s e^2}\right)^{1/2} \tag{1.17}$$

where $n_s \simeq n$ is the density of the paired superconducting electrons.

The electric field and the current density satisfy the same exponential relation as the magnetic field does. To calculate the surface resistance when $T \neq 0$, a complex conductivity, derived from the simple two-fluid model [9],

$$\sigma = \sigma_1 - j\sigma_2 = \frac{n_n e^2 \tau}{m(1+\omega^2\tau^2)} - j\left(\frac{n_s e^2}{m\omega} + \frac{n_n e^2(\omega\tau)^2}{m\omega(1+\omega^2\tau^2)}\right) \tag{1.18}$$

can be used to calculate the surface impedance with (1.6), which gives:

$$Z_s = (j\omega\mu_0/\sigma)^{1/2} \simeq (\omega^2\mu_0^2\lambda_L^3 n_n\sigma_n/2n_s) + j\omega\mu_0\lambda_L = R_s + j\omega L_s \tag{1.19}$$

where τ in eq. (1.18) is the average time constant between two electron-phonon collisions, n_s and n_n are the densities of electron in the paired and unpaired states. When $T = 0$, the normal electron density $n_n = 0$, which results in $R_s = 0$. In a normal conducting state, R_s has the same magnitude as X_s (the reactance). In the superconducting state, R_s is much smaller than ωL_s when $T < T_c/2$. Notice that λ_L is the dc magnetic field penetration depth and is independent of frequency. When $n_n \ll n_s$, the microwave penetration depth is approximately the same as λ_L, because the supercurrent contributes to magnetic shielding.

Although there is a significant difference between conducting mechanisms in a normal conducting state and in a superconducting state, the loss mechanism is exactly the same. The loss is caused by normal electrons within the penetration depth layer. What happens is that the supercurrent shields the external field, yielding an exponentially decaying field inside the superconductor, and the normal current causes the loss due to interaction with the

penetrating field. Further knowledge from BCS theory gives $n_n/n = e^{-\Delta(T)/kT} = e^{-\alpha T_c/T}$ when $T < T_c/2$, which explains the dramatic decrease of R_s when lowering the temperature.

Again, London's equations are localized equations between **J** and **E**. General analysis has to take boundary conditions and more physical parameters into account to describe the transport behavior in a thin layer near the surface. This was done by Mattis and Bardeen in 1958 [23]. It included the size of the Cooper pairs (*coherence length*), the mean free path, the Fermi velocity $\mathbf{v}_f$ (related to the electronic structure of the material), in addition to the critical temperature T_c and the energy gap $\Delta(T)$. However, it is quite complicated, and a more commonly used expression of surface resistance is:

$$R_s \simeq A\left(\frac{\omega^\gamma}{T}\right)e^{-\alpha T_c/T} \tag{1.20}$$

for $T < T_c/2$ and $f < 10$ GHz; A is approximately unity in the formula and γ is between 1.7 - 2.2 (normally used as $\gamma = 2$). Precise calculation with the use of computer programs has been made possible separately by Halbritter and Turneaure [24], and results predicted with both programs agree well with experimental results [25].

If only the difference of the penetration depth and the density of electrons are taken into account, a rough estimation of surface resistance can be done easily. At 1.5 GHz, niobium at room temperature has a surface resistance of 27 mΩ and a skin depth of 4.7 μm. At 2 K, its penetration depth is 33 nm and $n_n/n = e^{(-1.86\times 9.2/2)} = 1.9 \times 10^{-4}$. These two factors result in a reduction of 1.33×10^{-6}, which can be extrapolated to an R_s of 3.6×10^{-8} Ω at 2 K. The result from Halbritter's program is 3.1×10^{-8} Ω.

The above discussion is limited to losses caused by normal conducting electrons, which is called BCS surface resistance. Because the surface resistance is lowered to the nano-ohm range at 1.5 GHz and below 2 K, other loss terms can no longer be ignored as was done in Section 1.2 for normal conductors. Residual resistance becomes an important term as will be discussed below.

1.3.3 Residual Surface Resistance

The experimental results of surface resistance of conventional superconductors can be expressed as:

$$R_s = R_{BCS} + R_{res} \simeq A\left(\frac{\omega^2}{T}\right) e^{-\alpha T_c/T} + R_{res} \tag{1.21}$$

where R_{BCS} reduces dramatically with temperature decrease and is proportional to the square of the frequency, while R_{res}, the residual resistance, is independent of temperature and frequency. Loss mechanisms of R_{res} are quite complicated to identify [26]. Several commonly observed loss mechanisms are summarized as the following:

(1) Normal inclusions: These defects are normally included in the bulk superconductor or formed during the preparation process. Achieved residual resistances of 10 nΩ correspond to only about 1 ppm normal conducting area. As discussed before, surface resistance due to normal inclusions is proportional to $\omega^{1/2}$.

(2) Magnetically trapped flux: Due to the large demagnetizing factor of cavity walls, the superconducting walls are actually in a vortex state when placed in a residual magnetic field [27], which contains normal regions of fluxoids. These normal regions contribute to RF losses, which are about 5 nΩ/mGauss for niobium. Among all the mechanisms which are responsible for residual resistance, this is the only one which has been studied with systematic experiments [28].

(3) Dielectric layer under electric fields: The normal electric field is supposed to be terminated by the surface charge of the metal. During the exposure to air, niobium is easily oxidized to form a Nb_2O_5 and/or NbO layer. The field penetrates into this layer and causes dielectric losses.

1.4 Surface Resistance of High-T_c Superconductors

Although there is still no final answer about the pairing mechanism of high-T_c superconductors, a great amount of work has been done in developing different microwave characterization methods and measuring the surface resistance of high-T_c superconductors at different temperatures, frequencies, and field levels. In this section, we will simply present some well accepted concepts and results concerning high-T_c superconductors.

1.4.1 Occurrences

Since the discovery of the 40 K La-Sr-Cu-O system [2], superconducting cuprates working at liquid nitrogen temperature region have come into being. Typical examples are $Y_1Ba_2Cu_3O_7$ (93 K), $Bi_2Sr_2Ca_1Cu_2O_8$ (80 K), $Bi_2Sr_2Ca_2Cu_3O_{10}$ (110 K), $Tl_2Ba_2Ca_1Cu_2O_8$ (110 K), $Tl_2Ba_2Ca_2Cu_3O_{10}$ (T_c of 125 K). It is well known that the conducting carriers in these superconducting cuprates are holes from 2-d CuO_2 planes, and the number of CuO_2 planes in each unit cell is correlated with the transition temperature T_c. For example, $Bi_2Sr_2Ca_2Cu_3O_{10}$ and $Tl_2Ba_2Ca_2Cu_3O_{10}$(2223 structure) have three Cu-O layers. They have the highest T_c in their corresponding Bi-based and Tl-based families.

Other newly discovered materials include alkali-metal-doped fullerenes like K_3C_{60} and electron doped superconductors such as $Nd_{1.85}Ce_{0.15}CuO_4$, etc. As for the search for new materials, there is no reason why superconductors with higher T_c cannot be found.

1.4.2 Physical Parameters

Remarkable progress has been made in material preparation, characterization, and application of high-T_c superconductors. Table 1-1 provides some important material parameters which are related to microwave properties.

The major differences between the high-T_c superconductors and the conventional superconductors are the highly anisotropic nature and very short coherence length in these superconducting cuprates. The structural anisotropy results in a large anisotropy of conductivity, penetration depth, coherence length, critical magnetic field, etc. It is believed that the coherence length is even shorter for the more anisotropic BiSrCaCuO and TlBaCaCuO materials [29]. In addition, granularity of the oxides presents weak links to superconducting current, which causes extra losses when an external magnetic field is applied. This is why epitaxially grown thin film samples and bulk single crystal samples have far superior superconducting properties than their polycrystalline counterparts.

1.4.3 Thin Film Preparation

Table 1-2 presents some best RF measurement results for thin films prepared with different methods. The following is a brief description of each method:

(1) Laser ablation has been an effective method to make stoichiometric thin films of high-T_c superconductors. It does not involve a high electric field and therefore does not have the resputtering problem that the sputtering method does.

(2) The sputtering method is a commonly used thin film deposition technique. Initially, however, it was difficult to get stoichiometric films due to negative ion bombardment. This has been overcome by the off axis sputtering method and the high pressure sputtering method. One tradeoff for the solution is the lower deposition rate.

(3) MOCVD (Metalorganic chemical vapor deposition) is a widely used method in semiconductor technology. It has the advantage of growing uniform and large area films. In addition, thin films can be deposited on both sides for some applications without using a thermal adhesive.

(4) Electron beam evaporation is a common deposition method, but not as well developed as the sputtering method of preparing high-T_c superconductors. This is because the oxidation

Table 1-1: Important material parameters to microwave properties [30]

Material	T_c (K)	Δ_0/kT_c	ℓ (nm)	ξ_0 (nm)	$\lambda(0)$ (nm)	$\mu_0 H_c(0)$ (T)
Nb	9.2	1.97	> 100	39	40	0.20
Nb_3Sn	18	2.20	> 1	5.7	110	0.535
$Y_1Ba_2Cu_3O_7$ (preliminary)	93	1.5-4 (anisotr?)	> 1	ab: <2 c: <0.4	140 (ab) 770 (c)	1.0 - 1.4

Table 1-2: Best R_s achieved with different deposition methods (77 K) [31]

Material Preparation	T_c (K)	J_c (A/cm^2)	f (GHz)	R_s ($\mu\Omega$)
$Y_1Ba_2Cu_3O_7$ laser ablation (*in situ*)	93	5×10^6	2	< 40
$Y_1Ba_2Cu_3O_7$ sputtering (*in situ*)	84	$> 10^7$ at 4 K	10	450
$Y_1Ba_2Cu_3O_7$ MOCVD (*in situ*)	87	$> 10^6$	36	9500
$Y_1Ba_2Cu_3O_7$ evaporation (annealing)			12.5	375
$Tl_2Ba_2Ca_1Cu_2O_8$ sputtering (annealing)	107.6		10	130

of metallic components cannot be completed during the deposition and it must be done with a post annealing process.

There are two approaches to growing an epitaxial thin film on a single crystal substrate. One is *in situ* deposition, in which a film is deposited epitaxially on a hot substrate (normally higher than 700 ^0C). The other is the post annealing technique, in which a film is deposited at room temperature and then thermally treated afterwards. From table 1-2, it can be seen that there is virtually no difference in superconducting properties between these two approaches.

It has to be noted that the R_s value is strongly dependent on the thin film thickness, substrate, measurement frequency, and the measurement technique, in addition to the sample quality which is investigated. Simply comparing the values without knowing the measurement techniques and conditions may not lead to correct conclusions. This will be illustrated in detail in Section 2.5.

1.4.4 Results of Surface Resistance Measurement

As mentioned earlier, epitaxially grown high-T_c superconducting thin films have higher phase purity, a higher degree of alignment, cleaner grain boundaries, and better surface morphology than others. As a result, the surface resistance of epitaxial thin films has been improved about two or three orders of magnitude [30]. From the microwave characterization point of view, surface resistance measurements fall into the following three areas:

(1) Temperature dependance of R_s: It reflects the number of thermally excited quasi-particles, or normal electrons/holes which are related to the energy gap (eq. 1.19). In addition to the first gap of $2\Delta/kT_c = 2.4$ [32], a second gap $2\Delta/kT_c = 0.8$ has been reported [33].

(2) Frequency dependence of R_s: For conventional superconductors, R_{BCS} is proportional to $\omega^{1.7-2.2}$, while R_{res} is independent of frequency [34]. For high-T_c superconductors, an f^2 –

law is widely perceived and accepted for residual resistance [31]. Nevertheless, complicated mechanisms of residual resistance at high frequencies and lack of convincing results at low frequencies make it an open question (see Section 2.5).

(3) Surface magnetic field effect on R_s: For conventional superconductors, the losses are usually not enhanced by the surface magnetic field. For high-T_c superconductors, the response to the field depends strongly on sample qualities [35]. It has been known that epitaxial thin films and single crystals have the lowest surface resistance values, and the polycrystalline samples have the highest residual resistance, with the aligned and electroplated samples in the middle [36]. The results clearly indicate that broken weak links between grains play a role in RF loss mechanisms.

1.4.5 Some Points about Applications

At present, $Y_1Ba_2Cu_3O_7$ is the most widely studied among all the high-T_c superconducting oxides. High quality epitaxial thin films have been prepared and used for the study of superconducting properties as well as the fabrication of microwave components and other electronic applications. Good thin film samples up to 2″diameter have been grown on different substrates. Growth on silicon or sapphire with a buffer layer is also being pursued.

The Bi-system has better stability to the environment than $Y_1Ba_2Cu_3O_7$. It has been studied for potential large scale electric application. Wires and tapes which have a J_c of several times 10^4 A/cm^2 have been made. Further work will be undertaken on making long wires and achieving satisfactory current carrying ability.

The Tl-system has the highest transition temperature of 125 K. It has also been studied for applications in microwave devices. According to [31], it has lower surface resistance than $Y_1Ba_2Cu_3O_7$ at 77 K.

For microwave applications, the following results are encouraging: (1) The surface resistance of $Y_1Ba_2Cu_3O_7$ is lower than that of Cu at 77 K, (2) Large area, high quality thin films have

been epitaxially grown on crystal substrates, and (3) Some components have been fabricated from those large area thin films [37]. It is believed that the first practical applications of high-T_c superconductors will be some kind of microwave component.

Chapter 2

Surface Resistance Measurement

2.1 Introduction

As mentioned in Chapter 1, electromagnetic waves penetrate into good conductors within a thin layer δ (eq. 1.3) and cause small RF losses characterized by surface resistance (eq. 1.5). Most of the incident energy is reflected, and good conductors have a *reflection coefficient* of nearly unity [3]. To first order, the reflection coefficient $|\rho|^2$ is given by:

$$|\rho|^2 \simeq 1 - \frac{4R_s}{\eta_0} \tag{2.1}$$

where R_s is the surface resistance and $\eta_0 = \sqrt{\mu_0/\varepsilon_0} = 377\,\Omega$ is the characteristic wave impedance of vacuum. For copper at room temperature and at 1.5 GHz, R_s is 10.04 mΩ. Only a fraction of 1.1×10^{-4}, or 0.011%, of incident power penetrates into the copper from air. Therefore, good conductors form ideal boundaries for electromagnetic waves in the radio-frequency range. In addition, equation (2.1) also provides a method to measure surface resistance in the infrared range.

When several conducting walls enclose a space or a dielectric region, they form a cavity or resonator. With effective coupling from the outside world, electric and magnetic fields will

be built up at certain frequencies. When the power coupled into the cavity equals the power loss P_{loss} on the walls, the stored energy U inside the cavity will no longer increase. Then the stored energy resonates back and forth between electric energy and magnetic energy at a certain resonant frequency. The figure of merit of any resonator, Q, is defined as 2π times the ratio of the stored energy to the energy loss per cycle, that is:

$$Q \equiv 2\pi \frac{U}{P_{loss}/f} = \frac{\omega U}{P_{loss}} \tag{2.2}$$

where f is the resonant frequency, and $\omega = 2\pi f$ is the angular frequency. With $P_{loss} = -dU/dt$ when the coupled power is zero, the stored energy decays exponentially with time:

$$U(t) = U_0\, exp(-\omega t/Q_0) = U_0\, exp(-t/\tau) \tag{2.3}$$

where $\tau = Q_0/\omega$ is the time constant of the decaying process, and Q_0 is the Q when the coupled power is zero. As mentioned earlier, the power loss on the walls is characterized by surface resistance R_s. Therefore, provided that R_s is a constant on all parts of the cavity surface, the problem of measuring R_s is converted to a problem of Q measurement, which will be described in detail in the next two sections.

In this chapter, we will take a cylindrical cavity in the TE_{011} mode as an example, showing how to calculate Q and other parameters which are essential for cavity design. This will serve three purposes: (1) It shows the cavity design fundamentals, so that one can understand the output of the URMEL program (see Section 3.2) and effectively use the output parameters to design a cavity; (2) The URMEL program does not calculate TE_{0mn} modes; (3) Cavities working at the TE_{011} mode are widely used by many groups around the world to measure R_s of high-T_c superconductors, due to the fact that the change of samples requires a demountable cavity, and there is no current flowing through the joints at the end plates of a TE_{011} cavity. Based on the TE_{011} solution, the end plate replacement method and the Q-perturbation method will be analyzed in Section 2.3. In Section 2.4, cavities used for R_s measurements of high-T_c superconductors will be examined and their results will be given. Because the frequencies of planar resonators are in about the same

range as that of our triaxial cavity, their results will also be briefly summarized. In the last section, we will conclude this chapter by asking some fundamental questions concerning the surface resistance measurement of planar samples. Then we will try to answer and solve these problems with a new and unique cavity design in Chapter 3.

2.2 Cylindrical Cavities in the TE_{011} Mode

The resonant frequencies and the field distributions in a cylindrical cavity can be obtained by solving the Helmholtz equation:

$$\nabla^2 \mathbf{E}(r,\varphi,z) + k^2 \mathbf{E}(r,\varphi,z) = 0 \tag{2.4}$$

$$\mathbf{H} = -\frac{i}{\mu\omega}\nabla \times \mathbf{E} \tag{2.5}$$

with certain boundary conditions (for TE_{0mn} modes only):

$$\begin{aligned} E_z &= 0 \\ E_r\,|_{z=0} &= E_r\,|_{z=d} = 0 \\ \frac{\partial E_r}{\partial r}\,|_{r=R} &= 0 \\ E_\varphi\,|_{r=R} &= 0 \\ E_\varphi\,|_{z=0} &= E_\varphi\,|_{z=d} = 0 \end{aligned} \tag{2.6}$$

where R is the radius and d is the length of the cavity. The TE_{011} resonant frequency f is given by [38]:

$$f_{011} = \frac{c\,k_{011}}{2\pi} = \frac{c}{2\pi}\sqrt{\left(\frac{x_{01}}{R}\right)^2 + \left(\frac{\pi}{d}\right)^2} \tag{2.7}$$

where c is the speed of light in vacuum, and $x_{01} = k_r R = 3.832$ is the first root of $J_0'(k_r r)$. The solutions for the TE_{011} mode are:

$$\begin{aligned} H_r(r,z) &= -\frac{\pi}{d\,k_r} H_0\, J_1(k_r r)\, cos\,\frac{\pi z}{d} \\ H_z(r,z) &= H_0\, J_0(k_r r)\, sin\,\frac{\pi z}{d} \\ E_\varphi(r,z) &= \frac{\mu\omega}{k_r} H_0\, J_1(k_r r)\, sin\,\frac{\pi z}{d} \end{aligned} \tag{2.8}$$

There is only an azimuthal electric field component in the cavity, and the magnetic field has only a radial component on both the end plates and only a z-component at $r = 0$ and $r = R$. At the end plate ($z = 0$ or d), the maximum magnetic field is at $x_m = k_r r_m = 1.841$, which gives $r_m \simeq 0.48R$,

$$H_{max} = H_r(z = 0, r_m) = H_0 \frac{\pi R}{3.832\, d} J_1(3.832 \frac{r_m}{R}) = 0.477 \frac{R}{d} H_0 \tag{2.9}$$

at the side wall ($r = R$), the maximum magnetic field is at $z = d/2$, which is:

$$H_{max} = H_z(z = d/2, 0) = H_0 \tag{2.10}$$

These two maximum field locations are where thin film samples are usually located. In addition, the magnetic field is zero at $z = 0$ (and d) and $r = R$, which results in a zero current at the joints ($\mathbf{J} = \mathbf{n} \times \mathbf{H}$). This is the reason why the TE_{011} cavity is so popularly used for RF characterization.

The stored energy is:

$$U = \int_{cavity} \frac{1}{2} \varepsilon E_\varphi^2 \, dV = 4.74 \times 10^{-24} f^2 R^4 d H_0^2 \text{ Joules} \tag{2.11}$$

while the end plate loss P_1 and the side wall loss P_3 are:

$$P_1 = \int_{Z=0} \frac{1}{2} R_s H_r^2 \, da = 0.17 \frac{R^4}{d^2} R_s H_0^2 \tag{2.12}$$

$$P_3 = \int_{r=R} \frac{1}{2} R_s H_z^2 \, da = 0.251 R d R_s H_0^2 \tag{2.13}$$

With the total loss:

$$P_{loss} = P_1 + P_2 + P_3 = 2P_1 + P_3 \tag{2.14}$$

the Q of the cavity at the TE_{011} mode can be derived from eq. (2.2) and (2.6):

$$Q = c\pi\mu \frac{[3.832^2 + (\frac{\pi R}{d})^2]^{3/2}}{2\pi\,[3.832^2 + \frac{2R}{d}(\frac{\pi R}{d})^2]} \frac{1}{R_s} \tag{2.15}$$

The geometry factor of a certain mode is defined as:

$$G \equiv Q R_s = c\pi\mu \frac{[3.832^2 + (\frac{\pi R}{d})^2]^{3/2}}{2\pi\,[3.832^2 + \frac{2R}{d}(\frac{\pi R}{d})^2]} \tag{2.16}$$

which is related to the cavity shape and is independent of the cavity material and the resonant frequency. G is determined by the cavity dimensions and the resonant mode. For a given cavity with known dimensions, the geometry factor of the TE_{011} mode can be easily calculated from (2.16), and R_s can be obtained from

$$R_s = \frac{G}{Q} \tag{2.17}$$

with a measured Q.

At room temperature, Q can be determined with a network analyzer, which is given by

$$Q_L = \frac{f}{\Delta f} \tag{2.18}$$

where Δf is referred to as the half-power bandwidth (bandwidth of a 3 dB power loss), and Q_L is the loaded Q of the cavity. The cavity Q is given by

$$Q_c = Q_L(1+\beta_1) \tag{2.19}$$

when the pickup coupling $\beta_2 \ll 1$, and β_1 is the coupling factor of the input coupling probe [39]; Q_c is the Q_0 of the cavity.

When the cavity is in superconducting state, Q is usually measured by the decay method due to its high Q

$$Q_c = Q_L(1+\beta_1) = \omega\tau(1+\beta_1) \tag{2.20}$$

where τ is the time constant of the decay for the loaded cavity (eq. 2.3).

The coupling factor β_1 and the power loss P_{loss} inside the cavity can be determined from the incident power P_I, the reflected power P_R, and the transmitted power P_T [39]:

$$\begin{aligned} \beta_1 &= \frac{1-\sqrt{P_R/P_I}}{1+\sqrt{P_R/P_I}} \quad \text{when} \quad \beta_1 < 1 \\ \beta_1 &= \frac{1+\sqrt{P_R/P_I}}{1-\sqrt{P_R/P_I}} \quad \text{when} \quad \beta_1 > 1 \end{aligned} \tag{2.21}$$

and

$$P_{loss} = P_I - P_R - P_T \tag{2.22}$$

From the above formulas, R_s can be obtained from G (known from calculation) and Q, and the field H_0 can also be determined from (2.11) and (2.2). Then E_{max} and H_{max} can be calculated from H_0. As will be seen in Section 3.2, these quantities can be calculated by the URMEL program when the cavity dimensions and the resonant mode are given.

2.3 Measurement Techniques for Planar Samples

2.3.1 End Plate Replacement Method

When the bottom plate of the TE_{011} cavity is replaced with a plate of a different material, the cavity Q will be changed. By measuring the change of the cavity Q, the surface resistance of the substituted material can be calculated from the known quantities, as will be shown below.

Dividing eq. (2.14) by ωU, Q_i of different parts can be defined as:

$$\frac{1}{Q_c} = \frac{1}{Q_1} + \frac{1}{Q_2} + \frac{1}{Q_3} = \sum_i \frac{1}{Q_i} \tag{2.23}$$

$$Q_i \equiv \frac{\omega U}{P_i} \tag{2.24}$$

If part i has a different surface resistance R_s' (from now on, "$'$" designates the substituted material), then:

$$\frac{1}{Q_i'} = (\frac{1}{Q_c'} - \frac{1}{Q_c}) + \frac{1}{Q_i} = (\frac{1}{Q_c'} - \frac{1}{Q_c}) + \eta_i \frac{1}{Q_c} \tag{2.25}$$

where Q_c and Q_c' are cavity Q's before and after the replacement, and

$$\eta_i \equiv \frac{1/Q_i}{1/Q_c} \tag{2.26}$$

is defined as the filling factor of the changed part, which is decided by the geometric size, the field distribution inside the cavity, and the location of the part. The filling factor can be

obtained by calculation or calibration for any given structure. For an end plate of a TE_{011} cavity, η_i is given by:

$$\eta_i = \frac{Q_c}{Q_i} = \frac{P_i}{P_{loss}} = \frac{0.17(R/d)}{0.34(R/d)^2 + \frac{0.251}{R/d}} \tag{2.27}$$

Notice that Q_c or Q_i is independent of the field, but dependent on the surface resistance, while η_i is not dependent on either. The geometry factor G_i can also be defined for each part

$$G_i \equiv Q_i R_{s_i} = \frac{\omega U}{P_i} R_{s_i} \tag{2.28}$$

and

$$\eta_i = \frac{G}{G_i} \tag{2.29}$$

Therefore, the surface resistance of a substituted material can be derived:

$$R'_{s_i} = \frac{G_i}{Q'_i} = \frac{G}{\eta_i Q'_i} = \frac{G}{Q_c}[\frac{1}{\eta_i}(\frac{Q_c}{Q'_c} - 1) + 1] \tag{2.30}$$

where $R_{s_i} = R_s = G/Q_c$ is the surface resistance of the cavity material, and $R'_{s_i} = R'_s$ is the surface resistance of the tested sample. With the known η_i, G, the measured Q_c and Q'_c, R'_s can be simply calculated from eq. (2.30).

From eq. (2.30), it can be easily seen that the measurement accuracy of R_s is dependent on the Q measurement accuracy, i.e.

$$\Delta R_s = \frac{G}{Q_c}\frac{1}{\eta_i}\frac{\Delta Q}{Q'_c} = \frac{R_s}{\eta_i}\frac{\Delta Q}{Q'_c} \tag{2.31}$$

where $\Delta R_s = R'_s - R_s$ and $\Delta Q = Q'_c - Q_c$.

2.3.2 Q Perturbation Method

When the sample size is not as large as the end plate, the Q-perturbation method is usually used to measure R'_s. One basic assumption or requirement of this method (unless appropriate corrections are made) is that the existence of the sample does not change the field

distribution inside the cavity due to its small size. It is also assumed or required that the sample is in its proper location and orientation. For high-T_c superconductors, this method has been widely used because high quality superconducting crystals and thin films have limited sizes.

The formulas derived in 2.3.1 are still valid for the Q-perturbation method. The difference is the smaller filling factor η_i due to the smaller geometric area ratio. Rewriting equation (2.29) gives:

$$\frac{\Delta Q}{Q'_c} = \eta_i \frac{\Delta R_s}{R_s} \tag{2.32}$$

which indicates that for any given $\Delta Q/Q'_c$, the filling factor η_i needs to be maximized for detection of a small enough ΔR_s. To increase η_i, or P_i (eq. 2.24), samples are always placed in a strong field region. Moreover, a superconducting parent cavity is usually used, so that the resolution $\Delta R_s/R_s$ is improved. This explains why niobium cavities are usually used and samples are usually placed at $(r = 0.48R, z = 0)$ or $(R = 0, z = d/2)$ [41].

One major disadvantage of the Q-perturbation method is that by placing the entire sample at the maximum magnetic field location, some extra unwanted losses may be created on the sample edge and between the interface of the thin film and the substrate, or even in the substrate itself. This is because the current flowing on the sample surface has to flow over the edge, and the sample quality at the edge is usually poor. In addition, any component of the current flowing parallel to the edge will cause a very large magnetic enhancement. The losses from the edge effect have not been well stressed in the past, which might be responsible for the systematic higher R_s's when compared to those measured by planar resonators.

Although efforts are made to maintain the disturbance of the sample to the field at a minimal level, the location of the sample is normally not in a symmetric position within the field distribution. This will make it impossible to calculate G_i (geometry factor of the tested sample) with two dimensional computer codes such as URMEL [40], because the program requires cylindrical symmetry. Three dimensional codes such as MAFIA [40] do

not have sufficient resolution to deal with small samples. Therefore, a calibration run, using a sample which has a known R_s and is the same size as the tested one, is always needed. This is not an easy task for an accurate measurement and will introduce some error in the result.

As will be described in Chapter 3, these disadvantages have been successfully eliminated in our triaxial cavity.

2.4 Measurement Techniques for High-T_c Superconductors

In this section, we will describe several types of cavities, their field distributions and sensitivities. Results measured from planar resonators are also collected here for future comparisons. All the data used here, unless specified, are reported measurement results (no f^2 scaling).

2.4.1 TE_{011} Cavity

Q-perturbation Method

Figure 2-1 shows a cavity developed by the Cornell group [41]. It is a high-Q superconducting niobium cavity working at 4.2 K. The sample is mounted on a thermally insulated sapphire rod which is inserted into the cavity through a cutoff tube along the cavity axis. The sapphire rod is thermally coupled to the helium bath through a thermal resistor. A heater and a thermometer are attached to the rod, so that the temperature of the sample can be controlled for measurement and the RF losses on the sample can be measured calorimetrically, which yields higher sensitivity than the RF method.

Temperature dependence and field strength dependence of surface resistance can be measured with this type of cavity. An energy gap of $2\Delta/kT_c = 2.4 \pm 1.0$ was determined from

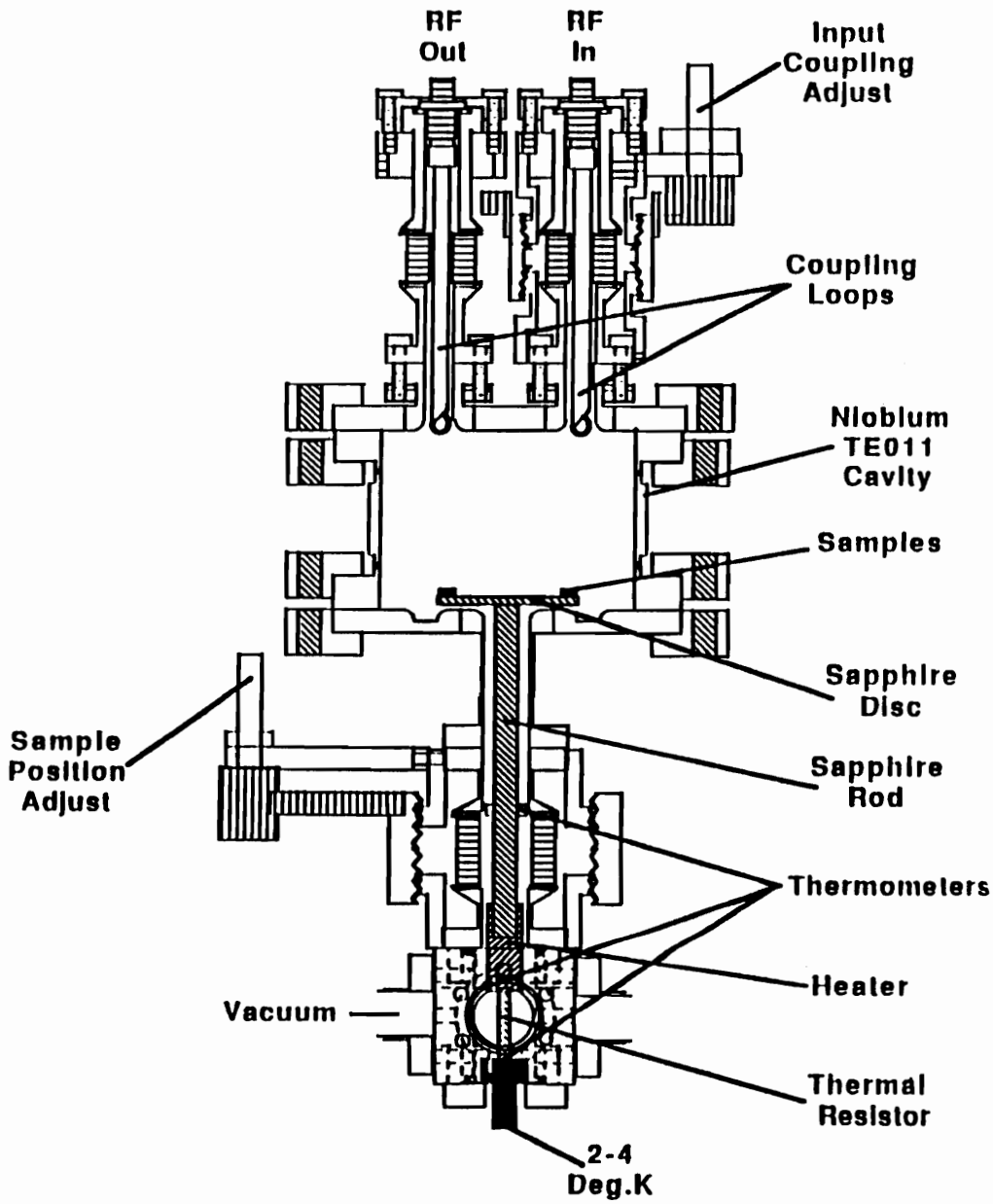

Figure 2-1: The cylindrical niobium cavity resonates at 5.95 GHz in the TE_{011} mode

the R_s – T curve [32], and the field response up to 100 G was measured for different samples. The detection limit of the RF method is 1 mΩ, and the detection limit of the calorimetric measurement is 15 $\mu\Omega$ at 2 K.

Other laboratories, such as groups at Northeastern University [36] and Superconductor Technology Inc. [42], have also employed the Q-perturbation method in a TE_{011} cavity. The frequency range covers 6 – 20 GHz, while the sensitivity is normally above 1 mΩ, depending on the sample size.

Although the calorimetric measurement can greatly improve the sensitivity, the sensitivity is ultimately limited by the background losses from the sapphire rod and the grease. The edge effect, substrate, and interface between the thin film and the substrate will also result in some extra losses, which should be excluded in a well defined measurement.

End Plate Replacement Method

Figure 2-2 shows a copper TE_{011} cavity used by the Wuppertal group [43]. As shown in 2.3.1, it has a better defined test geometry and its geometry factor is calculable. Because the cavity was designed for a 2.54 cm diameter sample, the resonant frequency is above 20 GHz. For the coupling system, waveguides are used because of the high frequency. In the transition temperature region of the sample, copper cavities are preferred because it is convenient to perform experiments in external magnetic fields and at different temperatures. In addition, RF losses in normal conductors are less sensitive to high frequencies than RF losses in superconductors ($f^{1/2}$ *vs.* f^2).

The frequency range of this method covers 18.7 GHz – 148 GHz [44]. The sensitivity is normally a few mΩ, which is limited by the background loss of the copper cavity. To improve sensitivity, cavities made of superconducting materials can be used to reduce the background loss. However, there will normally be poor contact between the superconductor and the cavity, and any asymmetries will cause currents to cross this joint.

Higher order TE_{0mn} modes are also used to increase the sensitivity. In addition, several modes can be used to study the $R_s - f$ relation in the same cavity.

Compared to the frequency for most accelerator applications, the frequency range of this type of cavity is somewhat too high. Moreover, the loss mechanisms at high frequencies may be different from those at low frequencies, so that frequency extrapolation may not be valid.

Cavities Made from High-T_c Superconductors

Cavities made of bulk $Y_1Ba_2Cu_3O_7$ and thick films have been studied by researchers at Northeastern University and ICI [45]. The thick film result of ICI is very promising. Thick films are coated on polycrystalline yttria stabilized zirconia (YSZ) substrates, which are in the form of discs (up to 100 mm in diameter) and tubes (70 mm i.d., 2 mm wall thickness, and 75 mm long). At 77 K, the high-T_c superconducting cavity has a Q of 7.16×10^5 at a resonant frequency of 5.66 GHz, yielding a surface resistance of 1.09 mΩ on an area of 230 cm^2. The R_s is one order of magnitude lower than that of copper and is one of the best results for large area samples.

As for this type of cavity, there is no concern about the measurement sensitivity. The overall performance, which includes the material quality, the machining capability, etc., is the focus of the study. Therefore, this type of cavity is not a good candidate of RF characterization methods used for the study of intrinsic material properties.

2.4.2 $\lambda/4$ TEM Cavity

A $\lambda/4$ TEM niobium cavity (Figure 2-3) with a relatively large filling factor was developed by the Argonne group [46]. It has a resonant frequency of 820 MHz (table 2-1), which is within the most common range of accelerator frequencies of 0.3 GHz to 3 GHz. The

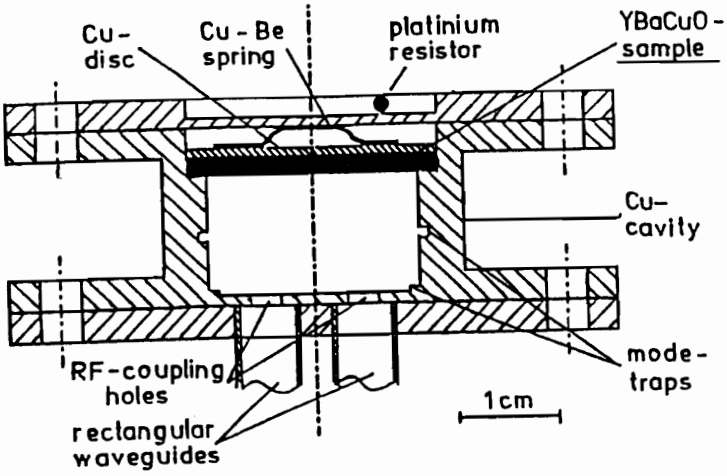

Figure 2-2: End plate replacement TE_{011} cavity

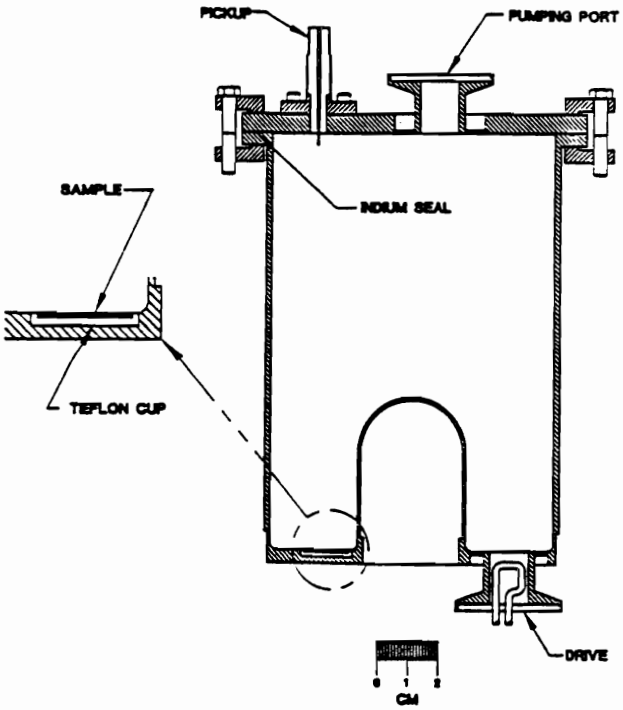

Figure 2-3: Coaxial quarter-wave ($\lambda/4$ TEM) niobium cavity

resonant frequency is lowered by its coaxial line structure and it has a larger filling factor than a TE_{011} cavity. Compared to the commonly used TE_{011} cavity, its sensitivity has been improved 15 times for a 24 mm diameter sample because of its compact size for a low frequency. The magnetic field is circumferential on the bottom plate, gradually decaying along the radial direction. Along the z direction, the field decreases more rapidly. Therefore, significant RF losses will not be caused by the indium vacuum seal placed at the top end of the cavity. The bottom plate is welded to the side wall, minimizing the possible joint losses due to the symmetry breaking effect from the drive coupling hole. Its strongest magnetic field location is at the juncture of the center conductor and the bottom plate. A 24 mm diameter sample is placed at the strongest magnetic field region to measure its surface resistance at 4.2 K. The relationship between the surface resistance and the surface magnetic field has been measured up to 300 Gauss when the cavity was filled with liquid helium.

At 4.2 K, a Q of 8×10^7 was measured when the cavity was filled with liquid helium but with no sample. It yields a surface resistance of 1.16 $\mu\Omega$, which is 5 times higher than the theoretically calculated value for niobium. At a peak field of 0.5 Gauss, the lowest R_s measured is 20 $\mu\Omega$ which was measured in a TBCCO thick film coated on a silver substrate. When a stainless steel disc was used for calibration in the experiment, about 50% more losses were observed if the losses were only from the upper surface of the disc, indicating that about 2/3 of the losses came from the top and 1/3 from the bottom surface.

Although the existence of the liquid helium improves the field level from 150 Gauss to 300 Gauss by suppressing the multipacting, it may also degrade the Q value and be responsible for the result being 5 times lower than the expected value.

2.4.3 R_s Measurement with Planar Resonator

Planar resonator methods represent a different approach to characterizing microwave properties of high-T_c superconductors, and will be examined in limited detail. One exception is

Table 2-1: Different cavity techniques and their sensitivities (N.A.: not applicable)

Cavity type	f (GHz)	Result (mΩ)	Size (cm^2)	Sensitivity (mΩ)
$\lambda/4$ TEM [46]	0.82	0.02	0.74	0.02
TE_{011} (HTSC)[45]	5.66	5.6	230	N.A.
TE_{011}[41]	5.95	1.0	0.073	1.0
TE_{011}[42]	9.5	< 0.3	0.5	0.3

Table 2-2: Different planar resonators and their measurement sensitivities

* Results at 77 K, scaled back to measurement frequency;

** Results measured below T_c, BiSrCaCuO.

Resonator type	f (GHz)	Result (μΩ)	Size (cm^2)	Sensitivity (μΩ)
Stripline[48]	1.56	17*	patterned	
Split Ring[49]	1.78	25**	0.01	
Ring Resonator[50]	10.14	> 1500	patterned	N.A.
Parallel Plate[51]	12	56	1.0	5

the parallel plate resonator, which has a simple field distribution, minimal sample preparation (i.e. no patterning), and no superconducting or conducting materials involved other than the samples. In addition, most of the best reported data (Table 1-2) were measured by this method.

The experimental setup [51] consists of two 1 cm $\times$ 1 cm samples, with a thin dielectric spacer (12.5 μm Teflon FEP) between them. The samples are pressed with two dielectric posts and are put inside a gold-plated brass test chamber to improve the boundary condition of the resonator. The coupling probe is a few tenths of a millimeter away from the edge, which contributes greatly to the success of the method. The coupling is chosen to be so weak that the loaded Q_L is about the same as unloaded Q_0 ($\beta_1 \ll 1$ in eq. 2.17). Because of this, Q is too small to have the signal measured when the sample has a surface resistance of above 1 mΩ. The losses in the measurement come from: (1) surface resistance of the tested samples, (2) dielectric layer, and (3) radiation loss at the edges. Normally, the spacing is chosen to be small enough to have the last two terms neglected. The system has been calibrated with 23 $\mu\Omega$ niobium thin films at 12 GHz and 4.0 K (the best samples under such conditions), and has a resolution of 5 $\mu\Omega$ with a 12.5 μm Teflon spacer. The temperature dependance can be easily measured between 4 K - 90 K. The change of the loss tangent of the Teflon sheet due to temperature change does not exceed 15%. This method has been considered the most sensitive method developed so far for high-T_c superconductors [33].

Other methods like the stripline resonator and the ring resonator, were also used to measure surface resistance (Table 2-2). Their advantages are: (1) Easy patterning enables selection of any frequency in a wide frequency range, and (2) They could be used for possible applications. Like cavities made from high-T_c superconductors, the results may be degraded by the preparation process [50].

The parallel plate resonator technique is especially efficient for tuning the thin film deposition parameters due to its simplicity and convenience. Although it does not involve metallic material, it does have a Teflon sheet involved. It is easy to use, but has limitations

and pitfalls such as: (1) the precision control of the Teflon sheet thickness for an accurate measurement, (2) the temperature characteristics of its loss tangent, and (3) small particle inclusion. At present, niobium properties under various conditions are understood pretty well. Therefore, it is safe to say that use of niobium is better than most other materials for a highly sensitive and accurate measurement.

2.5 Discussion

As described in last section, all the cavity measurement techniques fall among three categories:

(1) The sample has a small size and is exposed to a known or measurable electromagnetic field. It does not cause significant disturbance to the field distribution, but does cause a fair amount of power loss. The filling factor of the sample is usually small, usually less than 1%. Therefore, the sensitivity is greatly limited unless other measurement methods, for example, the calorimetric measurement method, are used.

(2) The sample is a part of the cavity or resonator, which provides a better sensitivity than the first method due to a larger sample size. It also has a better test geometry, which offers direct comparison for the material under study and the material of the cavity. A disadvantage is that the cavity has the same temperature as the sample, which makes it difficult to have high sensitivity at temperatures higher than T_c's of conventional superconductors.

(3) The entire cavity is made from the same material, which gives overall performance of the device. Because the result reflects the improvement in both the material properties and the process of the device fabrication, it is more appropriate to use the method to test improvement of the material processing and device fabrication.

None of the existing surface resistance measurement techniques could answer all fundamental and practical problems they have faced:

(1) For a given size of epitaxial thin film, e.g., a 25.4 mm diameter disc, what is the R_s detection limit which can be achieved? Is it "impossible" or "impractical" to measure R_s if the film quality is further improved to below 1 $\mu\Omega$?

(2) Measurement results are scattered widely not only because of the differences in material quality, in measurement frequency, etc., but also because of the differences in measurement techniques. The planar resonator techniques have a "long" history of reporting better results than the cavity techniques. Is this because of the edge effect or other reasons related to the cavity methods? Or is it due to lack of correct standards for calibration in the planar resonator methods?

(3) As mentioned in Chapter 1, the f^2-*law* is well accepted and is freely used to extrapolate to 10 GHz. If the best reported results were extrapolated to 1.5 GHz according to f^2, the values would be about 0.15 $\mu\Omega$, which is lower than the BCS value 0.69 $\mu\Omega$ of niobium at 4.3 K. This does not seem to represent the reality of today's level of thin film fabrication.

In summary, all the existing methods are limited in sensitivity for different reasons; but the sensitivity is limited for one reason: an entire cavity cannot be made from high quality single crystal high-T_c superconducting materials. It should be obvious now that an accurate and reliable method is necessary to meet two challenges: (1) measure the surface resistance of planar samples in the sub-$\mu\Omega$ range, and (2) resolve the difference between the results of the cavity method and the planar resonator method. In the coming chapter, we will present our approach to this problem, i.e., a combination of both the RF method and the calorimetry method, which will be described in Chapter 3 and Chapter 4.

Chapter 3

Niobium Triaxial Cavity

3.1 Introduction

As was discussed in Chapter 2, the existing surface resistance measurement methods of high-T_c superconductors face two challenges:

(1) As the sample quality is further improved, a more sensitive method down to sub-$\mu\Omega$ range becomes a necessity;

(2) The background losses need to be further reduced as the sensitivity is improved.

In addition, most of the previously reported results are in the high frequency range (> 10 GHz). This is due to two reasons: (1) A lower resonating frequency requires a larger TE_{011} cavity, which will make the filling factor even smaller for a given size sample; (2) the R_s value itself is smaller for a lower frequency, which makes it even more difficult to detect.

Being aware of these challenges and difficulties, a new measurement technique which combines both the microwave measurement method and the calorimetric measurement method has been devised. It makes good use of the following two achievements in SRF technology:

(1) The well developed cavity fabrication technology: the machining, welding, processing, etc., of niobium are so sophisticated that cavities with complicated shapes can be made with high Q values;

(2) The high resolution temperature mapping system: it has been developed to detect nΩ range residual resistance in superfluid helium. At 2 K, a 1 μK temperature resolution was achieved for a 100 Ω carbon composition resistor [52].

With the RF cavity method and the calorimetry method in mind, the URMEL program [40] has been used to design a triaxial cavity which has (a) a resonant frequency at 1.5 GHz, (b) negligible edge effects on the tested sample, (c) negligible substrate and substrate-film interface losses, (d) negligible losses in the indium joint, and (e) compact size with a reasonable filling factor for the sample. A 16-resistor sensor array is then arranged to measure the RF losses of the sample. The sample and the sensor array are mounted on opposite sides of a thin niobium sheet, and they are located in separate vacuum chambers. The combination of the two methods will not only greatly improve the sensitivity, but also increase the measurement range. Moreover, in the intermediate range where both methods can be used, the measurement reliability will be ensured.

In the coming section, we will first state the design criteria. Then the URMEL design process will be briefly described. The URMEL results will then be discussed in detail, and the temperature distribution and final verification will also be presented. In Section 3.3, we will describe how the cavity, along with the vacuum chamber for the calorimetric measurement, is made and processed. In Section 3.4, the experimental setup for the RF test will be described and the test results at room temperature and 2 K will be compared to the theoretical results. The calorimetric measurement will not be described in detail until Chapter 4.

3.2 Design of the Triaxial Cavity

3.2.1 Design Criteria

As mentioned earlier, the resonant frequency of the new cavity is chosen to be 1.5 GHz. This is based on the following reasons:

(1) The 5-cell niobium cavities used at CEBAF work at 1.5 GHz. The choice can take full advantage of the existing RF measurement equipment;

(2) The measurement will add a valuable data point in the $R_s - f$ curve of high-T_c superconductors [30]. The curve has been short of low frequency points, especially points from high quality thin films;

(3) Only low R_s, which is easier to achieve at lower frequency, could possibly impose a challenge to the calorimetric measurement method.

The following general rules are used for the URMEL calculation:

(1) Reasonable cavity size: this will make the sample's filling factor large enough for the RF measurement in normal cases. In order to achieve this, a *coaxial line structure* will be used because any frequency of interest can be obtained by choosing a relatively short coaxial line length;

(2) Easy fabrication and processing: high quality surface finish and surface cleaning during and after machining are essential for a high Q cavity;

(3) Elimination of sample's edge effect: Samples normally have poor quality on the edge. Possible edge losses, substrate losses, and substrate-to-film interface losses may be responsible for the higher R_s values measured by customary cavity methods;

(4) Low non-reproducible background losses: losses from indium seals should be reduced to a minimal level;

(5) Compatibility with the calorimetry system: the temperature change due to RF heating will be measured on the other side of the cavity wall. To obtain high sensitivity, the sensors glued on the outside wall will be in a vacuum chamber. Moreover, the temperature change should be large enough to be detected, but not large enough to affect the cavity performance by causing BCS runaway.

(6) The coaxial line is tapered to improve the filling factor of the sample, confine high fields to the center portion of the sample, shorten the coaxial line, and preserve sufficient room at the shorted end of the coaxial line for placement of couplers.

Therefore, the design was started from a coaxial line structure with an open end. Outside the open end is an anti-resonant volume where the fields are weak. The sample's edge is located in the outside volume. The indium seal, which is inevitable for a demountable cavity, would not cause any sensible losses due to low fields in this outside volume. The cavity is called a *triaxial* cavity.

3.2.2 URMEL Design

The cavity dimensions are optimized with URMEL [40] due to the cavity's cylindrically symmetric shape. URMEL is a computer code which was written for the evaluation of electromagnetic fields inside cylindrically symmetric structures, such as cavities and waveguides. It uses a simple input file which specifies the shape, the boundary conditions, the modes, and the output format. The input file also includes a namelist **$mesh**. It specifies the points where the fields are calculated. In some cases, only the maximum number of points is needed, leaving the mesh division to the auto mesh generator. In the triaxial cavity design, the small end gap of 1 mm is too small for the auto mesh generator to divide the mesh satisfactorily. Therefore, special attention needs to be paid to the mesh division, especially to the arrangement of the mesh points on the boundary. Appendix A is an example of an input file, a plot of meshes with the cavity, a parameter table which is important to

the cavity design, and the resonant frequencies of some non-cylindrically symmetric modes of the triaxial cavity.

The information which can be obtained from the URMEL output is as follows:

(1) In Appendix A, there is a output table which lists useful parameters such as *mode type, frequency, wavelength, skin depth,* Q, P_{total}, E_{max}, and H_{max}. All results in the table are for copper at room temperature, which uses a conductivity of $\sigma = 5.8 \times 10^7\ (\Omega\text{m})^{-1}$. To convert it to normal conducting niobium or other materials, simply use the formulas in Section 1.2 with corresponding conductivity values.

(2) Figure 3-1 is a plot output of the azimuthal magnetic field ($H_\varphi r = constant$) from URMEL, with the cavity centerline added to the drawing. At the boundaries, the surface current obeys $\mathbf{J} = \mathbf{n} \times \mathbf{H}$, which causes the power losses P_{loss} on the wall. From the values of P_{loss} and Q, the stored energy U can be calculated from eq. (2.2), and C_1 can be determined from

$$U = C_1 E_{max}^2 \tag{3.1}$$

(3) Figure 3-2 shows the electric field where the field strength is represented by the length of each arrow. The electric field has its maximum within the gap. The magnitude of the field strength is inversely proportional to the gap. Because the tested sample will be put on the left plate facing the cone tip, a high field is intentionally created so that a high displacement current will be excited, yielding a radial current on the sample. A small gap is therefore preferred for a larger filling factor. However, a small gap will not only increase the difficulty in machining, but also create problems like field emission and multipacting. A compromise has to be made for the gap.

(4) To calculate the geometry factor of a 25.4 mm diameter sample in the center of the left plate, the program output of the power losses on the walls needs to be used. The maximum magnetic field on the left plate H'_{max} can also be found from the field distribution output.

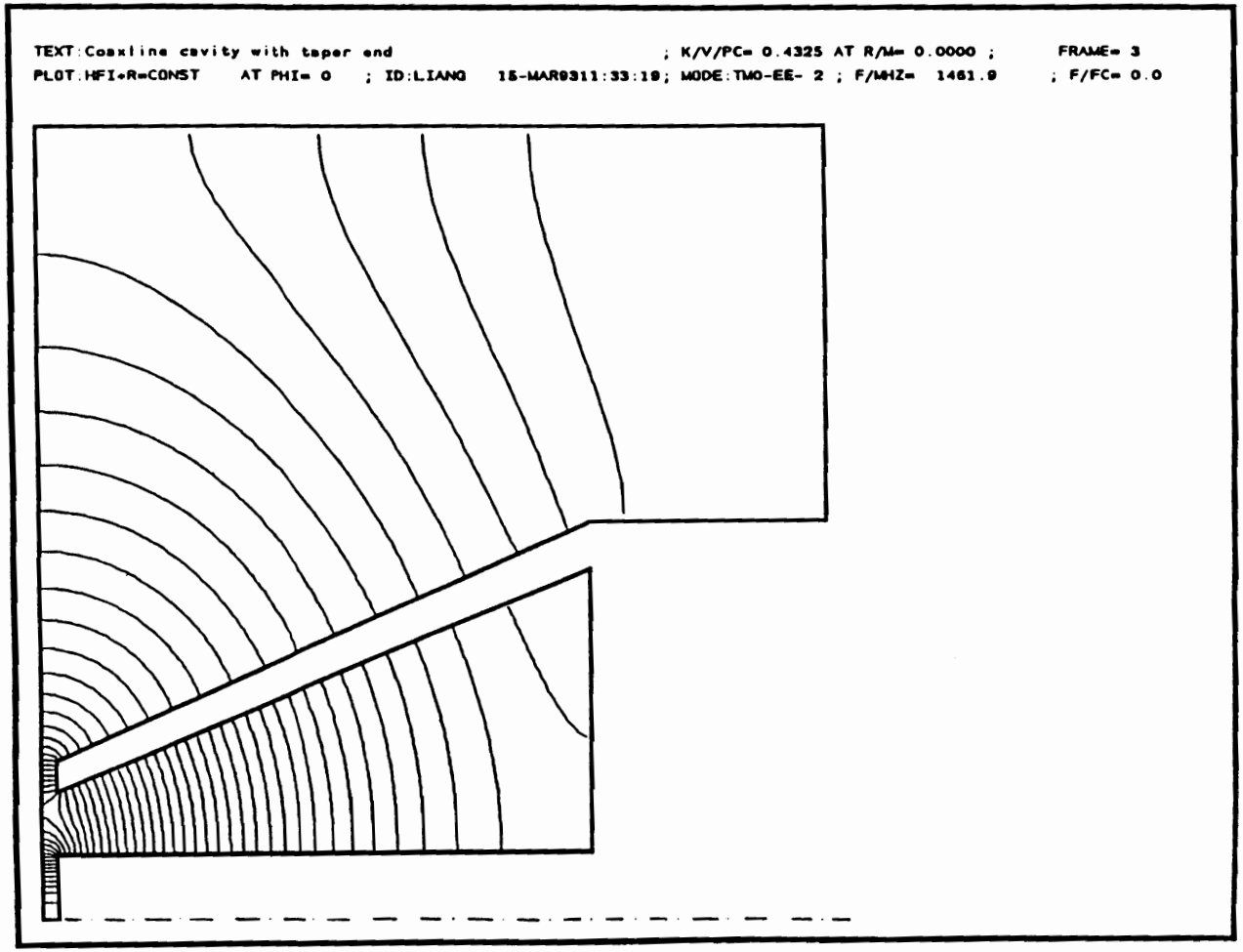

Figure 3-1: Magnetic field component $H_\varphi r$ = constant (triaxial cavity)

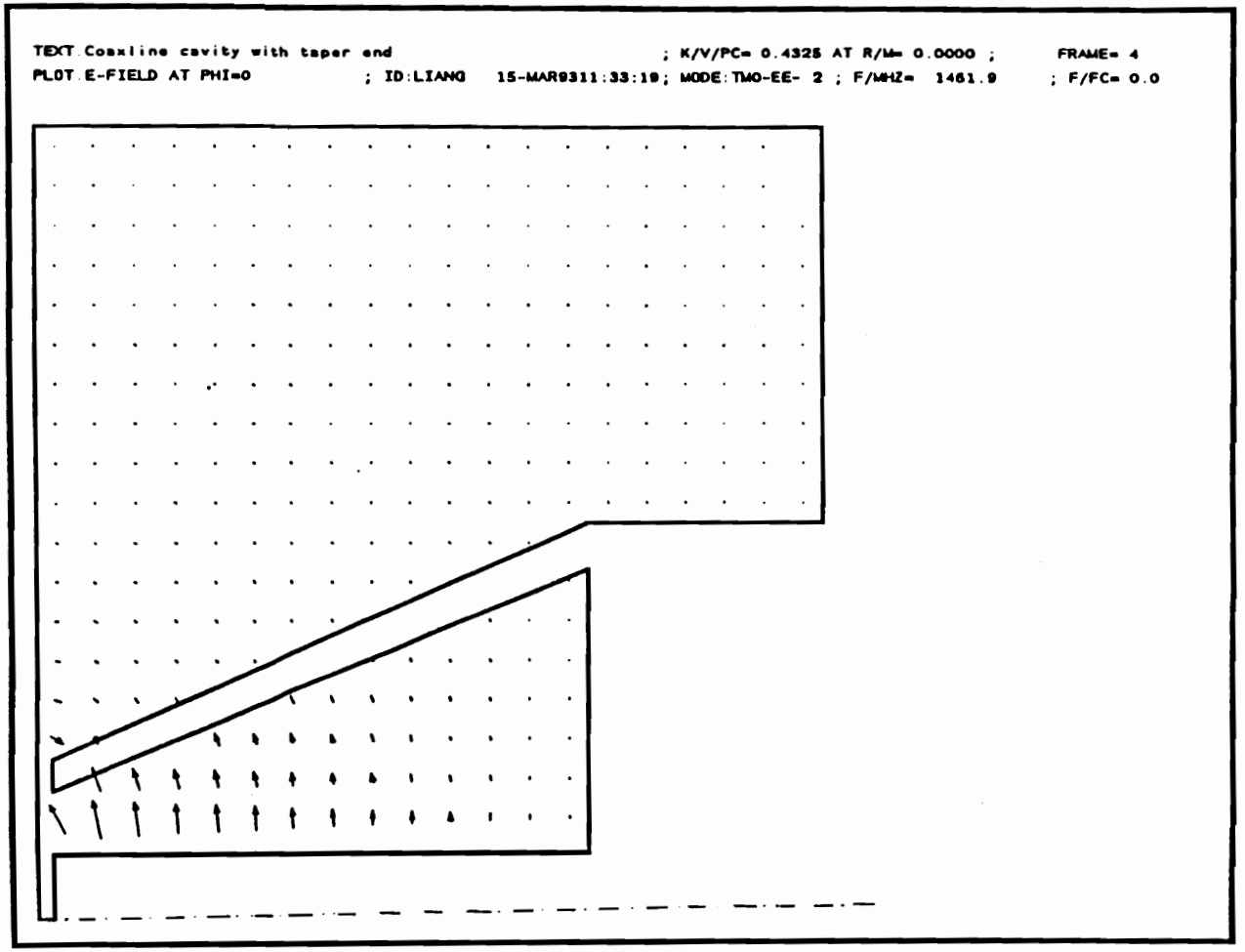

Figure 3-2: Electric field at $\varphi = 0$ (triaxial cavity)

3.2.3 URMEL Results

Role of Different Dimensions

A series of URMEL calculations for different shapes has been performed in order to obtain the least edge effect on the sample, high sensitivity, and easy fabrication. The role of different dimensions had been studied before the final dimensions were decided. The following discussions are about the role of each dimension.

1. The length of the coaxial line d: The resonant mode is chosen to be excited in the center coaxial part. To get a frequency of 1.5 GHz, the length of an open end straight coaxial line is about a quarter of the wavelength, i.e., about 50 mm. Reducing d will result in higher frequency, and it will also reduce the power losses along the line, which will enhance the field strength on the sample placed on the left plate. Two other factors which have an effect on frequency are the concentric radial gap width of the coaxial line and the gap between the small end and the sample. They can be adjusted to shorten the length d.

2. The concentric radial gap width of the coaxial line b: A large width is preferred for two reasons. First, it will reduce the length d for a given resonant frequency and end gap. Second, it will increase the volume-surface ratio, yielding a higher Q of the cavity, or lower background losses. However, the width is limited by the size of the test samples, if the edge effect on the sample is to be minimized. For a straight coaxial line structure, the narrow width would make the magnetic coupling from the cone end impossible. Therefore, an earlier design of a straight coaxial line was changed to a tapered design. This change enhances the sensitivity, shortens the coaxial line, and makes the coupling no longer a problem. By enlarging the coupling side, the coaxial line length is reduced to 35 mm from 50 mm.

3. The gap s between the sample and the tapering end: For a given input power, the electric field strength, and also the surface magnetic field on the sample, is inversely proportional to the gap s. The power loss on the sample is proportional to the square of the surface

magnetic field. Therefore, the gap has a significant effect on the sensitivity, i.e., the filling factor $\eta_i = P_i/P_{total}$. Figure 3-3 shows how the η_i is affected by the gap s, and Figure 3-4 shows the frequency dependance on the gap s. It is obvious that a small gap s is preferred for the sensitivity. Taking into account the machining tolerance capability, a 1.5 mm gap without a sample, or a 1.0 mm gap with a sample, is chosen for the cavity.

4. The radius a of the center conductor: The maximum field strength on the sample is proportional to the radius a when a is small. This is because the field is determined by the current carrying capability of the center conductor. Due to the limited size of the test sample, the radius of the center conductor is chosen as 4 mm.

5. The outer radius R of the triaxial cavity: The field strength on the sample edge reaches its optimum when R is between 50 - 60 mm. The frequency changes very little with R. The outer radius is chosen to be 50 mm.

6. The overall length L of the outer part of the triaxial cavity: If the cavity length L, is longer than the coaxial length d, the loss on the surface of the outer volume will be reduced. Therefore, a length of 50 mm is chosen to match R.

In summary, by choosing a small gap s and a tapered cone for the center line, the coaxial length is reduced to 35 mm from a quarter wave length, 50 mm for a 1.5 GHz cavity. This increases the sample loss P_i and reduces the cavity loss P_{total} and yields a filling factor of about 1% for a 25.4 mm diameter sample located on the center of the left plate. Compared to a straight center coaxial line, the filling factor is increased by a factor of 10, and the coupling to the cavity is no longer a problem. As a result, the power losses on the center conductor and center cone are 94% of the total. The losses are 1% on the sample plate, and 4% on the outside volume boundaries. Figure 3-5 gives the actual dimensions of the cavity.

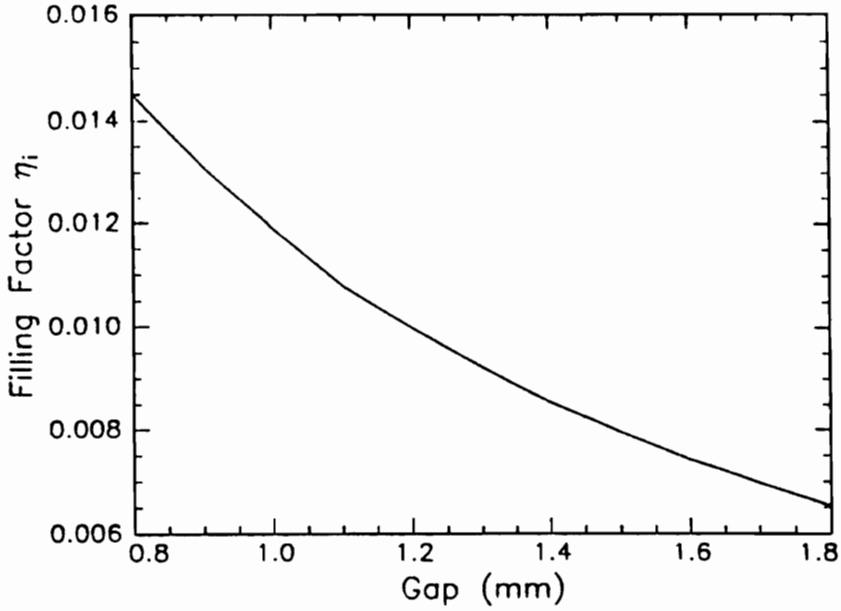

Figure 3-3: The dependance of the filling factor η_i on the gap s (η_i *vs.* s)

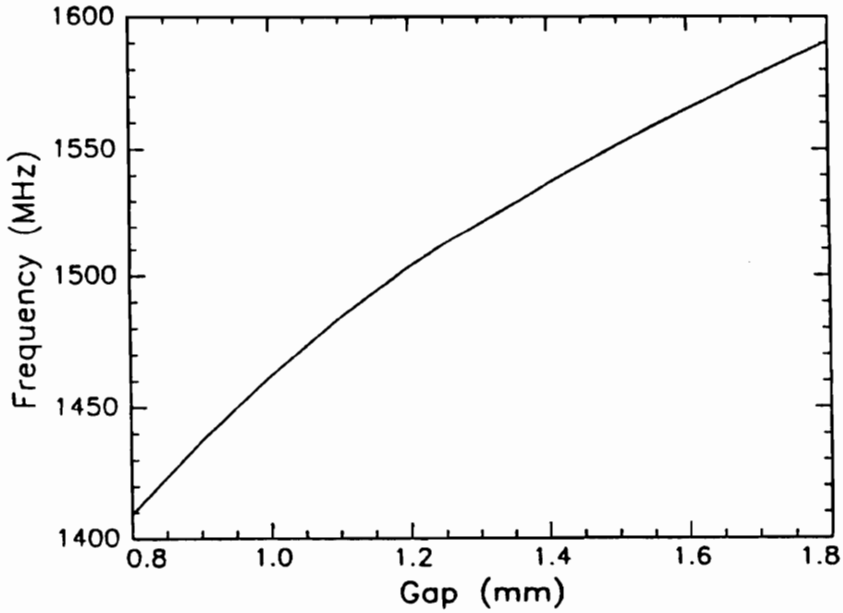

Figure 3-4: Frequency f dependance on the gap s

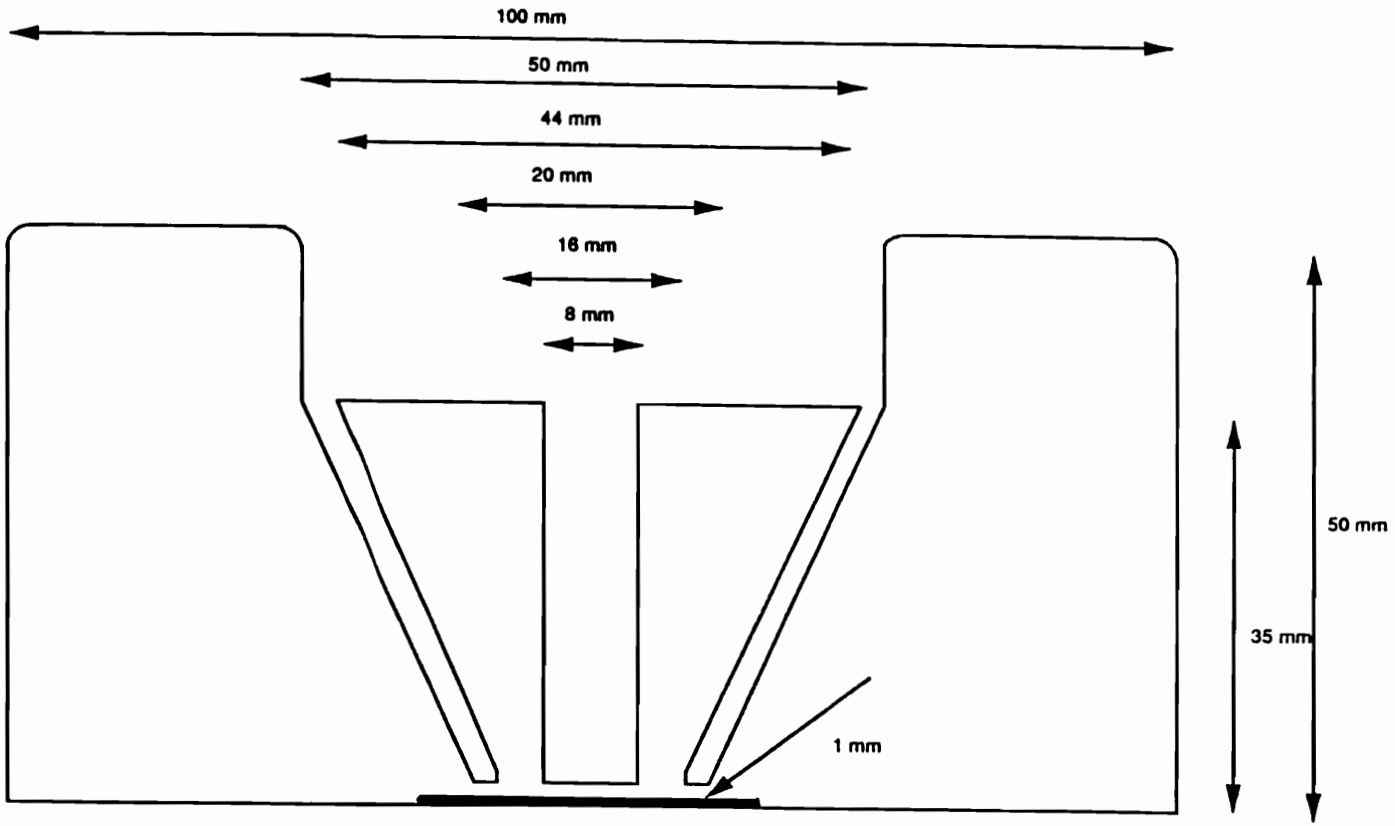

Figure 3-5: Dimensions of the triaxial cavity

Results of Final Dimensions

Based on the dimensions in Figure 3-5, the cavity design parameters, along with those of a TE_{011} cavity which has the same size, are given in Table 3-1. Important design parameters are explained in the following:

(1) From the table, the resonant frequency of the triaxial cavity is 1551.5 MHz without a sample and 1461.9 MHz with the sample. For a TE_{011} cavity with the same size, the frequency would be 4731.9 MHz, three times higher than that of the triaxial cavity. If the gap were larger, the frequency would be less sensitive to the gap. However, a larger gap would reduce the filling factor and increase the field at the edge of the sample and at the indium seal.

(2) The geometry factor G is 44.75 Ω without the sample. Given the conductivity of niobium (8×10^6 $(\Omega m)^{-1}$), the room temperature Q is 1662. If the surface resistance is 112.5 nΩ at 2 K, the number used in CEBAF's design for the BCS surface resistance plus the residual resistance, the Q at 2 K is 4.0×10^8. For the TE_{011} cavity, the Q would 15 times higher.

(3) To build up the same 10 MV/m field, the 1.5 mm gap requires 75% more power coupled into the cavity. As pointed out before, the same electric field gradient gives approximately the same surface magnetic field H'_{max}, or the same displacement current, which is shown in the second last line of the table.

(4) The highest magnetic field H_{max} is at the cone's larger end, which is 73.7 Oe and 93.5 Oe for gaps of 1.0 mm and 1.5 mm, respectively. Good cooling conditions are required in order to avoid thermal magnetic breakdown in that location.

(5) The maximum magnetic field on the sample is 23.6% for a 1.0 mm gap and 17.8% for a 1.5 mm gap of the maximum field. This is lower than other Q-perturbation methods because elimination of the edge effect has a higher priority in the design.

Table 3-1: Parameter comparison of the triaxial cavity and a same size TE_{011} cavity

Parameters	Triaxial (gap = 1.0 mm)	Triaxial (gap = 1.5 mm)	TE_{011} R = L = 50 mm
frequency (MHz)	1461.9	1551.5	4731.850
Q	4350	4475	66623
G (Ω)	43.50	44.75	666.23
P_{loss} (W)	163.45	281.12	182655
P_{plate} (W)	1.940	2.239	52540
η_{plate}	1.187%	0.796%	28.76%
E_{max} (MV/m)	10.00	10.00	10.00
H_{max} (Oe)	73.72	97.52	666.46
U (μJ)	75.439	133.5	4.1×10^5
C_1 (μJ/(MV/m)^2)	0.754	1.335	4100
H'_{max} (Oe)	17.40	17.26	666.46
$\eta_{25.4mm}$	1.050%	0.700%	

(6) The final filling factor of a 25.4 diameter sample is about 1%. This is acceptable when compared to the 1.23% filling factor of the 820 MHz $\lambda/4$ TEM cavity [46], which had the sample placed in its maximum magnetic field location. In the triaxial cavity, the 1% filling factor is achieved when the sample is purposely placed in a weaker field location inside the cavity. $\eta_{25.4mm}$ in the same size TE_{011} cavity is not given due to its non-symmetric position.

The Field Distributions

As shown in Figure 3-1, the central coaxial cone is excited in the TEM mode at 1.5 GHz. The magnetic field of this mode has its maximum on the larger end of the cone. It is circumferential and gradually decays along the cone, dropping dramatically within the gap. On the left plate where the sample will be placed, the field increases from zero at the center to its maximum on the plate at a 6.25 mm radius from the center and is about 18% of its maximum value at the larger end of the cone. Then the magnetic field decreases to zero and changes its sign at about 20 mm from the center. This is where the real radial current has a zero and the edge effect is completely eliminated. Figure 3-6 shows the normalized power dissipation density $p(r)$ on the left plate, which is the heat source for the temperature distribution on the plate (see 3.2.4). It can be seen that when a sample's radius is larger than 12.5 mm, the RF loss at the edge is greatly reduced, and is zero at 20 mm. The outer volume has a low field distribution and has been designed to make the indium joint loss small. The magnetic field at the indium seal is about 1.2% of the maximum field inside the cavity, or about 5% of the maximum field on the plate. It will be shown in Section 4.6 that when the surface resistance is in the $\mu\Omega$ range, the indium joint losses are negligible. Even when the indium losses are not negligible, the effect on a calorimetric measurement is very small because of the proximity of the indium to the helium bath.

The electric field has its maximum between the top plate and the cone tip. Possible multipacting or field emission may limit the cavity performance. In the worst case, a dielectric layer (e.g., TiO_2) could be coated to reduce the secondary electron coefficient.

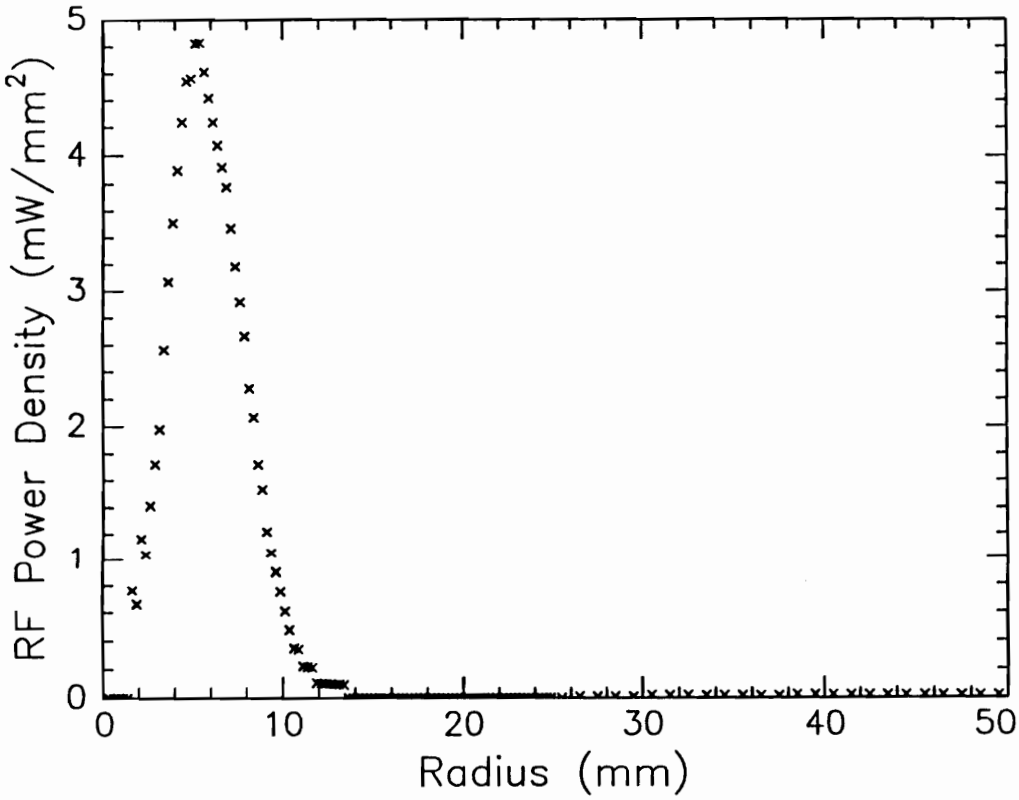

Figure 3-6: Normalized power density $p(r)$ on the sample plate

Sensitivity of the RF Method

When Q is larger than 1×10^6, Q is measured by the transient response method. The time constant for the decay is measured by an oscilloscope. Suppose the resolution of the Q measurement is limited by the oscilloscope to about 5%. Then the resolution for a 25.4 mm diameter sample would be $\Delta R_s = 5\, R_{Nb}$ (eq. 2.31). If R_{Nb} is 100 nΩ, the detection limit would be 600 nΩ. This resolution limit could be reduced by digitizing and fitting the decay signal, but errors introduced by opening the cavity (to install the sample), thereby contaminating the surface and altering the R_s everywhere, would quickly limit the accuracy.

3.2.4 Temperature Distribution due to RF Heating

After the major dimensions of the triaxial cavity are determined, the diameter of the temperature sensor chamber needs to be determined. In order to avoid the influence of the indium joint losses on the temperature distribution, the inner diameter of the sensor chamber is chosen to be 8 cm, 2 cm smaller than the inner diameter of the cavity. This will provide enough space to accommodate the 16 temperature sensors, build up a high enough temperature in the center, and give a long enough path to let the heat produced by the indium joint losses be carried away by the superfluid helium [52]. The complete structure of the system is shown in Figure 3-7.

The thermal conduction in a cylindrically symmetric thin plate is defined by the equation

$$\dot{q}(r) = -\kappa \frac{dT}{dr} \tag{3.2}$$

and the boundary condition of $T(r_0 = 40 \text{ mm}) = T_0 = 2.0$ K. The solution is given by:

$$T(r) = T_0 + \int_r^{r_0} \frac{\dot{q}(r')}{\kappa}\, dr' = T_0 + \int_r^{r_0} \frac{\dot{Q}(r')\, dr'}{\kappa\, 2\, \pi\, r'\, h} \tag{3.3}$$

where $\dot{q}(r')$ is the heat flux per unit area per second at r', while $\dot{Q}(r') = \dot{q}(r')\, 2\, \pi\, r'\, h$ is the heat flux across the ring section area per second; κ is the thermal conductivity of the reactor

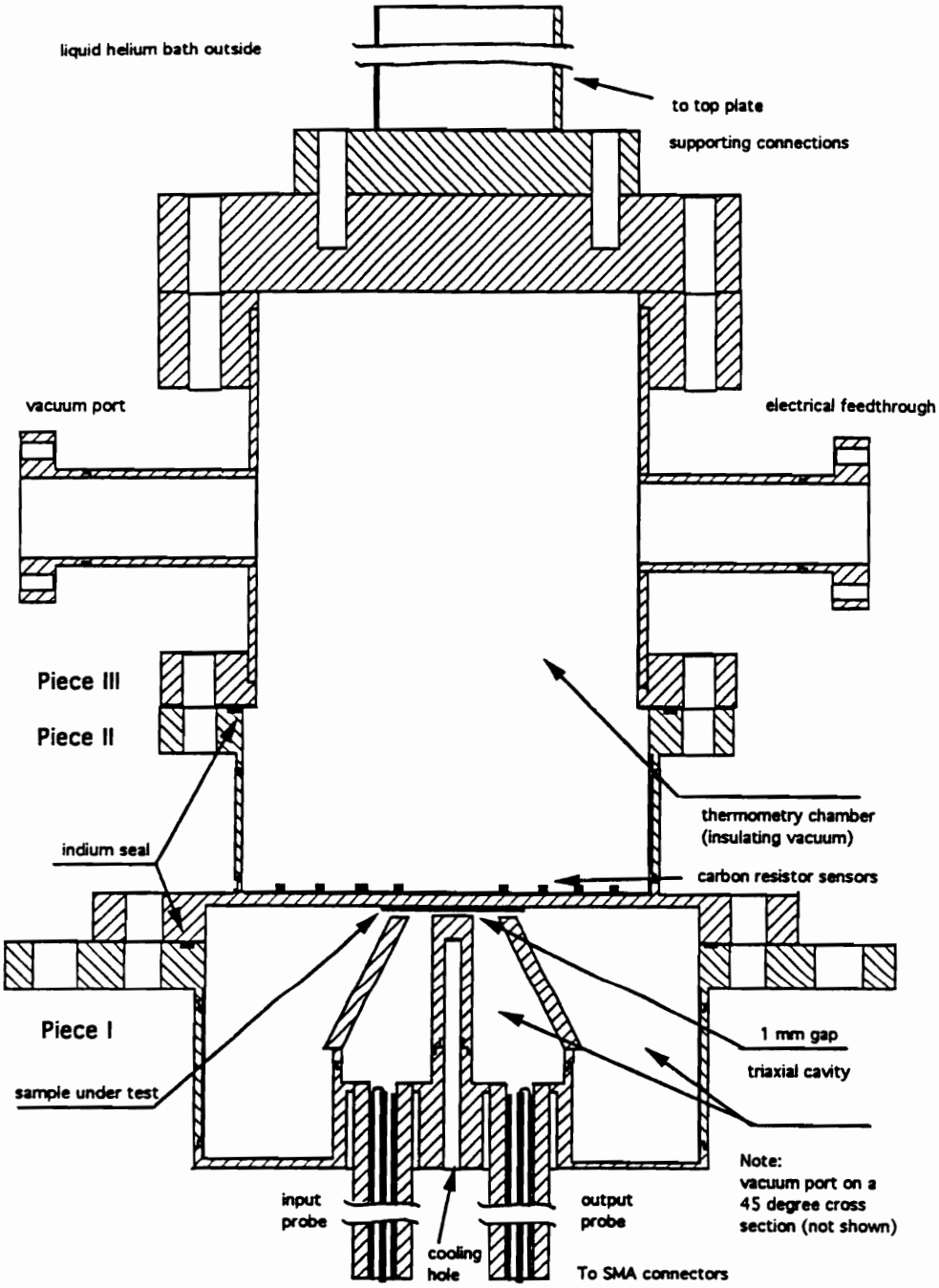

Figure 3-7: Configuration of the triaxial cavity and the sensor chamber

grade niobium, and h is the thickness of the plate. The relation between the heat flux across the ring section per unit time and the power dissipation density from the URMEL result is:

$$\dot{Q}(r) = \int_0^r 2\,\pi\,x\,p(x)\,dx \tag{3.4}$$

Given $p(r)$ (Figure 3-6), κ, and h, the temperature distribution $T(r)$ on the plate can be easily obtained by integrating a double integral (Section 4.1.2).

It is assumed in eq. (3.3) that the temperature distribution along the z direction is independent of z. This is because the radius r_0 (40 mm) is much larger than the thickness h (1.6 mm). The temperature change is expected to be a few or a few tens of mK, so that the thermal conductivity κ is nearly a constant in the measurement. Otherwise, $\kappa(T)$ would have to be used in the integration.

At 10 MV/m, the total loss in the sample plate will be 1.94×10^{-5} W, assuming a sample surface resistance of 100 nΩ. Taking $\kappa = 0.03$ W cm^{-1} K^{-1} and $h = 0.16$ cm, this power dissipation will result in a temperature change of 1.09 mK in the center of the plate. If the resolution for the temperature change is 2 μK, the resolution will be 0.02 nΩ at a field level of 30 MV/m. This estimate shows the sensitivity of the calorimetric measurement.

3.2.5 Possible Limitations to Cavity Performance

The cavity performance was evaluated before the fabrication process, based on knowledge of field limiting phenomena such as field emission, magnetic breakdown, BCS runaway, and multipacting. The necessary steps have been taken to raise the limitation levels.

Field Emission Limitation

Field emission occurs at extremely high field levels (above 100 MV/m), when electrons are extracted from the metal by the high field. The extracted electrons will then be accelerated

by the high field, causing one of the several kinds of anomalous losses, known as non-resonant electron loading. This kind of high field level usually exists at sharp corners which have very small curvatures.

In the triaxial cavity, the electric field has its maximum within the small gap (Figure 3-2). All the corners at the rod and cone tips have been rounded to increase their curvatures. Small particles, which sometimes have a large secondary electron emission coefficient, have to be cleaned away through repetitive rinsing in deionized water and ultrapure methanol. As a conservative estimation, a peak field of 10 MV/m was used as the maximum expectation value.

Thermal magnetic breakdown

As mentioned in Section 1.2, RF losses are proportional to the square of the surface magnetic field. When a normal inclusion exists at the surface, that location may be overheated so that it heats its neighboring region to above 9.2 K. Then a thermal breakdown can occur, making the whole cavity turn normal. This is why high RRR (residual resistance ratio) niobium materials are used in the CEBAF 5-cell cavity; high thermal conductivity niobium spreads out the heat faster, and enhances the thermal magnetic breakdown threshold [53]. In the triaxial cavity, reactor grade niobium materials were used because of availability. This will make the thermal breakdown problem occur even more easily. In addition to the two coupling holes which help to cool the center block, a hole has been drilled in the center rod, cooling both the rod end and the highest magnetic field regions. For the tapered cone, the thickness at the larger end is 3 mm, while the thickness on the smaller end is 2 mm. Nevertheless, nothing could be done to the thin sample plate because the temperature gradient on the plate is purposely created, except for careful cleaning to reduce the number of such normal regions. Empirical estimation for the thermal breakdown field is 100 Oe, which is larger than the conservatively estimated 10 MV/m limitation, i.e., 73.7 Oe. (Table 3-1).

BCS runaway

Even though there are no external particles on the surfaces of high field regions, poor cooling may still result in a magnetic breakdown of the cavity, which results in BCS runaway. This is caused by RF heating from BCS surface resistance. The heating increases the temperature, which further increases the BCS surface resistance. When the magnetic field exceeds a certain value, this process becomes a positive feedback loop, and finally causes BCS runaway. One of the advantages of having the cavity work at 2 K is that the cavity has a higher BCS runaway threshold field level than it does at 4.2 K. Another solution is to improve the cooling condition, which has been described in the last paragraph. Two possible places for global BCS runaway are the cone tip and the center of the sample plate (BCS runaway at the bottom plate can be avoided by reducing the field strength). A rough estimation with an iteration program based on equation (3.3) and an approximate formula for R_s *vs.* T gives a minimum field threshold of 53 MV/m for the cone tip. This is much larger than the 10 MV/m field emission limitation. Therefore, BCS runaway does not impose any potential limitation to cavity performance.

Two point multipacting

Three conditions have to be met for two point multipacting to occur: (a) the secondary electron coefficient has to be larger than one; (b) the electron travel time between these two points equals an odd half integer number of rf-periods; and (c) The phase is proper in order to establish the two point resonant electron loading. When multipacting happens, all the extra energy coupled into the cavity will be absorbed by the multipacting site. Therefore, the field is no longer increased with the increased coupling power. While in field emission, the field keeps increasing with increasing power, but the Q drops more rapidly because the emission current increases exponentially with the field level.

Because of the high electric field and the geometry of the gap between the cone tip and

the sample plate, two point multipacting is very likely to happen at the gap. A computer program was written to study the possible multipacting based on [54]. The result predicts that only the first order multipacting could happen due to the small gap and high field in the gap. The multipacting barrier is between 0.3 MV/m to 0.5 MV/m, and depends on the specific secondary electron emission characteristics of the surface.

In summary, the two magnetic field related breakdowns are not as important as the two electron loading phenomena. The multipacting problem usually disappears at high field – when the electron energy is so high that the secondary electron coefficient is smaller than one. A low secondary electron coefficient dielectric coating could be deposited on the plate or on the sample to reduce the coefficient if the multipacting were a problem. For the field emission problem, there is little that can be done except for more chemical etching and cleaning.

3.3 Fabrication and Processing

3.3.1 Cavity Structure Design

Parts Design

The structure design process depends on the availability of the material. Reactor grade niobium was used for the sample plate because of its relatively low thermal conductivity, and was used elsewhere because high RRR niobium would have required a special order. The niobium pieces used are 1.27 cm and 5.08 cm diameter rods, 0.16 cm and 1.27 cm thick sheets, and a 15.24 cm diameter round bar. They were machined into eleven pieces: two cylindrical walls, three flanges, two RF coupling tubes, one vacuum tube, one center rod, one tapered cone, and one center block joining the center rod, cone, and the three coupling ports. They are joined by ten electron beam welds (permanent) and five indium

seals (demountable). Three indium seals are for vacuum and coupling ports, and two for the two separate demountable chambers. All the electron beam welds require full penetration to avoid cracks which would trap chemicals, and the indium wire used for sealing is 0.10 cm in diameter. No vacuum leak has ever developed in any of these permanent or demountable vacuum joints in approximately 20 tests in 2 K superfluid helium.

From now on, the pieces which will be addressed frequently will be described according to their sequence shown in Figure 3-7. The sample plate will be called *the top plate*, the larger end of the cone *the bottom of the cone*, the smaller end of the cone *the cone top*, the part joining the center pieces *the center bottom*, etc.

Coupling Ports

The two RF coupling ports are located at the bottom of the cone where the magnetic field has its maximum. Because the available width at the cone bottom is 1.8 cm, the diameter of the coupling holes is only 0.46 cm. The magnetic coupling probe is a loop shorted at the end of a customized stainless steel transmission line with a characteristic impedance of approximately 50 Ω . The fabrication of the transmission line is described in Appendix B. The diameter of the line is 0.40 cm. The line has eight 1.27 cm long spring fingers located at 0.31 cm from the end which provides electric contact with the niobium tube wall and provides alignment. The electric contact prevents any mode from being excited between the transmission line and the niobium tube. To avoid the dust and niobium chips which might be scraped off by the spring fingers, the cavity is placed with the coupling probes positioned below the cavity. Each probe is adjustable through a stainless steel bellows, which is welded to an SMA connector through an adaptor.

Because the vacuum port is located on the outside volume where the magnetic field is weak, the diameter of the port can be a little bigger for the sake of pumping speed. The diameter is 0.95 cm and the length to diameter ratio is 5.9.

Tuning Mechanism

In order to have flexibility tuning the gap, the center bottom piece has a 0.16 cm thickness at the bottom. With a tuning bar, the gap can be adjusted at room temperature for minor frequency tuning. This, together with the 0.16 cm thick top plate, makes the cavity very sensitive to the outside pressure.

3.3.2 Machining and Welding Processes

Machining Requirements

After the dimensions of the cavity were determined, a detailed component design was done for machining purposes. The following are the requirements for the cavity machining:

(1) After cleaning, welding and assembling, the gap between the cone top and the top plate will be 1.5 mm. The mechanical design needs to take into account the welding shrinkage of 0.25 mm, the compressed indium wire thickness of 0.28 mm, the chemical etching before the welding, and the 0.43% thermal contraction of niobium. The chemical etching process after the welding does not change the gap because every surface is etched away by the same amount.

(2) The cavity has to have the highest practicable cylindrical symmetry, especially for the center rod and the tapered cone. Both the radius of the rod and the width of the radial gap at the cone top are 4 mm. The symmetry of the center rod is of great importance.

(3) The surface finish has to be smooth and the parts should be handled with great care to keep them scratch free. The center cone is especially important because of the high magnetic field distribution.

To achieve the requirements, the following specifications and procedures have been set for the design:

a. Practical specification for machining: only the dimensions which specify the inner surface of the cavity require a very strict tolerance of 0.0254 mm (0.001″);

b. Preparation for full penetration electron beam welding: all the welding steps are 1.14 mm by 0.79 mm (0.045″ by 0.031″);

c. Procedures which guarantee the highest practical cylindrical symmetry and flatness of parallel flanges for indium wires. This will be accomplished through a special machining-welding procedure, which will be described below.

d. When necessary, the machined parts are smoothed with a 3M wheel to mechanically clear off unevenness and other kinds of minor damage.

Machining and Welding Steps

To ensure the final cavity will be made as specified, the machining process takes several steps.

(1) The pieces making up the bottom part were first machined. The welding sequence was the three coupling tubes, the center rod, and the tapered cone. The rod and the cone were intentionally left longer at the first machining. They were machined to the proper length at the last step. The rod could be aligned to its center if there was any deformation due to the welding shrinkage.

(2) The upper welding preparation of the cavity wall was machined after the cylindrical wall was welded to the bottom part. This guaranteed the symmetry of the outside wall.

(3) The bottom flange was machined after the last welding of the cavity wall, together with the center part and the top plate of the cavity. This ensured that the gap was correct, and that all the cylindrical parts were aligned properly.

In summary, due to the complicated structure and the strict cleaning requirement, the cavity was assembled in several steps. Parts were first machined, then chemically polished, and then welded. Then the cavity was further machined several times before reaching the final dimensional specifications. As a result of the design, there is only one indium seal which is exposed to a magnetic field, and that field is very weak. Joints at the highest magnetic field region are made with full penetration welds.

3.3.3 Chemical Processing and Assembling

The purpose of chemical processing and cleaning is to remove minor mechanical defects, impurities on the surface, or the surface contamination. This is an inevitable step because contaminants are responsible for non-reproducible phenomena like Q degradation, thermal breakdown, electron loading, etc.

After all the welds were complete, the cavity was chemically polished in a 1:1:1 solution of concentrated phosphoric acid, nitric acid, and hydrofluoric acid for 1 minute. It was then rinsed in deionized water for several hours to rinse off the acid residue. Before assembling the cavity in a clean room, it was ultrasonically rinsed in deionized water for two to three hours and again in high purity methanol for half an hour.

When the cavity performance deteriorates after several measurements, another half a minute of light etching in the 1:1:1 acid solution is performed. It proves to be effective for improvement of the cavity Q, i.e., for the reduction of the anomalous losses in the cavity. The total thickness removed by etching is about 100 μm.

3.4 RF Test of the Triaxial Cavity

In this section, the experimental setup will be described. The cavity test results at room temperature and 2 K will be presented and discussed.

3.4.1 Cryostat Insert

The whole assembly, the triaxial cavity and the temperature sensor chamber, is mounted to a cryogenic insert. The insert is then put into Dewar I, one of the eight big cryostats used for cavity testing and other activities at CEBAF [55]. It has an inside diameter of 40.6 cm and a depth of 182 cm.

The top plate of the insert has several vacuum ports for couplings between the cryostat and the outside world. They are used for: (1) pumping of the cavity and the sensor chamber (2 ports); (2) rotational mechanical feedthrough for the adjustment of the RF coupling probes (2 ports); (3) RF feedthroughs which are used for the input cable and the pickup cable (2 ports); and (4) electronic instrumentation feedthroughs for the carbon resistor sensor signals, the germanium calibration sensor (2 ports), and the calibration heater. One of the pumping lines also supports the whole setup through a 3.8 cm diameter stainless steel tube (Figure 3-8).

To reduce the thermal radiation loss between the liquid helium and the top plate, ten aluminum baffle plates are used between the cavity and the top plate of the insert. This also reduces the temperature fluctuation due to reduced heat exchange.

Semirigid ISOCORE^{TM} cables were used because of their working stability at 2 K. They were bent with several loops so that they were flexible enough to move with the probe adjustment. The probe positions are adjusted through a fixture which converts the rotational movement of the mechanical feedthrough to the translational movement up and down. The adjustable range is 3 cm, which covers the range of -6 dB to more than -106 dB.

3.4.2 Vacuum

Both the cavity and the sensor chamber are under vacuum when the measurement is performed. The cavity and the sensor chamber are prepumped with a turbopump and then

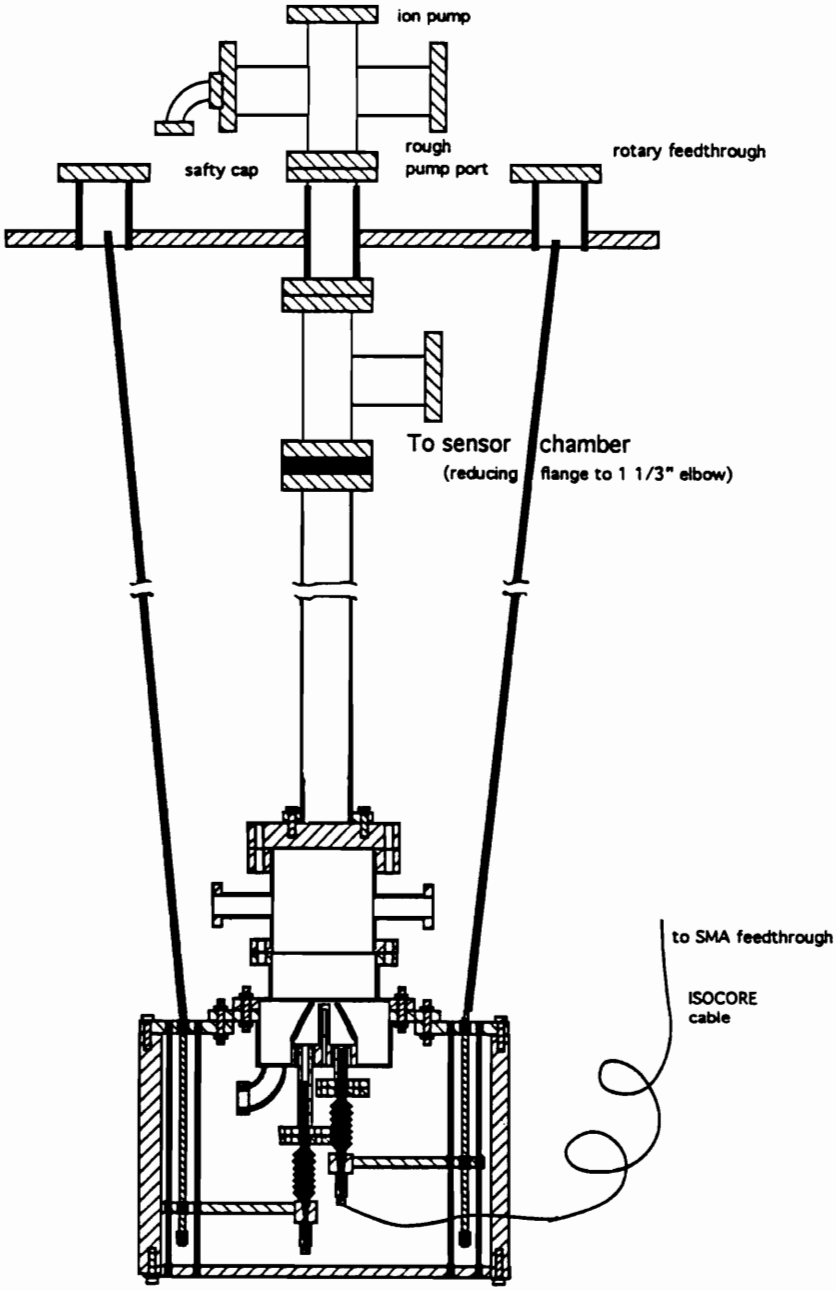

Figure 3-8: Cryogenic insert for 2 K measurement

with two separate ion pumps. The pumping speeds of the ion pumps are 20 l/s and 11 l/s, respectively. At room temperature, the vacuum before cooling is usually 3.0×10^{-7} Torr for the cavity and 2.0×10^{-6} Torr for the sensor chamber. The latter is poorer because the GE varnish used for glueing temperature sensors has a large gas desorption rate. The vacuum readings at the pumps for both chambers at 2.0 K are in the low 10^{-8} Torr range, due to the cryopumping effect.

It was found that the cavity pressure before cooling is very critical because the adsorbed gas layer formed during cooling of the cavity top plate causes multipacting between the top plate and the tapered cone tip (Section 4.6). The poorer the vacuum before cooling, the longer the time it takes, using heavily coupled RF power, to process it. Therefore, it is preferable to pump overnight before the cavity is cooled down.

3.4.3 Room Temperature Measurement

Because the niobium cavity has a Q of only a few thousand in its normal state, a network analyzer (HP85047A) is used to conduct the room temperature measurement.

The resonant frequency f and the Q were measured by a transmission measurement. Figure 3-9 shows the resonant peak of the triaxial cavity. The frequency was tuned to 1499.964 MHz with the tuning bar. At room temperature, when both the cavity and the cryostat are under vacuum, the resonant frequency is 1523.7 MHz. The resonant frequency is at 1499.4 MHz when the evacuated cavity is in a 730 Torr cryostat (room temperature). The frequency change due to pressure is about 33.3 kHz/Torr, because both the top and the bottom of the cavity are intentionally thin (1.6 mm thick). As a comparison, the 5-cell CEBAF cavity has a pressure coefficient of only 66 Hz/Torr. The sensitivity to the pressure would cause inconvenience to measurements at 4.2 K. However, at 20 torr (about 1.96 K), the pressure fluctuation is very small, and the resonant frequency is very stable.

The average unloaded Q_c from a variety of room temperature measurements is 1600. This

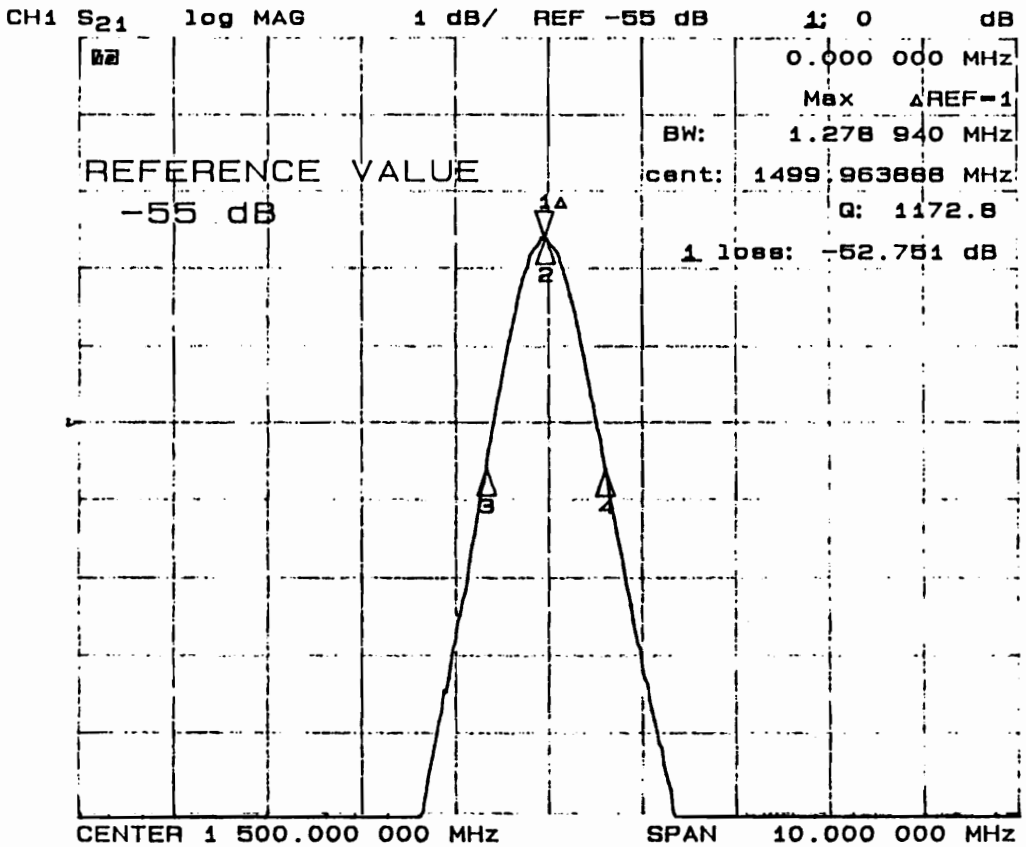

Figure 3-9: Resonant peak of the triaxial cavity

yields a geometry factor of 43.1 Ω, which is only 23.7% away from the expectation value (Table 3-1).

The Q measurement at room temperature is believed to be reliable because: (1) the Q values are consistently smaller than the expectation value, (2) all the G values are within 4% error, indicating the network analyzer has high stability and reproducibility, and (3) the transmission loss measurement is very reliable because $\beta_1 \ll 1$ and $\beta_2 \ll 1$, and does not require calibration as the reflection measurement does. In reality, a number of network analyzer parameters have to be optimized for an accurate Q measurement, including SPAN, IF bandwidth, power level, scale and reference level, etc.

The f value is lower than the expected 1551 GHz. This is due to the two RF coupling holes. As a whole, the specified dimensions of the cavity were completed within expectation.

3.4.4 RF Measurement at 2 K

Cooling

The insert has been described in 3.3.1. It is cooled by a closed cycle cryogenic system which can reach 1.5 K. The working temperature is chosen at 2 K because the carbon composition resistors which will be used have high enough sensitivity in this region, the BCS surface resistance of niobium is small, and the cooling capability of superfluid helium is good. The pressure of the cryostat is regulated by a stepping motor controlled valve. The temperature fluctuation at 2 K is less than 2 mK, which is measured by our carbon composition resistors and also by a calibrated Lakeshore germanium resistor sensor (GR-200A-500). In addition, the vapor pressure can be used as a temperature indicator. The cryostat has a usable volume of 136 liters, and does not require refilling for 12 hours. This is more than enough for pumping down to 2 K, doing calibration of the carbon resistor sensors for each run, and measuring the RF losses at different couplings and different field levels. The cryostat was

magnetically unshielded for the first tests. The residual magnetic field from the building where the cryostat is located is 4 to 8 Gauss. Later it was shielded with two layers of 0.08 cm thick μ-metal sheets and several compensation coils. The residual magnetic field after shielding is 6 mGauss.

RF Measurement Setup

When Q is larger than 5×10^6, it is measured by the transient response method. RF power is turned on and off in a pulse mode, so that the loaded Q of the cavity can be measured from the field decay time (eq. 2.3). Figure 3-10 shows the fundamental parts of the RF measurement system. Components like isolators (isolating the power source from power reflected from the load), attenuators (controlling power level), switches (selecting CW/pulse mode), etc., are not shown in the figure.

The microwave source is a 1.3 - 1.7 GHz voltage controlled oscillator (VCO). The output signal is sampled for feedback and frequency measurement with two directional couplers. Then the signal is amplified by a power amplifier with a constant gain, the output of which is controlled by a variable input signal. At the cryostat, a directional coupler is used for measuring the incident power to the cavity and the reflected power from the cavity. The transmitted power is split into two parts. One is directed to a power meter for measurement and to a diode for decay measurement. The other goes to one leg of the double balanced mixer (DBM), where it combines with the sampled VCO output passing through a phase shifter. The output of the DBM contains a dc signal which reflects the phase difference caused by any frequency fluctuation. This DBM output passes through a low pass filter, and is amplified and sent back to control the oscillator frequency. As a result, the output of the VCO is phase locked to the cavity resonant frequency.

The resonant frequency f is measured with a HP 5342A frequency counter and the decay time constant τ is measured with an oscilloscope. Incident, reflected, and transmitted power

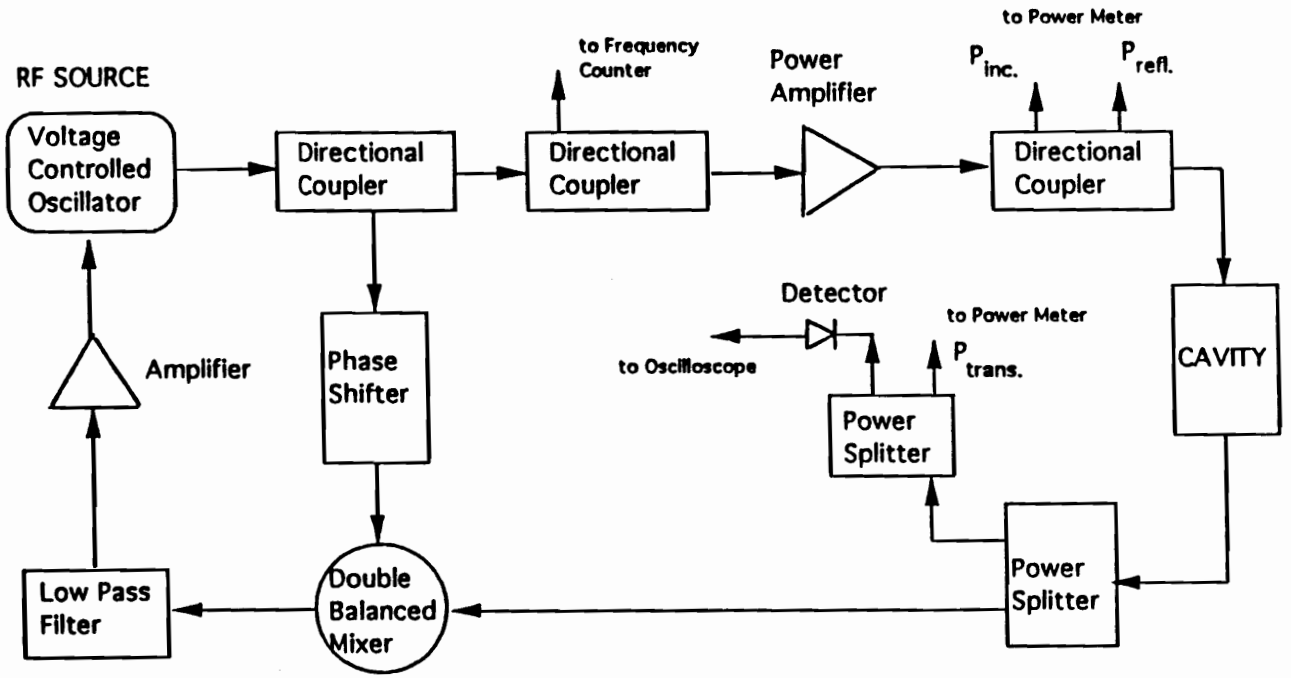

Figure 3-10: Schematic diagram of the RF measurement system

are measured with an HP 436A power meter. The power loss P_{loss} within the cavity and the coupling factor β_1 of the input probe can then be calculated from equations (2.21) and (2.22). With $Q_c = \omega\tau(1+\beta_1)$ and $U = C_1 E_{max}^2 = Q_c P_{loss}/\omega$, the Q_c of the cavity and the maximum electric field can be obtained, where C_1 is a constant determined by URMEL calculation (Table 3-1).

Special attention is paid to the measurable quantities like Q, β_1, $P_{inc.}$, etc., which determine the ultimate accuracy of the measurement. Errors from these quantities will be discussed in Chapter 5.

Measurement Results

Table 3-2 presents the measurement results at 1.96 K and 4.3 K when the cryostat was unshielded and shielded. As it can be seen, in the unshielded case, the R_s at 1.96 K is five times as high as that of the shielded case. This is because the surface resistance was dominated by the residual resistance caused by magnetically trapped flux. The best Q achieved in the unshielded case was measured at a field level of 5 MV/m. For the shielded case, the Q value did not start to degrade until 15 MV/m (Figure 3-11). The highest E_{max} achieved in the cavity is more than 30 MV/m, which is three times as high as the conservatively expected value. It also means thermal magnetic breakdown was successfully suppressed through careful design. At the 30 MV/m field level, Q is lowered by the temperature increase of the tapered cone, the field emission in that region, and possible probe losses. Below 5 MV/m, multipacting dominated the performance. The limiting field of the multipacting was measured to be 0.43 MV/m once, which is within the program estimation in Section 3.2.5.

The surface resistance calculated from Halbritter's program [24] is 0.69 $\mu\Omega$ and 9.2 nΩ respectively for 4.30 K and 1.96 K when using $T_c = 9.2$ K, $\Delta/kT_c = 1.86$, $\lambda_L = 33$ nm, $\xi = 38$ nm, and $\ell = 10$ nm. It is worth mentioning that the BCS surface resistance is also

Table 3-2: Test results of the triaxial cavity at 1.96 K and 4.30 K

	unshielded		shielded	
	1.96 K	4.30 K	1.96 K	4.30 K
f_0 (MHz)	1525.455	1515.100	1524.222	1513.510
Q_c (10^6)	20.0	6.6	110	30.0
E_{max} (MV/m)	5		15.0	
R_s ($\mu\Omega$)	2.24	6.78	0.41	1.49

sensitive to the mean free path ℓ. Figure 3-12 shows the relation between R_s and ℓ at 4.3 K.

Although the surface resistance at 1.96 K was dominated by some anomalous loss mechanisms, the 0.4 $\mu\Omega$ background is still good enough for measurements of high-T_c superconducting samples. As discussed earlier, the Q measurement method should have a detection limit of 2.4 $\mu\Omega$ in such a background. After the description of the calorimetric measurement in the coming chapter, the measurement results of high-T_c superconducting thin films will be presented in Chapter 5.

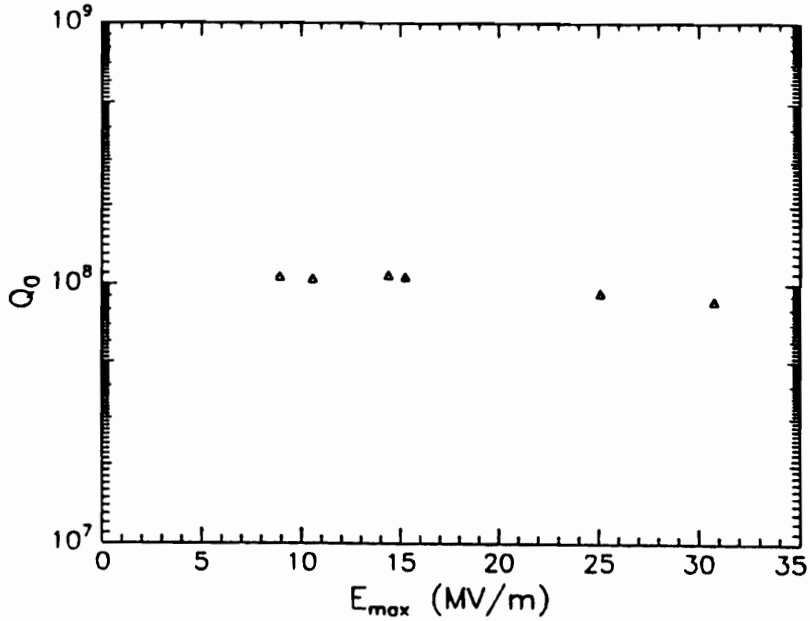

Figure 3-11: Q_c *vs.* E_{max} (the triaxial cavity)

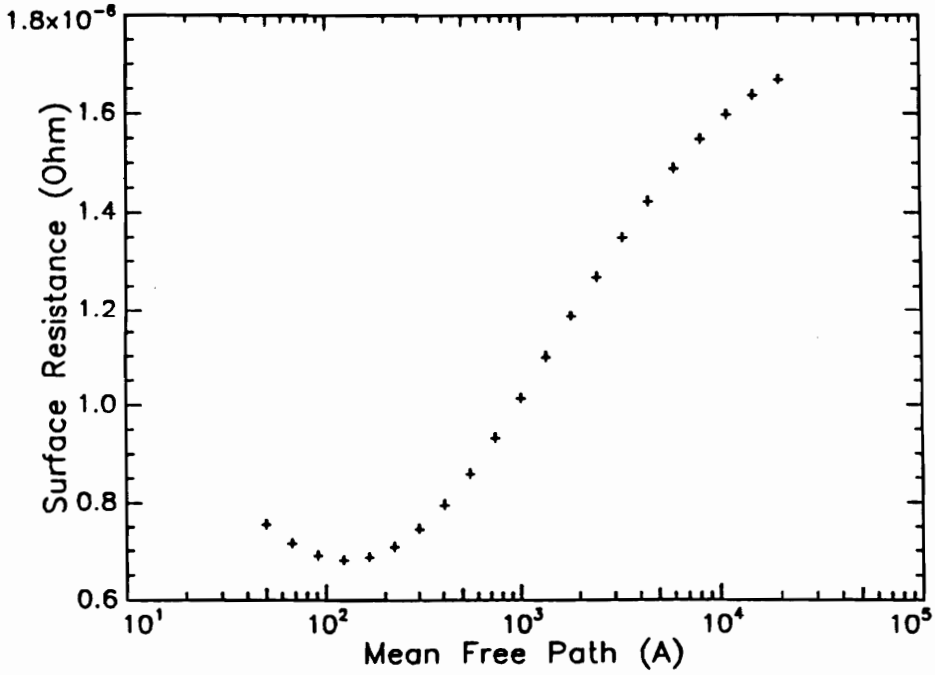

Figure 3-12: Surface resistance R_s *vs.* mean free path ℓ

Chapter 4

Calorimetric Measurement

4.1 General Description

4.1.1 Introduction

As mentioned in Chapter 3, if the Q measurement has an accuracy of 5%, the best sensitivity which could be achieved by RF measurement in the triaxial cavity for a 25.4 mm diameter sample is 6 R_{Nb}. This is 2.4 $\mu\Omega$ in the best case. On the other hand, if the calorimetric measurement method is used, assuming the carbon resistor sensors in use have a resolution of 2 μK at 2 K, at a maximum electric field level of 10 MV/m (surface magnetic field of 17.3 Oe), the R_s resolution would be 0.18 nΩ, which is more than three orders of magnitude lower than the RF measurement method.

Temperature mapping has been used for diagnosing lossy spots in subcooled helium (pressurized liquid above the λ-point of 2.17 K) [56] and studying residual resistance in superfluid helium (below the λ-point) in superconducting RF technology [52]. In the superfluid case, the system was capable of detecting a residual resistance of 50 nΩ at a surface magnetic field of 20 Oe. Because the carbon resistor sensor was located in superfluid helium, it had an

efficiency of 50% to 60% when compared to fully insulated model calculations. The reproducibility of the temperature mapping depended on two important factors: (1) the sensor has good thermal contact with the metal surface, and (2) the sensor is well insulated from the superfluid helium. Due to bath temperature fluctuations, the lower detection limit of the system lies at about 100 μK, corresponding to losses of a few μW at the lossy spot. During the measurement, 100 sensors were scanned in 20 to 50 minutes because each sensor's resistance was measured with a balanced bridge, which took time to reach compensation for each sensor.

A calorimetric technique measuring surface resistance of superconducting thin films was developed for improving the composition of Nb_3Sn thin films [57]. The measurement was performed in an OFHC copper cavity, which had a resonant frequency of 8.6 GHz in the TE_{011} mode. The sample was a long film slab which was located along the whole axis. The RF losses on the sample were measured by comparing it with that of a computer controlled dc heater. Germanium sensors were used to measure the ratio of the RF losses and the dc heater power. The reported dynamic range of the surface resistance was 1 nΩ to 1 Ω.

The calorimetry method used with the triaxial cavity (Figure 3-7) has the following features and advantages:

(1) It is extremely sensitive. The sensitivity of the 100 Ω 1/8 W Allen-Bradley carbon resistor has been reported having a resolution of 1 μK [52]. Due to the vacuum insulation, the temperature change caused by RF heating is built up along the radius, instead of a localized Gaussian peak like the distribution in superfluid helium. Moreover, the efficiency of the temperature sensor is nearly 100%, which greatly improves the reproducibility and reliability of the measurement.

(2) It is very accurate. The quantity measured is the temperature change, not the temperature. This will greatly simplify the measurement and the calibration process. The temperature change is proportional to the surface resistance at a given field level (eq. 3.3).

(3) It is not affected by other possible loss terms like probe loss, indium joint loss, etc. It only measures the intrinsic losses of the sample. In other words, the P_{sample} measured is only from the sample in the calorimetric measurement, while in the RF measurement P_{sample} can be measured accurately

$$P_{loss} = P_{cavity} + P_{sample} + P_{indium} + P_{probe} + \cdots \tag{4.1}$$

only when P_{cavity}, P_{indium}, and P_{probe} are reproducible, and P_{sample} is a significant fraction of the total loss. This not only puts restraints on the measurement but is also difficult to achieve. In ref. [52] mentioned above, indium joint losses in a 4 GHz TE_{011} cavity were observed as one of the major loss mechanisms being detected.

In this chapter, the calorimetric measurement method used to measure P_{sample}, or P_{plate} (RF losses of the cavity top plate) when the gap is 1.5 mm, will be described step by step. In the following parts, the expected temperature distribution from the URMEL result and the mapping sensor arrangement will be described. The next three sections will introduce three fundamental steps involved in any temperature and temperature change measurement: (1) choosing the sensor which is appropriate in the temperature range of interest, (2) measuring the signal from the sensor, and (3) the conversion of the signal into temperature. In Section 4.2, the carbon resistors used in the measurement will be described. Then the measurement method of a 4 by 4 temperature sensor array will be discussed in Section 4.3. This includes the development of a customized scanning board and automated data acquisition. In Section 4.4, the calibration procedure will be described, which establishes the signal-temperature relation for the conversion. In Section 4.5, the results from both heater calibration experiments and the RF losses will be presented and discussed. The agreement between the two serves as an overall calibration for the complete measurement system and the calorimetric method. In the last section, all results will be summarized.

4.1.2 Temperature Distribution of RF Heating

Temperature distribution of the top plate caused by RF heating can be calculated from eq. (3.4).

$$T(r) = T_0 + \int_r^{r_0} \frac{\dot{q}(r')}{\kappa}\, dr' \;=\; T_0 + \int_r^{r_0} \frac{\dot{Q}(r')\, dr'}{\kappa\, 2\, \pi\, r'\, h}$$

If there is no isolated lossy spot, field emission, or multipacting on the top plate, the temperature distribution is cylindrically symmetric and is shown in Figure 4-1 (1.5 mm gap). In subsequent discussions, it will be used as the theoretical model to calculate the RF losses on the plate. To obtain a surface resistance from the measurement, the following quantities are required: (1) the temperature change $\Delta T(r)$ due to RF heating, (2) the product κh (the thermal conductivity and the thickness of the top plate), and (3) the maximum electric field E_{max} in the cavity. The measurement of E_{max} was described in Section 3.4, and the measurement of $\Delta T(r)$ and κd will be described in the following sections.

4.1.3 Sensor Arrangement

The sensor arrangement and the wire connections are shown in Figure 4-2. Sensor scanning is started with the first row (1, 5, 9, 13), then (2, 6, 10, 14), etc., and the signal is measured, converted, saved and presented in sequence from 1 to 16 in the LabVIEW program, which will be explained in detail in Section 4.3 and Section 4.4.

In the measurement, RF power is in the ON/OFF pulse mode, which is the basis of the ΔT measurements. Data acquisition continues through a computer controlled process. Figure 4-3 shows a simulated temperature change due to RF heating. The acquired points in the upper level and in the bath level are then averaged for good signal-to-noise ratio, which yields 2 μK or better resolution.

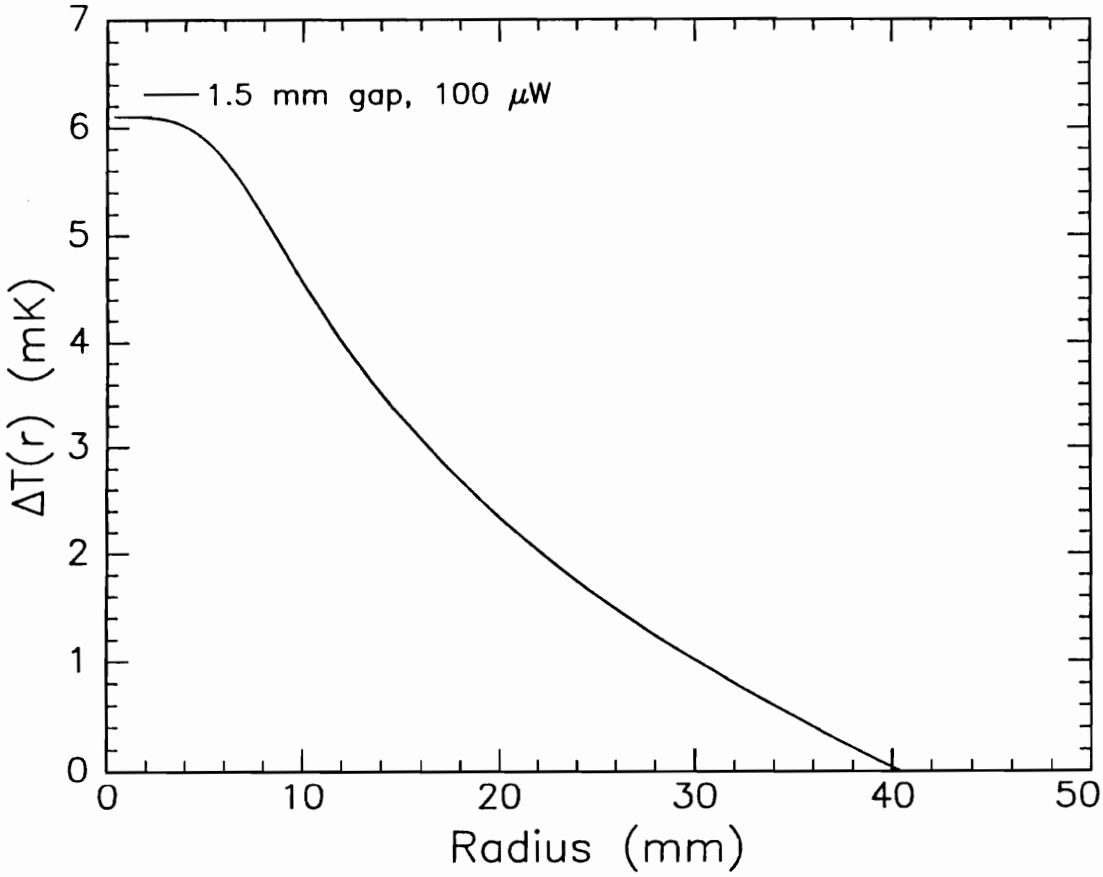

Figure 4-1: Temperature change distribution of the cavity top plate

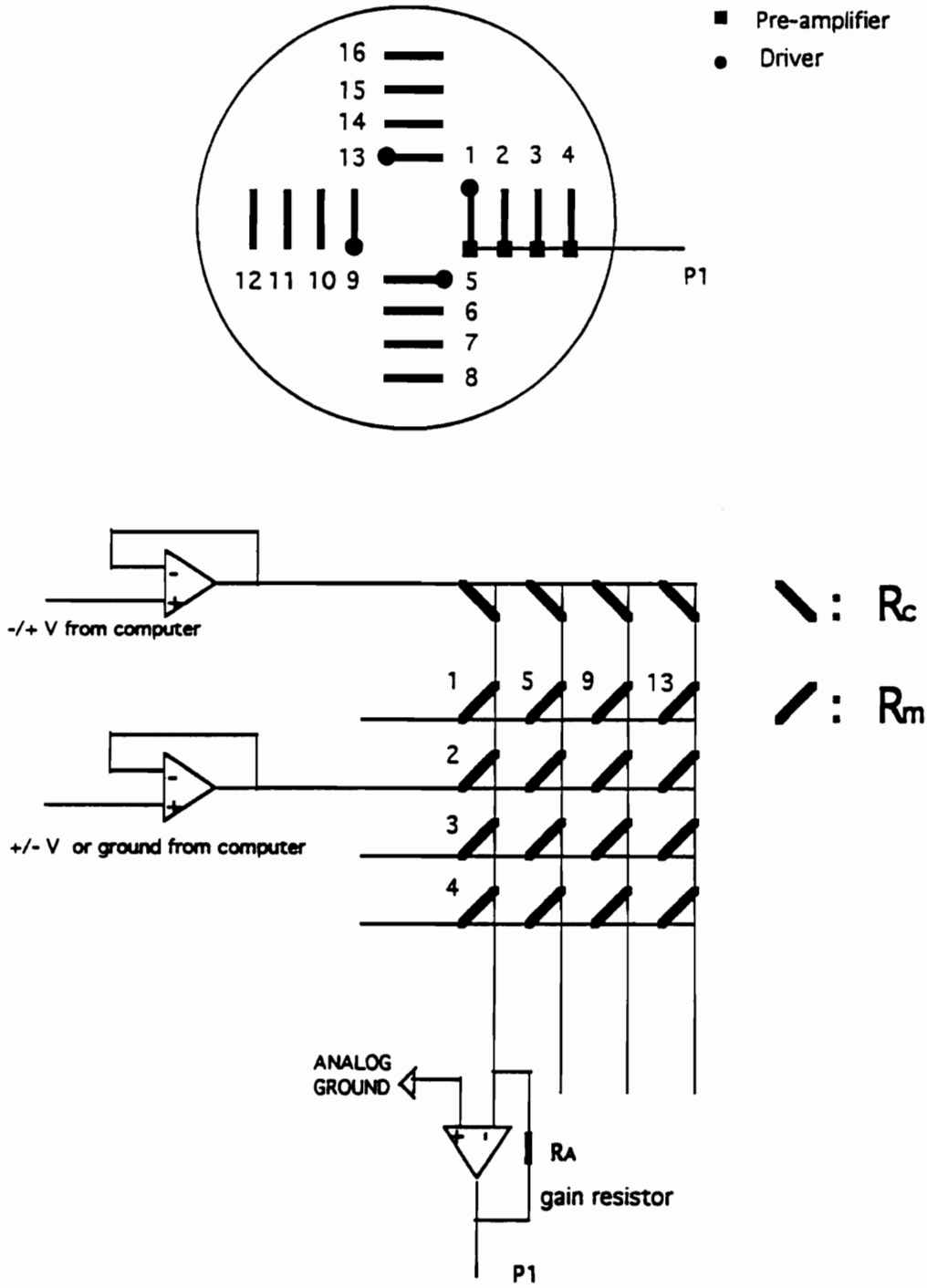

Figure 4-2: 16 sensor arrangement and labelling for temperature mapping

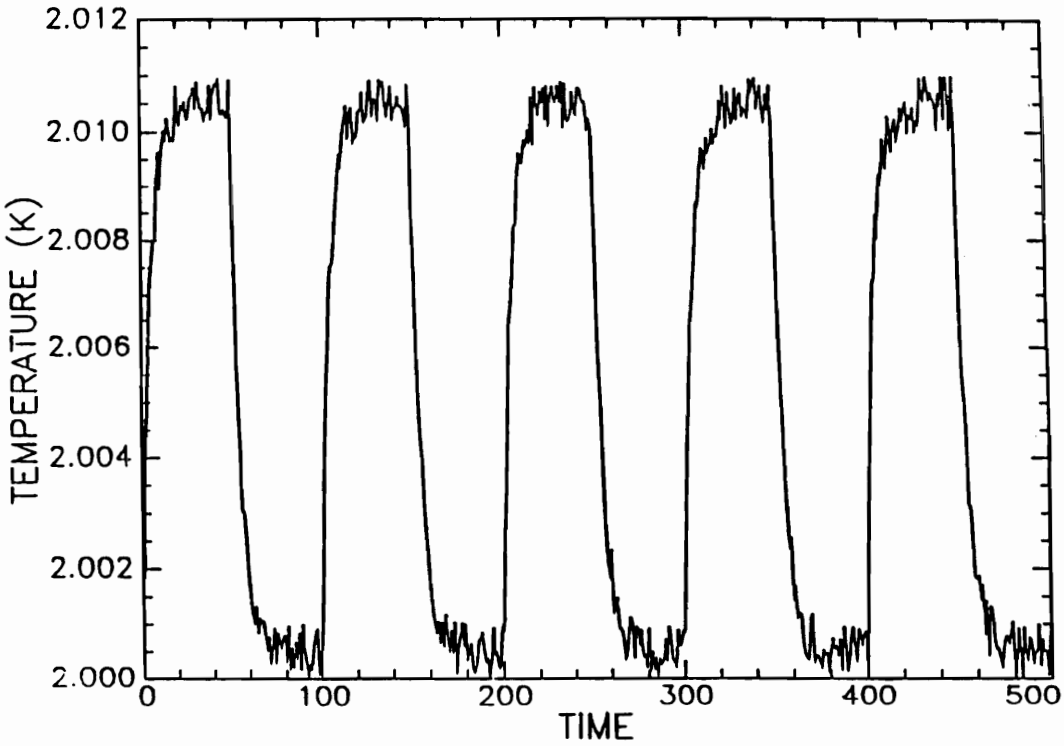

Figure 4-3: Simulated signal with bath temperature fluctuation

4.2 Carbon Resistor Sensor

4.2.1 Carbon Resistor for Calorimetry

The temperature–resistance characteristics of carbon composition resistors have been well studied because of their high sensitivity at low temperatures (< 6 K) and their cost effectiveness (at least 10^3 times cheaper than commercial sensors) [58]. The problems associated with the carbon resistor sensors are the stability and the reproducibility. Namely, the sensors have a drifting problem during each run, and have different resistance values between different runs. These two problems are detrimental for any precise measurement of thermometry, but should have little effect on calorimetry. The reasons are as follows:

(1) Thermometry requires accurate temperature measurement. To get an accurate reading, the sensor needs to be calibrated by a standard, which is either primary, secondary, or a reasonable working standard. Usually, the temperature characteristic of the working standard (the shape of the R(T) - T curve) does not change, but it is very difficult to prevent small shifts due to aging, stress, or different working conditions. In the calorimetric measurement, any small shift in temperature reading is cancelled in the temperature change. The temperature change is proportional to the corresponding heating power, or the surface resistance.

(2) The temperature change is measured in consecutive power ON/OFF cycles. Each cycle takes about one minute. In such a short time, there is almost no drifting related to the carbon resistor sensors.

(3) The sensors are calibrated for each run by a Lakeshore germanium resistance sensor. Therefore, the accuracy of the measured temperature change is approximately the same as that of the Lakeshore calibrated germanium sensor. With the aid of computer controlled data acquisition, the calibration is no longer a complicated task as it was before.

4.2.2 Sensitivity

The relative sensitivity of the calorimetric measurement depends on two factors, the sensor and the measurement system. It can be represented by:

$$\frac{\Delta T}{T} = \left(\frac{T}{R}\frac{dR}{dT}\right)^{-1}\frac{\Delta R}{R} = \left(\frac{d\,lnR}{d\,lnT}\right)^{-1}\frac{\Delta R}{R} \tag{4.2}$$

where the $(d\,lnR/d\,lnT)$ is known as the specific sensitivity of the sensor, which is material dependent but independent of the geometry of the sensor; $\Delta R/R$ is the resolution of the measurement system, which will be discussed in Section 4.3.

The carbon resistor sensors used in the calorimetric measurement are Allen-Bradley 100 Ω, 1/8 W, 5% resistors. At 2.0 K, the specific sensitivity is about 3, and the resistance is between 6500 Ω and 7500 Ω. Figure 4-4 gives the temperature characteristics of four carbon resistor sensors used in the experiment. The temperature range shown in the figure is the calibration range, which is about 140 mK. In normal measurements, the temperature change caused by RF heating is between 10 and 20 mK.

When the resistance change due to RF heating is measured, the simplest way to get the temperature change is to use equation (4.2), with the specific sensitivity calibrated earlier. The accuracy of the result will be good enough if the measurement range is small enough. This simple conversion method will not be used in this thesis because the convergence of the following expression

$$\Delta R = \frac{dR}{dT}\Delta T + \frac{1}{2!}\frac{d^2R}{dT^2}(\Delta T)^2 + \cdots \tag{4.3}$$

is not fast enough; the $(n+1)th$ order derivative is always larger than the nth order derivative (dR/dT changes 32% in the calibration range). If $\Delta T = 10$ mK, the error from the second term would be about 0.7% (given $(d^2R/dT^2)/(dR/dT) = 1.4$). The resistance–temperature conversion, or the calibration, will be discussed in Section 4.4.

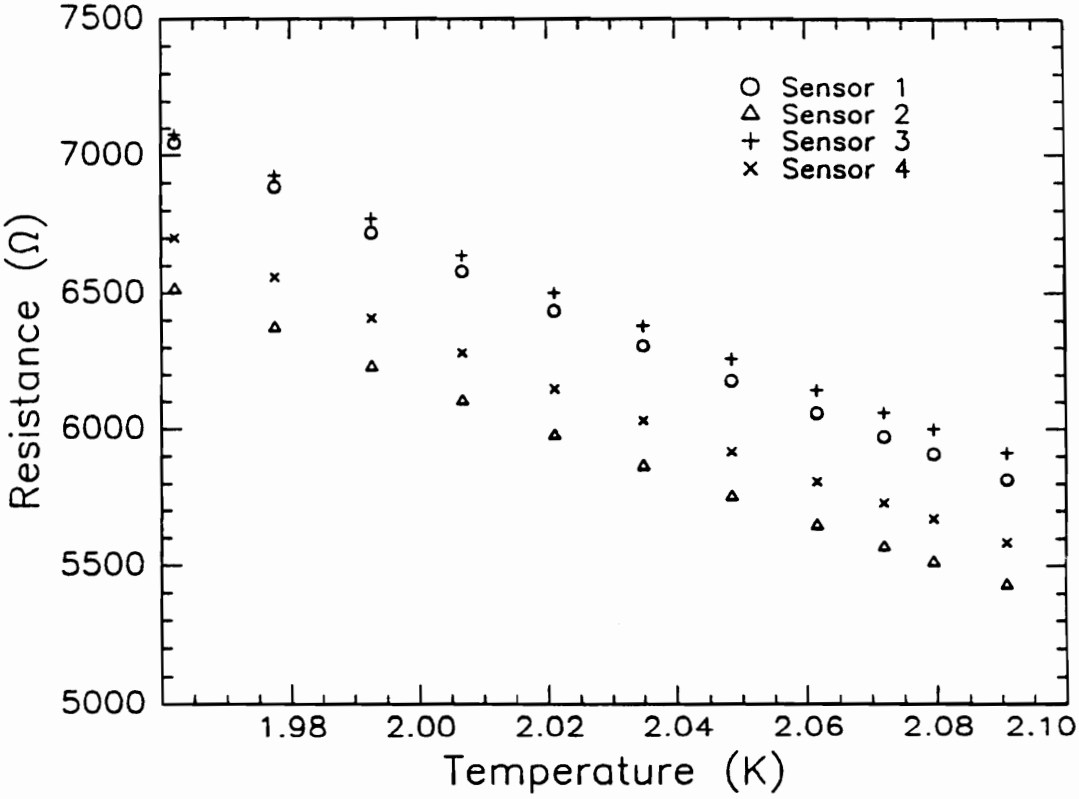

Figure 4-4: Temperature characteristics $R(T)$ *vs.* T of carbon resistor sensors

4.2.3 Preparation

Except for the high sensitivity, carbon resistor sensors have to meet other requirements as cryogenic sensors:

(1) small size: small thermal mass or thermal capacity;

(2) short time constant: good and uniform thermal conducting path besides small thermal capacity.

To meet these requirements, the insulation layer of the carbon resistors was ground off. Because the carbon core has a large thermal impedance, a 0.3 cm diameter (O.D.) copper tube was used to house the sensor. This not only results in more uniform thermal conduction around the sensor but also protects the sensor from infrared radiation and mechanical damage. Dessuga δ-bond was used as the thermal agent and the electrical insulation layer between the copper housing and the sensor. In addition, the copper housing was flattened on one side in order to improve the thermal contact between the sensor and its attached metal surface.

Measurement errors related to cryogenic sensors and their mounting are as follows:

(1) Self heating: This should be as small as possible so that the sensor's reading reflects the temperature of the tested body. The driving current of the sensor, or the driving voltage, is determined by the compromise of the self-heating effect and the range of the signal. Once again, the temperature change measurement has the advantage of eliminating small self-heating effects.

(2) Heat leak from the lead wire: The sensor's reading should not be disturbed by any heat sources except the tested body. Wires of high electric and thermal resistance are usually used for lead wires, and good thermal grounding needs to be ensured.

The lead wire used for the sensor was 42 gauge constantan wire. The wire soldered to each end was about 20 cm long. At room temperature, the resistance of a 100 Ω resistor was 110

Ω after grinding off the insulation layer. After soldering the two lead wires, the resistance was about 130 Ω. The sensors were then cycled 20 times between the room temperature and the liquid nitrogen temperature. If the electric insulation between the carbon core and the copper housing was still good after thermal cycling, the sensor would be used for the calorimetric measurement.

4.3 Data Acquisition

4.3.1 Temperature Mapping

To measure the resistance of a resistor sensor, the most commonly used configuration is the 4-wire configuration shown in Figure 4-5. It has the advantage of not including the lead wire resistance and the contact resistance, and is especially useful for small resistance measurements, such as the superconducting transition measurement of R(T) *vs.* T. In the experiment which will be described below, this method has been used to measure the resistance of a Lakeshore calibrated germanium resistance sensor, which is used as a working temperature standard.

If this method were used for 16 resistor sensors, there would be 64 wires coming out from the cryostat. This would be a source of heat leak in addition to wiring difficulty. In ref. [52], the 100 temperature sensor mapping was finished with a two-lead configuration, with 100 sensors sharing a common ground. Two 60-pin feedthroughs were used for the 100 mapping sensors, the 10 reference sensors, and a germanium sensor for calibration. Also shown in Figure 4-5 is a simplified diagram of its measurement principle. One of the arms was a computer controlled programmable resistance and the other was the temperature dependent resistance R(T). The resistance was measured when a bridge was balanced in two arms. The method used a Keithley 706 Scanner to select the sensors and a lock-in-amplifier to monitor the balancing.

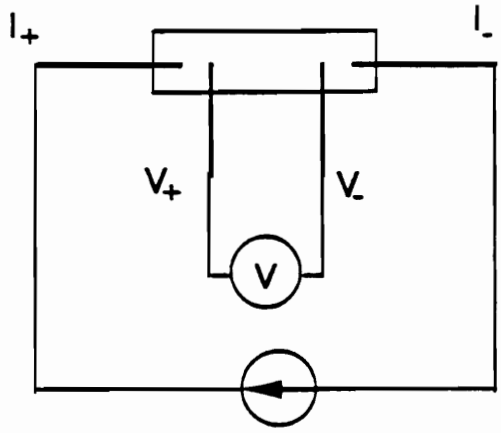

a. Four-lead resistance measurement

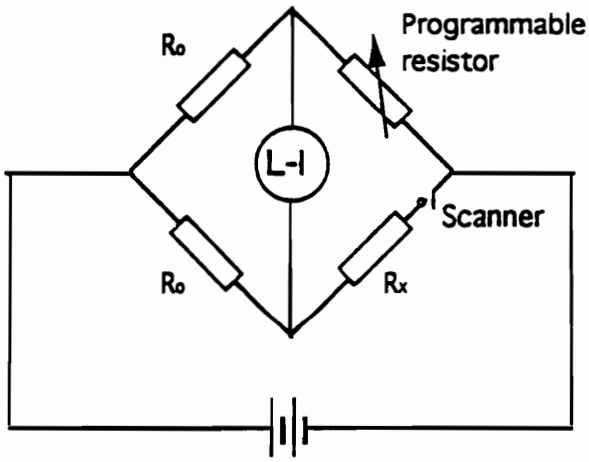

b. Bridge compensation method

Figure 4-5: Simplified diagrams for resistance measurement

The temperature mapping used for the triaxial cavity takes a much simpler approach. Figure 4-6 shows the simplified diagram for the two measurements performed in a regular data acquisition. It converts measurement of the sensor's resistance to measurement of the gain of an inverting amplifier.

R_A is a resistor which determines the gain of the inverting amplifier. By measuring the gain V_0/V_{in}, the compensation resistor R_c can be measured. The same is true for the mapping resistor R_m, which is measured in a separate scan. As far as the the temperature mapping, a 4 by 4 carbon resistor sensor array is mounted on the cavity top plate, while four compensation resistors are mounted on the side wall of the sensor chamber (not shown in Figure 4-2),. The compensation resistors change with bath temperature, compensating the bath temperature fluctuation during the data acquisition and enhancing the resolution of the measurement. A driving voltage, which is from the digital output of a NB-MIO-16 board in a Macintosh IIx personal computer and a customized scanning board, is applied to Row I, II, III, and IV in sequence, and the analog input of the NB-MIO-16 board reads the signals from four different columns which are amplified by the four inverting amplifiers. Including the reference row, the total number of wires used in the data acquisition system is 9. A 10-pin instrumentation feedthrough in a mini-conflat flange is enough for the signals of all twenty sensors. Figure 4-7 shows the overall structure of the data acquisition hardware.

4.3.2 Hardware for Data Acquisition

As shown in Figure 4-7, the system used for data acquisition consists of a Mac IIx, a NB-GPIB board with a Keithley 224 Programmable Current Source and a Keithley 196 System DMM, and a multifunction data acquisition board NB-MIO-16 with a customized scanning board. The measured objects are 20 carbon resistor sensors and a germanium resistor sensor used for calibration.

The Macintosh IIx is the system controller for the data acquisition process. It uses a MC68030 central processing unit (CPU) and a built-in MC68882 floating-point unit (FPU),

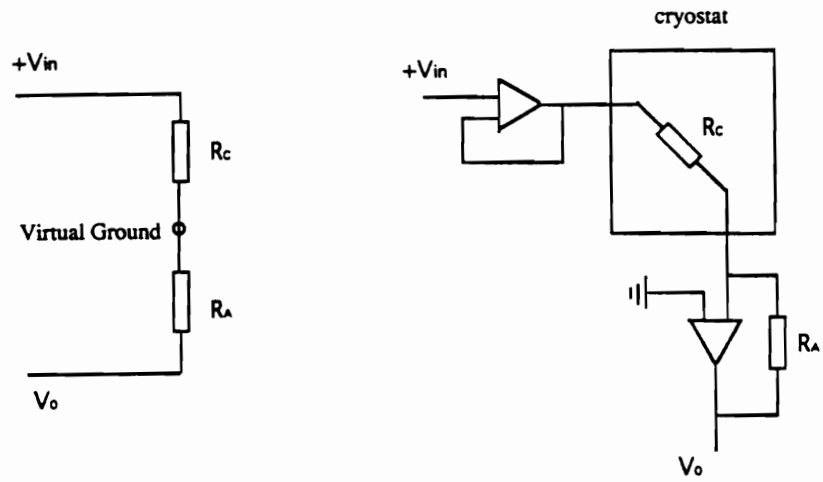

a. Compensation resistor measurement

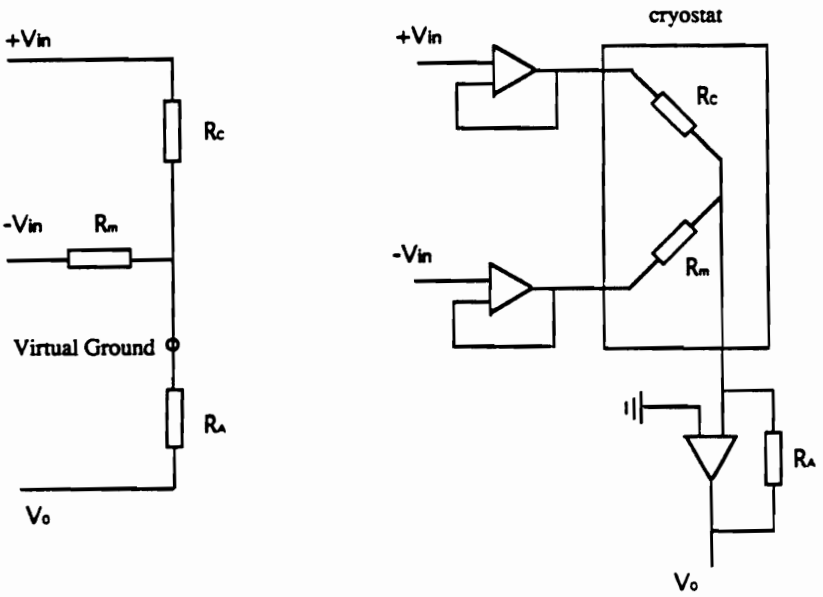

b. Sensor resistor measurement

Figure 4-6: Resistance measurement of the 16 mapping sensors

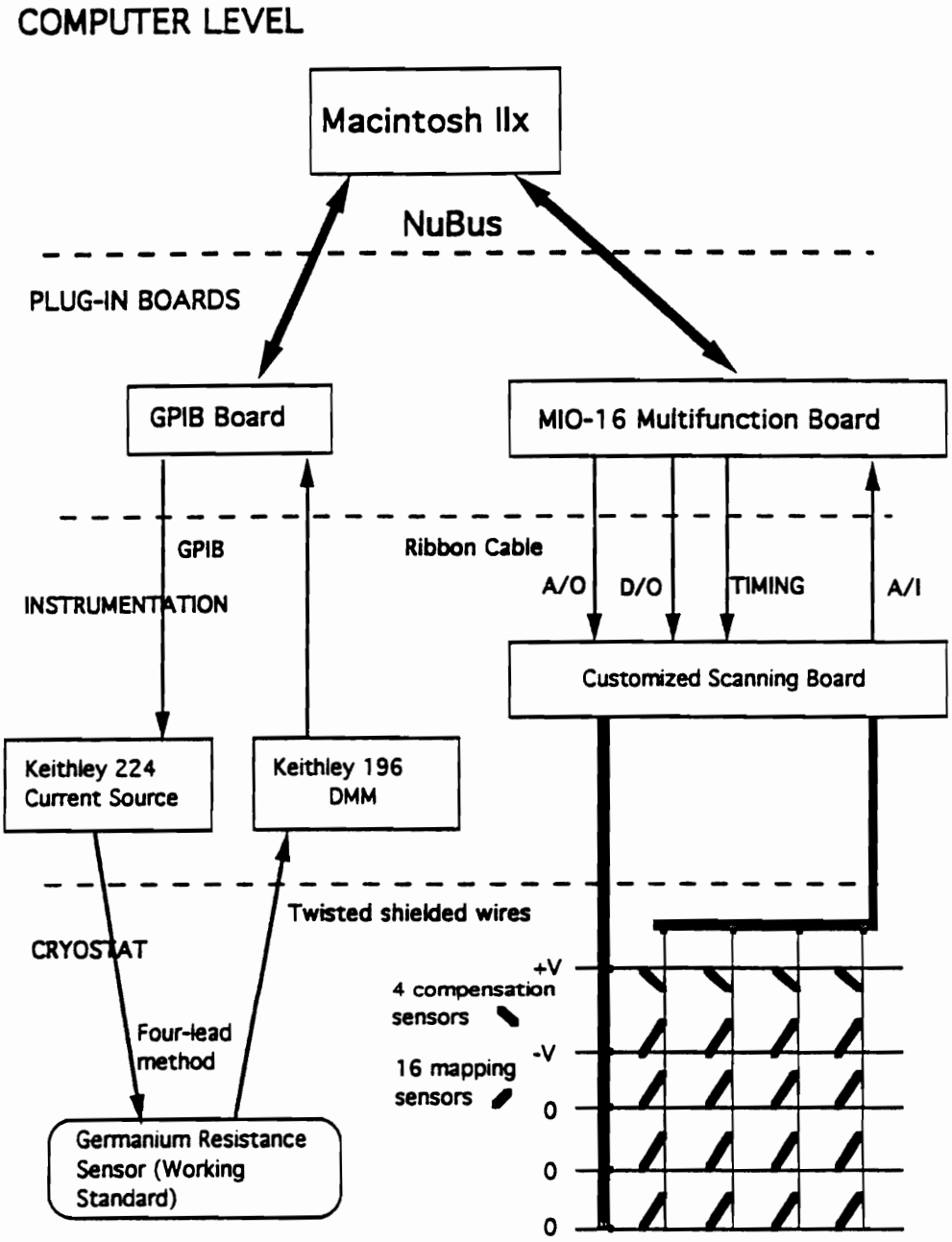

Figure 4-7: Instrumentation levels for temperature mapping

and its clock frequency is 15.6672 MHz. The IIx machine has a 32-bit address bus (Nu-Bus) and six NuBus expansion slots. NB-GPIB and NB-MIO-16 are two expansion boards used for scientific experiment and process control.

Equipped with a NB-GPIB board, a Macintosh NuBus computer such as the Mac IIx is a full function IEEE-4888 controller used for applications in laboratory testing, production testing, and process monitoring and control. The NB-GPIB board uses the NuBus (the computer internal 32-bit bus) to communicate with the Mac IIx and GPIB cables to communicate with GPIB-devices. It can control up to 14 GPIB-devices and its transfer rate is 800 kbytes/s. The following are some basic concepts concerning GPIB:

a. A GPIB cable is a General Purpose Interface Bus, which consists of 16 signal lines (8 data lines, 3 handshake lines, and 5 interface management lines) and 8 ground-return lines. It was first developed by Hewlett-Packard in 1965 and adopted as ANSI/IEEE Standard in 1987. It is commonly called the IEEE 488 interface bus, GPIB, or HP-IB. Data messages are transferred *in parallel* over 8 data lines in the bus. This allows faster information transfer than RS-232, which uses the serial port existing in any personal computer and transfers data messages in series over one data line.

b. A GPIB device is an instrument which includes a GPIB adapter board communicating with an IEEE 488 controller via a GPIB cable. It can be a Listener, a Talker, and/or a Controller. For example, in the four-lead resistance measurement, the Keithley 196 Current Source is a Listener, which receives the command (say, 1 μA current) from the computer, and the Keithley 196 DMM is a Talker when it transfers the measured voltage to the computer for presentation or storage. The GPIB Listener accepts ASCII strings as commands and executes them, while the GPIB Talker does the measurement, converts it to ASCII strings, and transfers the data message to the computer upon request.

The NB-MIO-16 is a multifunction analog, digital, and timing I/O board for the Macintosh NuBus. Unlike the NB-GPIB board which only takes care of the job of data transfer and

conversion, the NB-MIO-16 multifunction board measures real-time signals directly through its fast 12-bit analog-to-digital converter, which has 8 differential channels with a channel-independent programmable gain of 1, 10, 100, 500 (for NB-MIO-16H-25). The postfix "-25" indicates that the time of the analog-to-digital conversion is 25 μs, which corresponds to a normal sampling rate of 40 kHz. The MIO-16 can also be used as a variable voltage source with its two 12-bit digital-to-analog converters. For process control, its 8 TTL-compatible digital I/O lines (programmable to be input or output) can be used. For data acquisition control, it has three counter/timers and one frequency output as timing I/O, and has five data acquisition timing connections such as SCANCLK (SCANCLK generates a low-to-high edge whenever an A/D conversion begins, and will be used to increment the counter on the scanning board described below). These features make the MIO-16 board a fast, economical, and convenient choice for data acquisition and process control, and all these functions have been used when communicating with the customized scanning board, which will be described in the following.

4.3.3 Scanning Board

The two Keithley instruments in the INSTRUMENTATION layer of Figure 4-7 are ready-to-use commercial products. The following is a brief description of the function of the customized scanning board.

The building blocks of the scanning board are shown in Figure 4-8. Their functions are:

(1) Voltage divider: The range of the analog output of the MIO-16 board is -10 V to 10 V. The least significant bit refers to 10 V/2^{11} = 4.88 mV. To reduce the self-heating effect, a 1:100 voltage divider is used. The minimum driving voltage is 48.8 μV.

(2) Voltage inverter: This provides an on-board -V voltage source for the scanning. A multiplexer with +V/-V is controlled by Q3 of the counter, which means the source changes sign after every 8 counts, or 8 A/D conversions.

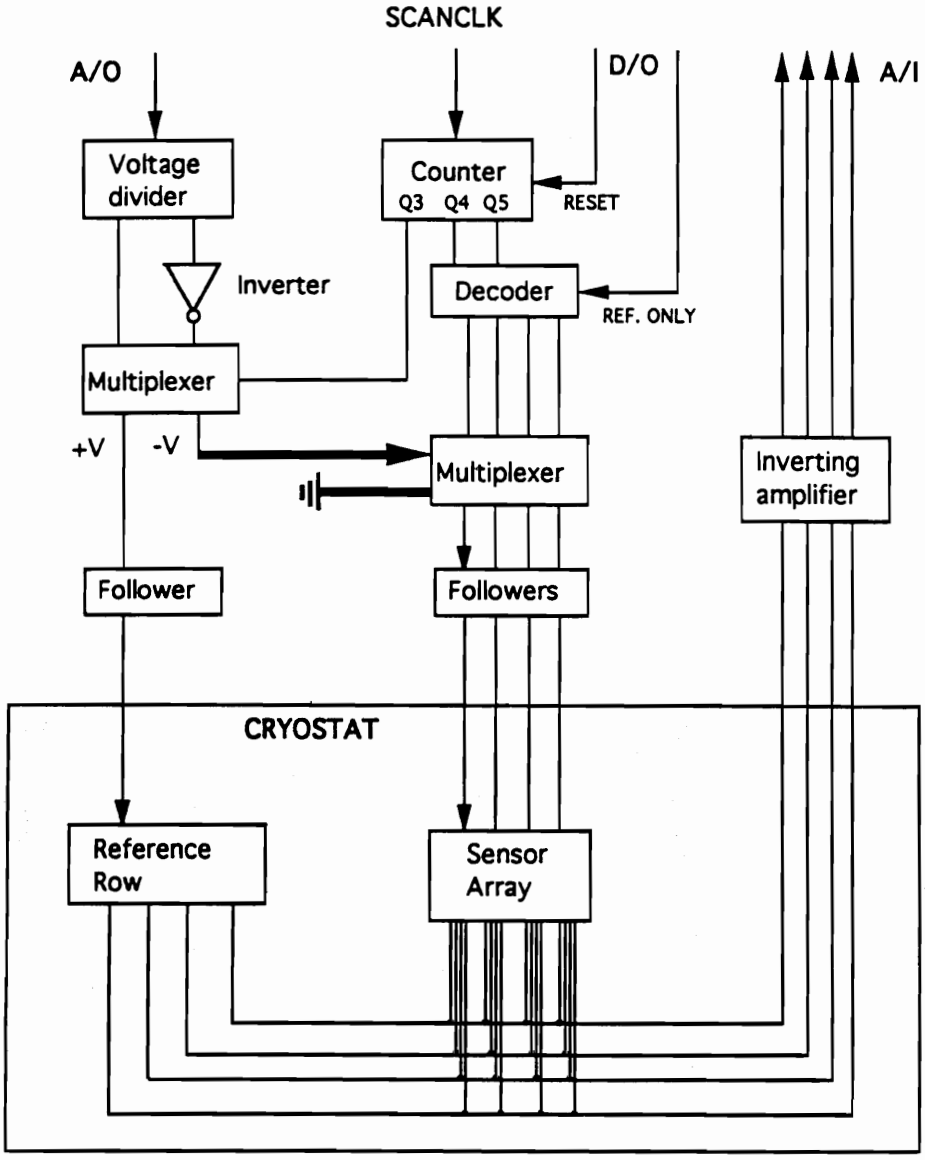

Figure 4-8: Diagram of the scanning board

(3) Counter: Before each data acquisition run, the counter is reset by a digital output. Then it starts to count for data acquisition, which is incremented by the SCANCLK pulse, or the A/D conversion. The Q4 (16 acquisitions) and Q5 (32 acquisitions) are sent to a decoder to control row scanning.

(4) Decoder: It decodes Q4 and Q5 from the counter for the four rows of the sensor array. The output always has one HIGH, and three LOW's, and it is used to select any one of the four rows of the sensor array through the multiplexer. The multiplexer's output is then (V, 0, 0, 0) for the first 8 counts. During this period, the MIO-16 scans channel 1 to 4 twice for Row 1. Then Q3 of the counter changes +V to -V through another multiplexer, and the MIO-16 starts to scan Row 1 for -V in another 8 counts. It then starts to scan the second row (0, V, 0, 0) and so forth. The total number of A/D conversions for a complete scan is 64. The scanning sequence of the sensors seen from the **A/I** is as follows:

$$\begin{pmatrix} V1 & V1 & -V1 & -V1 & V2 & V2 & -V2 & -V2 & \dots & V1 & V1 & \dots \\ V5 & V5 & -V5 & -V5 & V6 & V6 & -V6 & -V6 & \dots & V5 & V5 & \dots \\ V9 & V9 & -V9 & -V9 & V10 & V10 & -V10 & -V10 & \dots & V9 & V9 & \dots \\ V13 & V13 & -V13 & -V13 & V14 & V14 & -V14 & -V14 & \dots & V13 & V13 & \dots \end{pmatrix}$$

The sensors' labelling was shown in Figure 4-2.

(5) Another digital output line (REF. ONLY) is used to drive all the output of the decoder LOW. All the rows are at the virtual ground (0, 0, 0, 0), and the MIO-16 only measures the reference row R_{c_i}.

(6) Pre-amplifiers: There are four inverting amplifiers for four channels. The gain for each reference resistor is R_{A_i}/R_{c_i} (i = 1 to 4). R_{A_i} is 100 kΩ, and this gives a gain about 14 at 2 K and a gain of 800 at room temperature.

Figure 4-9 is the corresponding component schematic diagram for the scanning board. With the above description and component manufacturer's manuals, it should be easy to understand.

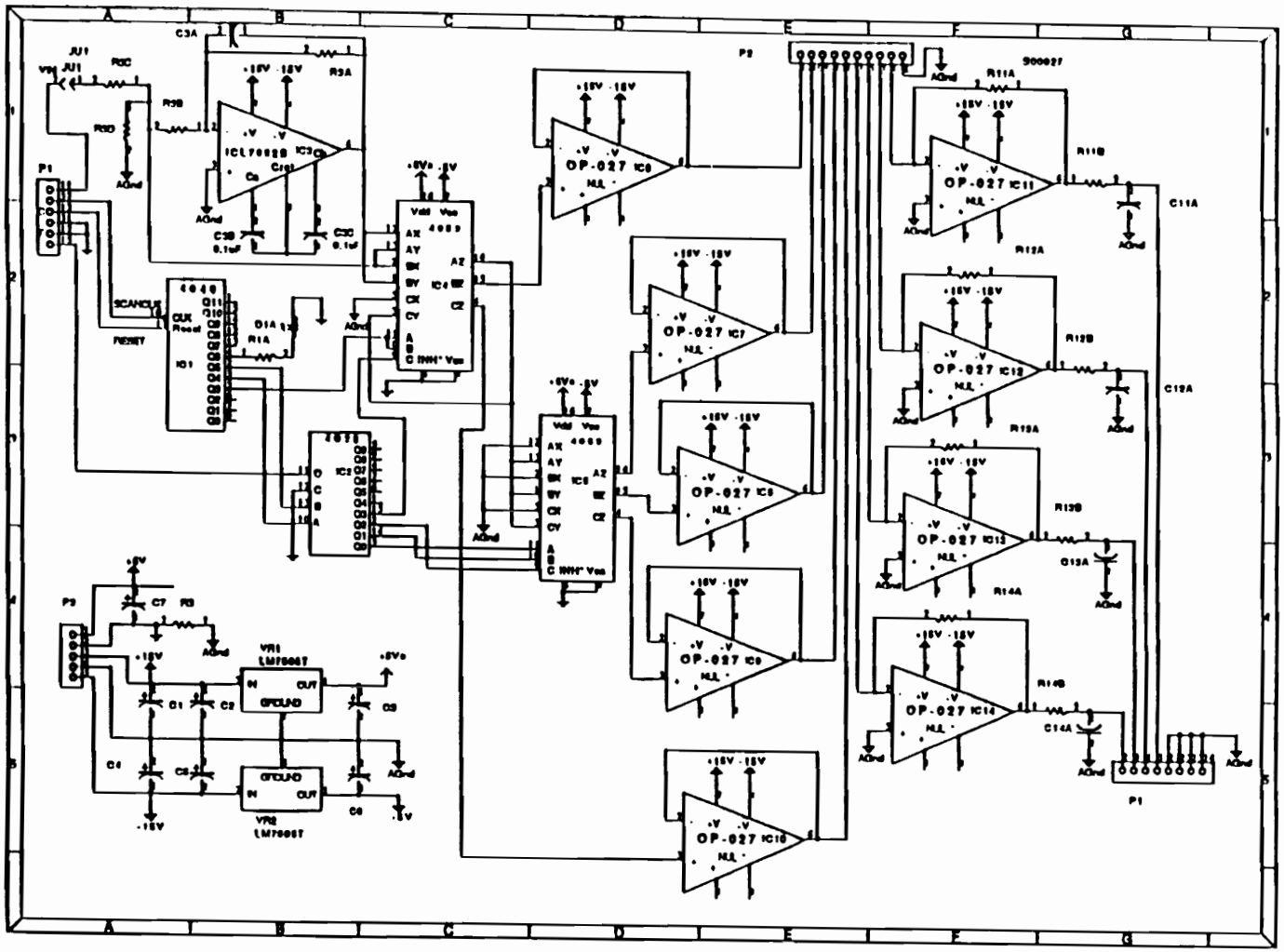

Figure 4-9: Component schematic diagram of the scanning board

4.3.4 Software for Data Acquisition

The software environment for the data acquisition includes System 7 for the Mac IIx and LabVIEW 2 for the GPIB and MIO-16 boards. To run these two programs, at least 6 MB of RAM are needed.

LabVIEW (Laboratory Virtual Instrument for Engineering Workbench) is a graphical programming software for data acquisition, data analysis, and data presentation. Because it is a high level language, users do not have to know the detailed protocols about how the acquisition is accomplished, but only need to know what is to be done. Taking a GPIB device as an example, there are two types of GPIB messages. One type is the interface messages. These are device independent and are transferred in the 3 Handshake Lines and 5 Interface Management Lines. The communication protocols are standardized in LabVIEW as different modules (icons, or subprograms) for programmers to use. The other type of massages is the device dependent, or data messages (ASCII strings), which can be found in the manual of a GPIB device and can be used to program a virtual instrument for the device.

A LabVIEW program includes a front panel for interfacing with users, a diagram for utilizing its functions, and an icon for interfacing between programs. The front panel can have as many *switches, knobs*, and *screen monitors* as the real panel of the instrument, which makes remote control as "real" as using the instrument. The diagram executes the messages from the front panel and other virtual instruments, and sends the results to the front panel as required. The icon serves as an interface with other virtual instruments in a larger scale application.

For the MIO-16 board, all of the programming information can be found in *LabVIEW 2 - LabDriver VI Library Reference Manual.* All of the control modules are explained in detail and are ready to be programmed. Figure 4-10 is an example of a LabVIEW front panel. Appendix C gives an example of a LabVIEW program, which executes the scanning for

data acquisition.

4.3.5 Determination of Important Acquisition Parameters

There are three error sources which affect resistance measurement: (1) thermal electromotive force, (2) electromagnetic interference, and (3) lead wire and contact resistance. As will be shown below, they are treated specially in the calorimetric measurement.

Thermal EMF

In the scanning sequence, alternation between $+V$ and $-V$ is used to cancel the thermal EMF effects. The inverter on the scanning board could be omitted because the polarity of the analog output could be switched in the control software. However, $-V$ on the scanning board is readily available, while $-V$ from the MIO-16 board requires a long settling time (as a Keithley scanner does), which would greatly reduce the scanning rate. It should be noted that $-V$ from the converter will not cancel the offset of the MIO-16 analog output, which is smaller than 1 LSB (least significant bit). The normal driving voltage before the divider was 150, or 0.732 V, so the error would be 0.6% for the resistance measurement. As will be described later, this will be calibrated with a room temperature resistance array. Therefore, an inverter is used for the sake of the sampling rate, and is preferred for noise reduction and minimization drift effects.

In addition, the reversal of the polarity also cancels the offset voltage/current of the operational amplifiers used in the circuit.

Noise in the Measurement

To reduce the noise pickup from the wires, care has been taken in arranging the wires and the instruments. A 3 m long 50-wire ribbon cable was used between the MIO-16 board and

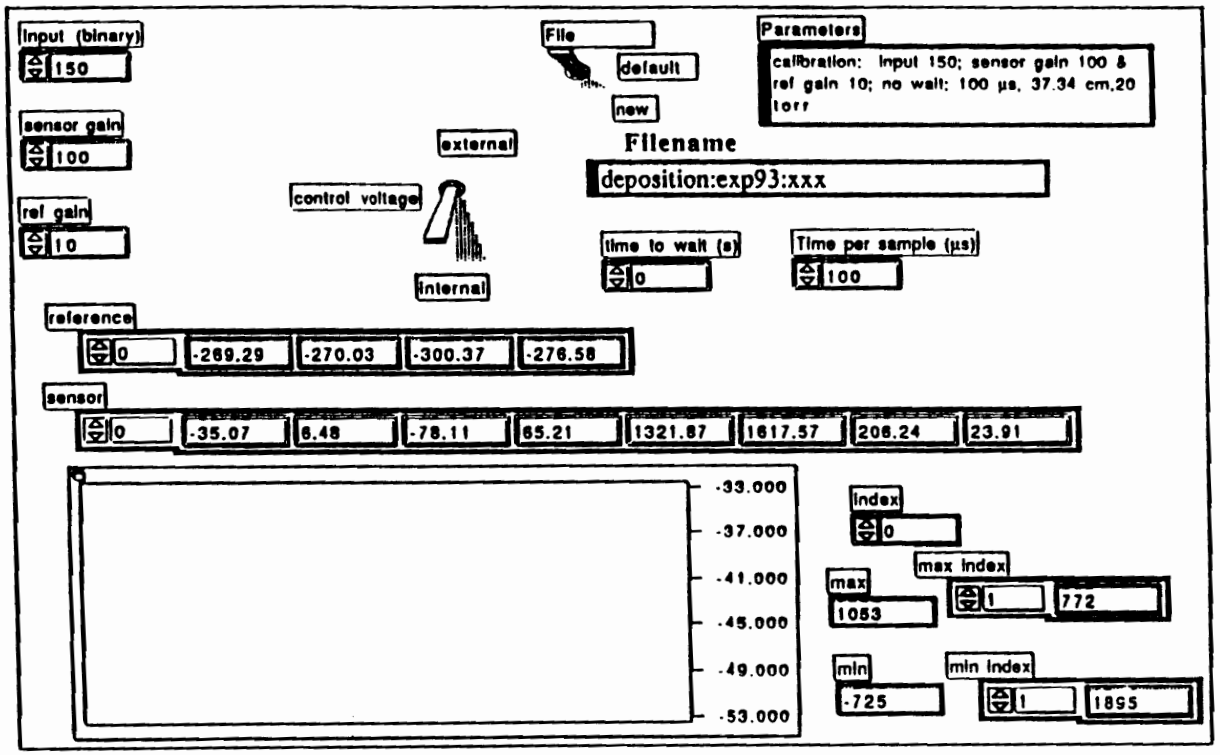

Figure 4-10: Front panel of a LabVIEW program

the scanning circuit. The scanning circuit was mounted in a aluminum box and connected to an instrumentation feedthrough on the cryostat plate with a 0.3 m long 10-wire cable which was well shielded. Inside the cryostat, the wires were shielded by the cryostat. The noise pickup from the ribbon cable could be as high as several millivolts. To enhance the signal-to-noise ratio (SNR), the driving voltage from the analog output of the MIO-16 should be as large as possible.

As mentioned in Section 4.2, the resistance of carbon resistor sensors at 2 K is about 7 kΩ. To get a 1 μA current, which corresponds to 7 nW of self heating power, the driving voltage after the divider (or at the follower) should be 7 mV. By using a 1 to 100 divider, the voltage from the MIO-16 should be 0.7 V. This is why 150 was used in the experiment (Figure 4-10). It is worth pointing out that scaling the binary output 150 to $150 \times 10V/2048 = 0.732$ V at the front panel would cause an extra error due to the round-off error. Therefore, the voltage output and input used below will be in binary with a unit of 4.88 mV.

A 1:1000 divider was also tried for large SNR, but it required high gain in the pre-amplifier. A high-gain amplifier not only had its own noise problem, but also increased the signal settling time. Therefore, a 1:100 divider, which matched the gain 100 of the MIO-16 signal amplifier, was finally adopted.

To achieve an effective SNR as high as 10^5, the noise picked up along the cable and the amplifier had to be averaged out. This was done by taking advantage of the high sampling rate of MIO-16 board. The highest sampling rate of a MIO-16H-25 board is 37 kHz, according to the manufacturer's manual. To get an error free acquisition, a 10 KHz sampling rate was used (*Time per sample* 100 μs in Figure 4-10). Because there were 16 sensors and each sensor was measured twice for $\pm V$, the sampling rate for each sensor was actually 156 Hz. Therefore, 100 valid readings for each sensor were acquired in only 0.64 s. Normally, 512 valid readings were done for each point from each sensor, which only took 3.3 s.

To reduce low frequency noise such as bath drifting, RF power was applied in the pulse mode. During each cycle, 4 or 8 points were collected. 10 to 128 cycles were collected for an

experiment, depending on the experimental conditions. Normally it took 10 to 20 minutes for an RF heating measurement. For the heater calibration measurement, it took one to six hours to conduct one experiment. A 128 cycle, 4-point per cycle acquisition gave an average of $2^{18} \simeq 260$ k readings, and the noise reduction ratio was 1/512.

To reduce high frequency noise, an RC filter (1 kΩ, 0.033 μF) was added to each pre-amplifier. The frequency is $f = 1/2\pi RC = 4.8$ kHz, since $\tau = RC = 33\,\mu$s. To get a 10^{-5} accuracy, $t = 11.5\,\tau = 380\,\mu$s is needed. This was why the first four readings of each row were discarded, which gave 400 μs for the signal to reach equilibrium.

Lead Wire Resistance

At 2 K, the resistance of lead wires and contacts is smaller than 30 Ω, and the sensor resistance is about 7 kΩ. The absolute error in the sensor resistance measurement is smaller than 0.5%. Because of cancellation in the temperature change, the error caused by lead wire resistance is at least one order of magnitude smaller than 0.5%. This is the basic reason why the two-wire configuration was used.

4.3.6 Resistance Measurement and Its Resolution

Figure 4-8 showed the simplified diagram of the resistance measurement. There are two sets of resistors: 16 mapping resistors which are mounted on the top plate of the cavity, and 4 compensation resistors which are mounted on the inner wall of the sensor chamber, away from any source of RF heating. The compensation resistors are determined by

$$R_c = -\frac{A_c}{G_c} = -\frac{R_A\,\alpha_c\,\gamma}{G_c} \tag{4.4}$$

where G_c is the measured gain, $R_A = 100$ kΩ is the gain resistor, $\alpha_c = 10$ is the computer amplifier gain, and $\gamma = 0.01$ is the voltage divider ratio, yielding an A_c of 10 kΩ. For an R_c of 7 kΩ at 2 K, a gain of 1.4 is expected.

The resistance of the mapping resistor is given by

$$G_m = A_m \left(\frac{1}{R_m} - \frac{1}{R_c} \right) \tag{4.5}$$

$$R_m = \frac{1}{1/R_c + G_m/A_m} = \frac{1}{1/R_c + G_m/R_A\,\alpha_m\,\gamma} \tag{4.6}$$

where G_m is the measured gain for the mapping sensor, and $\alpha_m = 100$ is normally used for the computer amplifier gain, yielding an A_m of 100 kΩ. If $R_c \simeq 0.9\,R_m$ is chosen, G_A would be approximately equal to G_m.

The compensation resistors were used for three purposes:

(1) To increase the dynamic range of the measurement: If $\alpha_m = \alpha_c = 10$, then G_A would be about 0.14. For an 1 V A/O voltage V_{IN}, the A/I voltage V_0 would be 1.4 V for R_c and 0.14 V for R_m. Therefore, the dynamic range which could be used for mapping sensors is 9.86 V instead of 8.6 V.

(2) To achieve a constant gain against slow drifting or bath temperature fluctuation: From eq. (4.5), it can be seen that any small resistance change due to slow drifitng or bath temperature fluctuation will not have much effect on the gain, since both R_m and R_c have similar temperature characteristics.

(3) To enhance the sensitivity of the measurement system: For the compensation resistors, the resolution is:

$$\frac{\Delta R_c}{R_c} = \frac{\Delta G_c}{G_c} = \frac{\Delta V_c}{V_c} \tag{4.7}$$

For the mapping sensors, R_c is unchanged during the RF heating, therefore

$$\frac{\Delta R_m}{R_m} = \frac{R_m\,\Delta G_m}{A_m} = \frac{R_m\,G_m}{A_m}\frac{\Delta G_m}{G_m} = \frac{R_m - R_c}{R_m}\frac{\Delta V_m}{V_m} \tag{4.8}$$

For $R_c \simeq 0.9\,R_m$, the resolution is one order of magnitude higher than that of eq. (4.7).

The MIO-16 board has a resolution of 1 LSB, or a relative resolution of $1/2^{11} = 4.88 \times 10^{-4}$. The resolution can easily be pushed to 10^{-4} by averaging (0.2 LSB). With a compensation

row in the sensor array, the relative resolution can then be achieved at the 10^{-5} level. According to eq. (4.2), the temperature resolution could be 6.7 μK at 2 K given a specific sensitivity of 3 for the carbon resistors.

4.3.7 Experimental Results

Choice of Operational Amplifier

At first, all the op-amps used were OP-27E (Figure 4-9). The OP-27E is an ultra-low noise, high precision bipolar operational amplifier. Its input offset voltage is 25 μV maximum, input offset current is 50 nA maximum, and input bias current is 60 nA maximum. These offsets caused a problem when a low driving voltage was used to reduce the self-heating effect of the sensor.

A 2.8 kΩ test array was used to check the self-heating effect. It was found that the measurement results were affected by those offset parameters of the OP-27E at the low driving voltage. Table 4-1 shows such an effect. When the voltage after dividing was 7 mV, the resistance measurement had an error of 3.5% due to the offset parameters. To solve this problem, super chopper-stabilized low-noise operational amplifiers (ICL7652S) were tried. The ICL7652S has an offset voltage 7 μV between 0 ^{o}C and 70 ^{o}C, an offset current of 40 pA, and a bias current of 30 pA. These parameters are much better than those of OP-27, but the use of ICL7652S is limited by the slow response due to the two large capacitors (0.1 μF) required by the ICL7652S. The final solution was to use an ICL7652S for the inverter and leave all other drivers and amplifiers with OP27E. As shown in Table 4-1, the effect of the amplifier's offsets was reduced by 10 times, which is acceptable because it will be cancelled in the resistance change or the temperature change. OP-27E op-amps in the followers and pre-amplifiers were left because they are after the inverter. The offset voltage/current will be cancelled out in the $\pm V$ subtraction. For the inverter there is no limit in the relaxation

time, because $\pm V$ is readily available on the scanning board and is not changed during each run.

Electromagnetic Noise at Room Temperature

To check the noise environment of the measurement system, a room temperature scanning of the sensor array was conducted. At room temperature, the carbon sensors have the smallest temperature variation, and they are nearly temperature independent. Therefore, any variation in reading could be viewed as the noise from the cable pickup and the amplifiers.

Table 4-2 shows the results from a 90-point room temperature acquisition. The 90 points were divided into 9 groups, each containing 10 points.

The average of 10 points (referred to as 10 cycles in future experiments) is treated as an independent experiment run. As can be seen, the relative error for 10 points is smaller than 2.9×10^{-5} (maximum among 20 sensors), which includes the contribution from the EM noise, noise from the amplifier, and a little fluctuation of resistor sensors.

The maximum σ_R/R is R_{m4}, which has a relative uncertainty of 2.9×10^{-5} for a 10-point result. This SNR is equivalent to 0.06 LSB resolution. Assuming the noise is reduced by $\sqrt{N}$, a 90-point acquisition has a SNR of 10^{-5}, or 0.02 LSB. If four points are acquired during each cycle, a 23-cycle measurement will achieve such a low SNR. Taking 15 s as the thermal time constant between ON/OFF levels, the time consumed for such a measurement is 23 minutes.

It has to be pointed out that the above discussion is only for the room temperature electromagnetic interference. At 2 K, the bath fluctuation will be the dominant noise source. If the bath were stable, the measurement system would have a resolution of less than 1 μK.

Table 4-1: OP27E *vs.* ICL7652S (2.8 kΩ array)

Voltage (mV) (after the divider)	OP27E Resistance (Ω)	ICL7652S Resistance (Ω)
78.1	2817	2801
32.2	2839	
7.81	2912	2810

Table 4-2: Results of room temperature measurement

Group	R_{C1}	R_{B1}	R_{B2}	R_{B3}	R_{B4}
1st $\bar{R}_{10}$ (Ω)	133.575	130.954	133.173	147.013	141.617
2nd $\bar{R}_{10}$ (Ω)	133.575	130.953	133.173	147.012	141.619
3rd $\bar{R}_{10}$ (Ω)	133.583	130.964	133.184	147.024	141.626
4th $\bar{R}_{10}$ (Ω)	133.577	130.959	133.179	147.019	141.616
5th $\bar{R}_{10}$ (Ω)	133.579	130.960	133.181	147.021	141.619
6th $\bar{R}_{10}$ (Ω)	133.572	130.956	133.176	147.015	141.612
7th $\bar{R}_{10}$ (Ω)	133.574	130.958	133.178	147.017	141.614
8th $\bar{R}_{10}$ (Ω)	133.573	130.958	133.177	147.016	141.614
9th $\bar{R}_{10}$ (Ω)	133.575	130.959	133.180	147.017	141.614
90-point $\bar{R}$ (Ω)	133.576	130.958	133.178	147.017	141.617
90-point σ_R	0.0036	0.0032	0.0035	0.0038	0.0042
$\sigma_R/\bar{R} \times 10^5$	2.7	2.4	2.6	2.6	2.9

4.4 Calibration

4.4.1 Procedure

Calibration of all 20 carbon resistor sensors is normally done before or after each RF and calorimetric measurement. This is a necessary procedure because the sensor's resistance supposedly drifts day by day, and is different run by run.

For normal calorimetric measurements, the calibration range was between 20 Torr and 30 Torr, which corresponds to 1.96 K and 2.10 K (temperature read by the germanium sensor). Eleven data points were measured for calibration at regulated pressures. The regulation was done by a stepping motor controlled VAT valve. At each pressure, 10 consecutive points were acquired for averaging. Therefore, there were 5120 readings for each sensor at each temperature point.

For thermal conduction calibration of the top plate, calibration was done between 20 Torr and 800 Torr. Eleven data points were obtained at different pressures, but the pressure above 100 Torr was controlled by a slow pumping speed offset by a manually controlled heater. The pressure fluctuation controlled this way was ± 5 Torr, which translates to ± 10 mK at 500 Torr.

4.4.2 Temperature Conversion

One direct temperature conversion method is to scan the sensors at different temperatures, save them, and then look up the calibration table to linearly interpolate over small intervals. Because the $(n+1)th$ order derivative is always larger than the nth order derivative, the interval has to be small for a specified accuracy. This requires more calibration points and more time for creating and checking a look-up table. Moreover, the error transferred from the calibration point is inversely proportional to the interval.

A logarithmic relation has been used for the conversion in all the experiments conducted for this thesis. It is expressed as:

$$\frac{1}{T} = a_0 + a_1 \left(log\, R + \frac{1}{log\, R} \right) \tag{4.9}$$

The 10 points acquired at each pressure were averaged to get an R value and used for a 11-point line fitting to determine a_0 and a_1. Figure 4-11 is an example of the fitting curve. The smallest deviation was 3 μK and the largest deviation was 490 μK for the fit.

Table 4-3 shows coefficients obtained in the same cooldown and in different cooldowns. As can be seen, the coefficients are almost the same in each cool down but may change significantly in different runs. The two calibrations on 8/26 and 8/31 did not experience any warmup, and the reproducibility was excellent, while the other two calibrations were conducted in two separate cooldowns after exposure to atmosphere. Systematic change of a_0 and a_1 was observed and is shown in Figure 4-12.

4.4.3 Error Analysis

The accuracy $\delta(\Delta T)/\Delta T$ of the calorimetric measurement is heavily dependent on the calibration. To discuss error terms, eq. (4.9) can be written as:

$$\Delta T \simeq a_1 T^2 (1 - \frac{1}{log^2 R}) \frac{\Delta R}{R} \tag{4.10}$$

where a_1 is the calibrated coefficient, T is the working temperature, $\Delta R/R$ is the relative change due to RF heating, and $(1 - 1/log^2 R)$ is a nearly constant term. The error is then determined by

$$\frac{\delta(\Delta T)}{\Delta T} = \frac{\delta a_1}{a_1} + 2\frac{\delta T}{T} + \frac{\delta(\Delta R)}{\Delta R} + \frac{\delta R}{R} \tag{4.11}$$

where $\delta a_1/a_1$ is smaller than 0.5% (Table 4-3), both $\delta T/T$ and $\delta R/R$ are smaller than 0.1%, and $\delta(\Delta R)/\Delta R$ is smaller than 0.5% when ΔT is about 10 mK. Notice all the $\delta(\ldots)$'s are from the randomly distributed measurement errors.

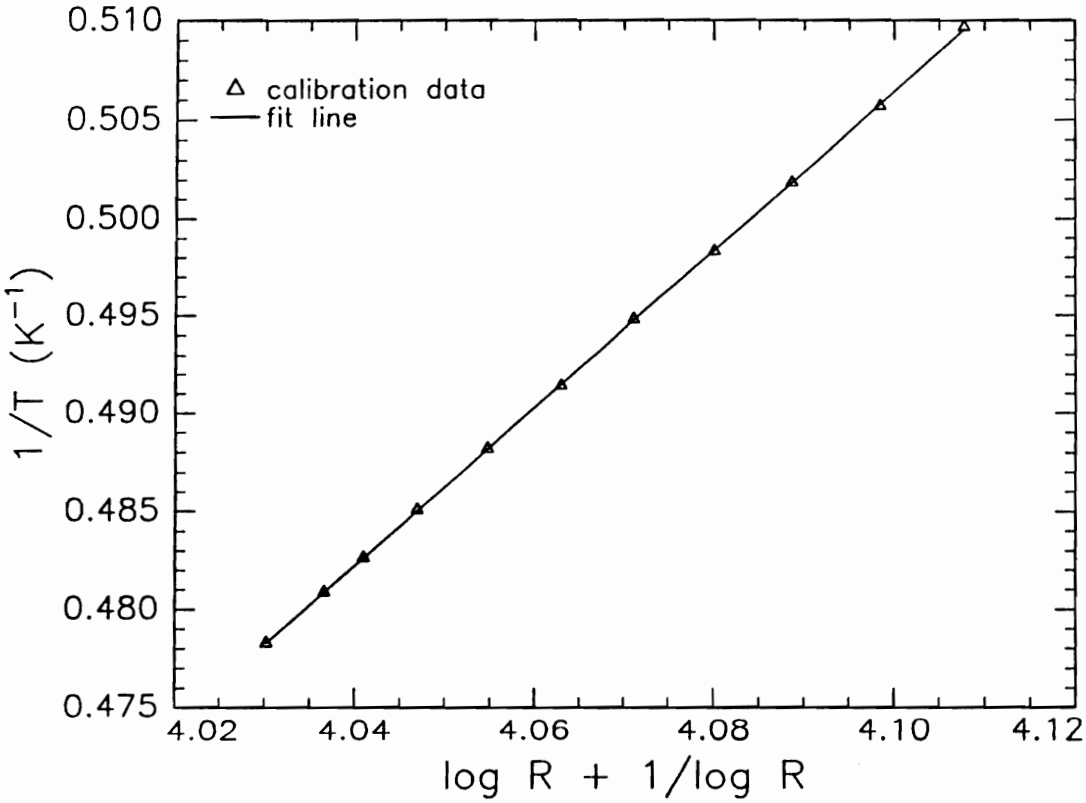

Figure 4-11: Calibration $1/T = a_0 + a_1 (log\, R + 1/log\, R)$

Table 4-3: Calibration Coefficients at different runs

Sensor #	8/26/92		8/31/92		10/26/92		11/18/92	
	a_0	a_1	a_0	a_1	a_0	a_1	a_0	a_1
1	-1.205	0.4184	-1.206	0.4187	-1.126	0.3981	-1.066	0.3829
2	-1.237	0.4280	-1.239	0.4283	-1.160	0.4090	-1.123	0.3994
3	-1.268	0.4321	-1.270	0.4324	-1.188	0.4134	-1.160	0.4063
4	-1.261	0.4333	-1.262	0.4336	-1.185	0.4147	-1.133	0.4013
5	-1.253	0.4308	-1.242	0.4283	-1.165	0.4089	-1.114	0.3959
6	-1.280	0.4426	-1.271	0.4403	-1.196	0.4211	-1.131	0.4044
7	-1.303	0.4452	-1.293	0.4426	-1.222	0.4247	-1.162	0.4098
8	-1.240	0.4263	-1.231	0.4240	-1.166	0.4079	-1.095	0.3903
9	-1.258	0.4334	-1.263	0.4344	-1.166	0.4102	-1.143	0.4040
10	-1.244	0.4278	-1.250	0.4292	-1.155	0.4057	-1.133	0.4001
11	-1.267	0.4383	-1.272	0.4396	-1.200	0.4204	-1.125	0.4011
12	-1.187	0.4109	-1.192	0.4122	-1.124	0.3948	-1.059	0.3783
13	-1.286	0.4387	-1.284	0.4379	-1.205	0.4177	-1.132	0.3991
14	-1.276	0.4379	-1.273	0.4373	-1.194	0.4171	-1.127	0.3996
15	-1.294	0.4363	-1.290	0.4353	-1.202	0.4131	-1.145	0.3990
16	-1.275	0.4359	-1.273	0.4351	-1.195	0.4156	-1.135	0.4002

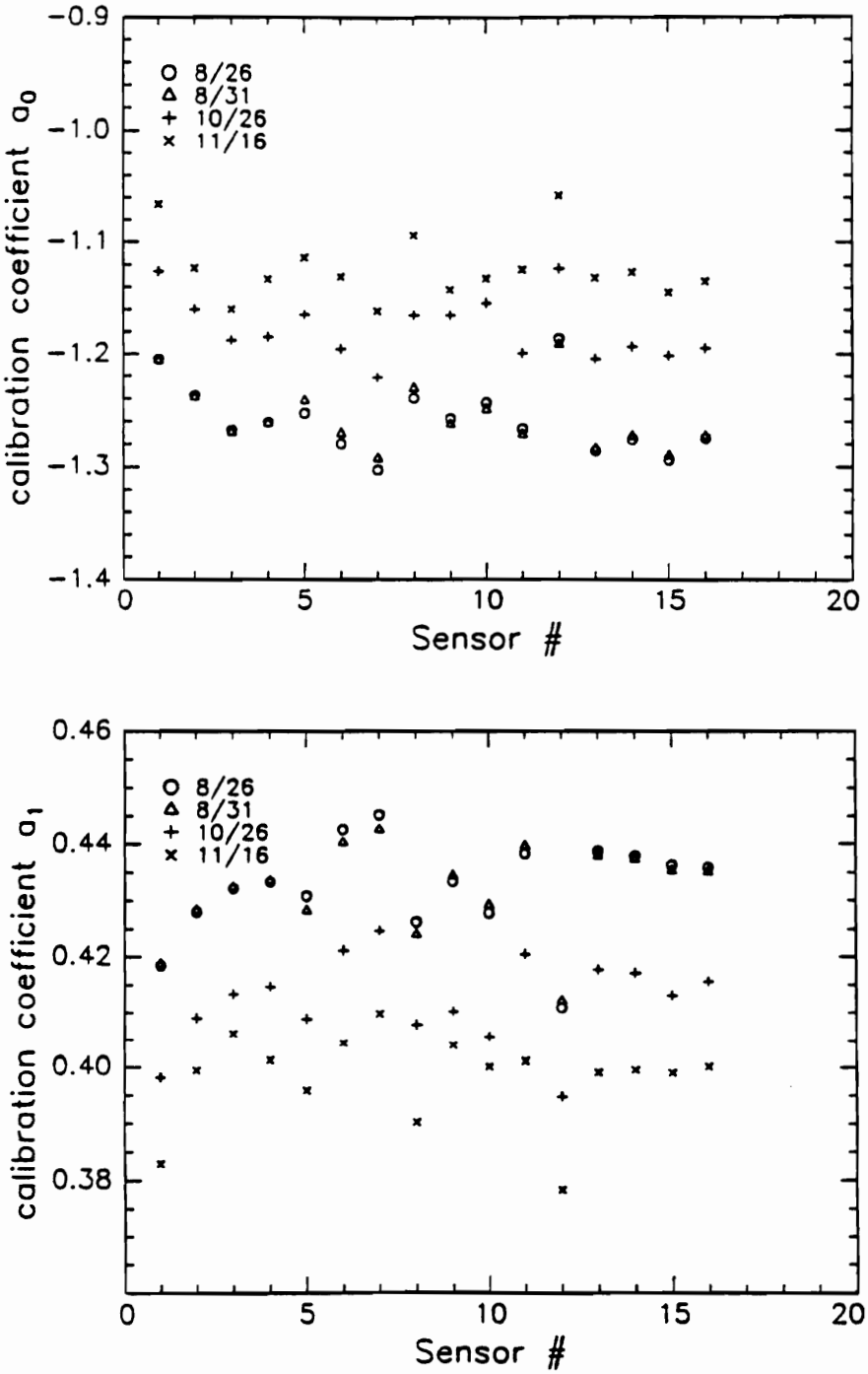

Figure 4-12: Calibration coefficient change with time

As mentioned earlier, the lead wire has a resistance of less than 30 Ω. This is a 0.5% systematic error in temperature conversion. Using δT_0 to denote the error caused by the lead wire δR_0 during the conversion, it will be subtracted out from eq. (4.10) because $\Delta(\delta R_0) \simeq 0$.

In addition, there are several ways to calculate ΔT. If there is only bath temperature fluctuation but no bath temperature drifting, the simplest way is to average the gain for the bath level and the heating level, convert the two points to resistance, then to temperature. The second way is to calculate the average resistance for each cycle, then convert the resistance to temperature, get the temperature difference, and average them for the number of cycles. This takes advantage of using the pulse mode against bath drifting. The third method is to convert the resistance to temperature for each point, get the cycle average and the cycle difference, and then average the cycle difference. The third way is used because it was believed it would average the effect of δa_1 in eq. (4.11).

4.5 Results of the Calorimetric Measurements

4.5.1 Heater Calibration

A calibration heater was used to check the validity of the measurement method, to measure the thermal conduction product κh, and to test the detection limit. The experimental results are presented as follows.

Calibration Heater

The calibration heater was made with 42 gauge constantan wire. The wire was wound on a 1.27 cm I.D., 1.46 cm O.D. niobium tube. To reduce the residual heating caused by the lead wire resistance, the lead wire used for the heater was 50 cm long, 36 gauge copper wire.

Heat flow through the lead wire and the niobium plate had a ratio smaller than 3×10^{-4}. The resistance of the heater was very stable during each measurement. Table 4-4 shows the measured heating power. As can be seen, the resistance of the heater increases a little due to its temperature rise at high heating currents. The accuracy of the power measurement can also be seen from the consistent resistance values.

The heater was glued to the cavity top plate with GE varnish 7031. It was placed in the center on the cavity side. Beyond the outer diameter of the heater, the temperature distribution is:

$$T(r) = T_0 + \frac{P}{2\pi\kappa h} ln \frac{r_0}{r} \tag{4.12}$$

where P is the heating power of the heater. With measured ΔT, the thermal conduction product κh of the plate could be calculated.

Two sets of experiments were conducted. One measured the sensors' response to different power levels at 20 Torr. The other measured the sensors' response at different bath temperatures for a given power.

Sensors' Response to the Heating Power

To measure the thermal conductivity of the cavity top plate, the calibration heater was placed on the center of the niobium top plate. Current pulses were applied to the heater in the experiment. There were 128 cycles in each experimental run. During each cycle, eight points were obtained at each level, and 512 readings were averaged for each point. Figure 4-13 shows the response of sensor 5 and sensor 8 after averaging over 8 points in each level. The standard deviation was only 24 μK (The actual bath temperature fluctuation is smaller than 2 mK, divided by $\sqrt{8 \times 512}$ yields 31 μK – good agreement). For sensor 8, its ΔT was 2.47 mK, which yielded a 1% of error for each cycle. This accuracy was achieved within 100 s. In addition, the bath temperature measured by the two sensors has

Table 4-4: Parameters of the calibration heater

Heating Current (mA)	Power (μW)	Resistance (Ω)
0.50	11.1	44.45
1.00	44.5	44.45
1.75	136.2	44.46
2.50	278.0	44.47
5.00	1112.6	44.50
9.00	3609.2	44.56

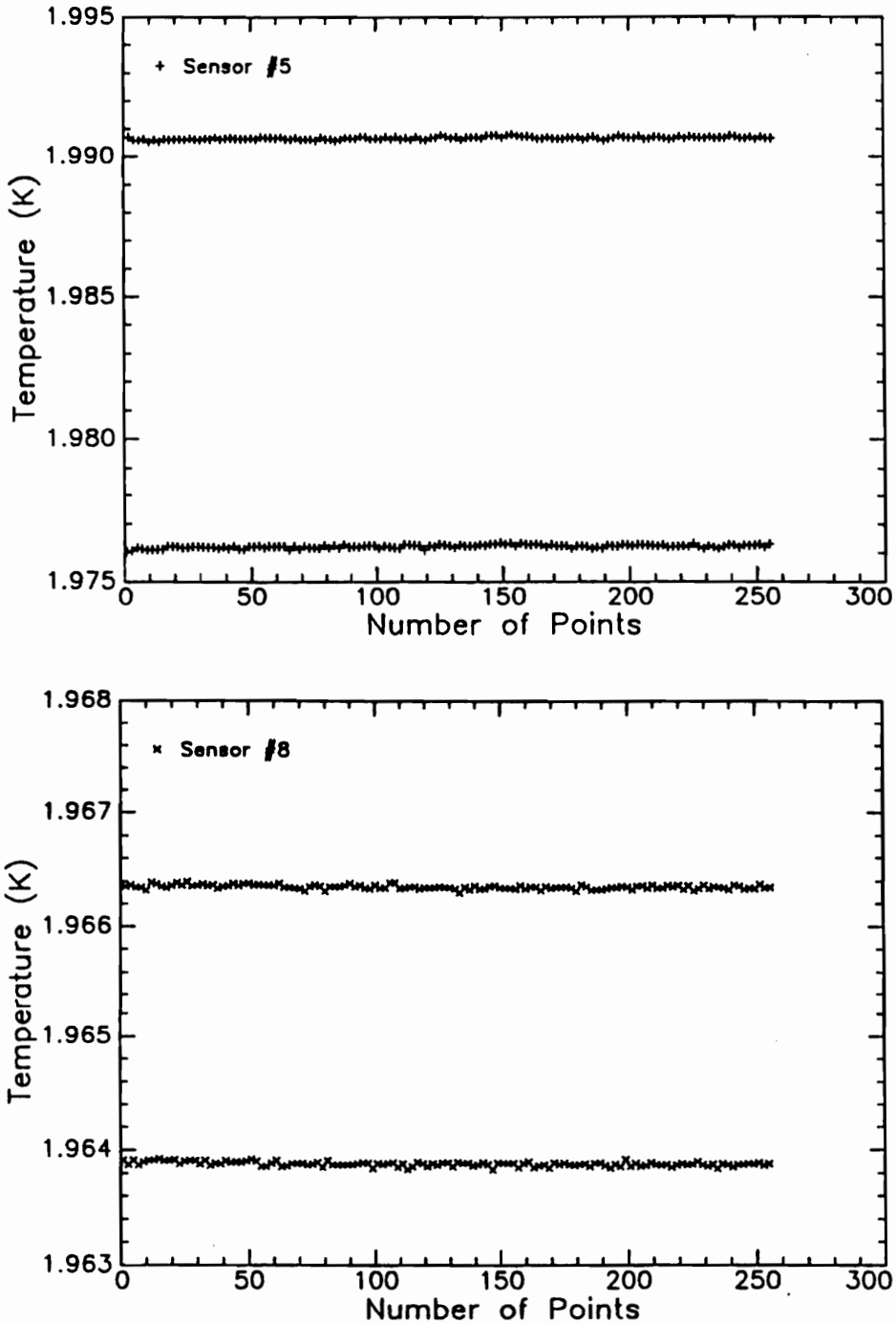

Figure 4-13: Temperature change measured by sensor 5 & 8

a difference of 12 mK, but it did not affect the temperature difference in the calorimetric measurement, as will be seen in the next two tables.

Table 4-5 shows the results obtained at different power levels. In the table, the column corresponds to the response of 16 mapping sensors to a given power, while the row corresponds to each sensor's response to different power levels. Except sensor 3 which had a loose contact with the niobium plate, all other sensors had responses consistent with their positions.

Table 4-6 normalizes the results to the power level of 278.0 μW. As can be seen, all normalized coefficients are about 1 with few exceptions. This verifies the proportional relation between the temperature change and the applied power level. In the intermediate power range (100 μW to 1000 μW), the error of all the sensors is within 1%, which agrees with the error analysis in Section 4.4.3. For sensor 16 at 136.2 μW, 1% means a result of $300 \pm 3\,\mu$K ($31/\sqrt{128} = 2.8\,\mu$K – the bath fluctuation does obey random distribution in normal cases!). For larger power, deviation amounts of 5% appear in large temperature changes. This small deviation was from the longer relaxation time at a higher power due to the increased ratio of heat capacity to thermal conductivity. Sensors located in last ring (4, 8, 12, 16) had the smallest deviation. On the other hand, deviation for a weak signal, such as sensor 16 at 11.1 μW, amounts to 50%. This is understandable and it can be neglected in analysis.

In a word, the normalization table has shown the accuracy and the reliability of the calorimetric method, including the sensor, the measurement system, and the signal-temperature conversion.

Detection Limit

As for the detection limit, temperature changes at a power level of 0.5 μW were measured. Table 4-7 shows the measurement results $\Delta T_{\pm\Delta T}$ and fluctuations (ΔT_{max} and ΔT_{min}) sensed by sensors in column IV (13 to 16; the other three columns were about the same).

Table 4-5: Temperature mapping at different power levels

Power (μW)	11.1	44.5	136.2	278.0	1112.6	3609.2
ΔT_1 (mK)	0.53	2.13	6.45	13.14	51.96	162.13
ΔT_2 (mK)	0.30	1.25	3.80	7.73	30.74	97.66
ΔT_3 (mK)	0.11	0.39	1.14	2.30	9.26	30.26
ΔT_4 (mK)	0.10	0.39	1.17	2.38	9.53	30.89
ΔT_5 (mK)	0.62	2.54	7.75	15.73	61.81	192.01
ΔT_6 (mK)	0.34	1.38	4.18	8.48	33.58	105.93
ΔT_7 (mK)	0.24	0.96	2.92	5.93	23.55	74.94
ΔT_8 (mK)	0.11	0.44	1.33	2.72	10.82	34.77
ΔT_9 (mK)	0.56	2.34	7.09	14.41	56.70	176.57
ΔT_{10} (mK)	0.31	1.25	3.78	7.68	30.42	96.65
ΔT_{11} (mK)	0.16	0.63	1.91	3.90	15.51	49.60
ΔT_{12} (mK)	0.10	0.35	1.03	2.09	8.35	26.07
ΔT_{13} (mK)	0.49	2.00	6.11	12.37	48.77	152.46
ΔT_{14} (mK)	0.33	1.32	4.04	8.20	32.41	102.57
ΔT_{15} (mK)	0.17	0.65	1.96	3.99	15.91	51.03
ΔT_{16} (mK)	0.04	0.10	0.30	0.60	2.39	7.75

Table 4-6: Normalized temperature mapping

Power (μW)	11.1	44.5	136.2	278.0	1112.6	3609.2
Sensor 1	1.012	1.012	1.002	1.000	0.988	0.950
Sensor 2	0.978	1.012	1.004	1.000	0.994	0.973
Sensor 3	1.219	1.053	1.011	1.000	1.008	1.015
Sensor 4	1.091	1.031	1.007	1.000	1.002	1.001
Sensor 5	0.985	1.010	1.005	1.000	0.982	0.940
Sensor 6	1.010	1.015	1.006	1.000	0.989	0.962
Sensor 7	1.006	1.008	1.005	1.000	0.992	0.973
Sensor 8	0.983	1.012	1.000	1.000	0.995	0.986
Sensor 9	0.978	1.013	1.005	1.000	0.983	0.944
Sensor 10	1.012	1.015	1.004	1.000	0.990	0.970
Sensor 11	1.006	1.008	1.003	1.000	0.995	0.981
Sensor 12	1.144	1.032	1.003	1.000	0.997	0.959
Sensor 13	0.999	1.008	1.008	1.000	0.985	0.949
Sensor 14	1.013	1.009	1.006	1.000	0.989	0.964
Sensor 15	1.039	1.020	1.004	1.000	0.997	0.986
Sensor 16	1.499	1.084	1.009	1.000	0.997	0.998

The difference in the bath stability between the two runs was caused by pumping activity in other cryostats connected to the same vacuum pump. The control parameters were actually the same for both runs. The following results can be obtained from the table:

(1) The error range shown in the table was the error for each cycle, which was determined by the averaged bath temperature fluctuation (22 μK in the normal case). This is usually smaller than the conservative estimation above (the error from a 2 mK range bath temperature fluctuation is 31 μK).

(2) The bath condition was clearly shown by ΔT_{max} and ΔT_{min}. The first run was performed in a disturbed bath, while the second run was done in a normal bath (about 2 mK fluctuation). The effect of a disturbed bath could not be averaged out, because it was caused by particular pumping activities.

(3) The reliability and accuracy of the measurement could be judged by the magnitude of $\Delta T_{max} - \Delta T_{min}$. In normal conditions, it should be about the same for all the sensors. This was the case in the second run, which thus had a reasonable distribution $\Delta T(r)$ within the expected error range. As a result, the difference $\Delta T_{max} - \Delta T_{min}$ could be used as a criterion to make data analysis more convincing.

(4) For sensor 16, the actual error range in the 128-cycle run was $2.0 \pm 1.6\,\mu$K. Using an averaging ratio from Table 4-5, the estimated reading for sensor 16 would be 0.9 K.

In conclusion, if the bath stability is improved by one order of magnitude with a feedback loop to 0.2 mK, a 2 μK measurement with an accuracy of 10% could be easily achieved (as easy as sensor 13 detecting 20 μK). This sensitivity at 2 K is still above the 1 μK limit due to EMF noise (Table 4-2), which means that the bath stability still plays a major role in the detection limit.

Table 4-7: Two measurements at a power level of 0.5 μW

Sensor	First Run			Second Run		
	ΔT	$(\Delta T)_{min}$	$(\Delta T)_{max}$	ΔT	$(\Delta T)_{min}$	$(\Delta T)_{max}$
# 13 (μK)	$19.1_{\pm 49}$	-130	320	$20.6_{\pm 15}$	-21	63
# 14 (μK)	$14.6_{\pm 29}$	-140	80	$11.7_{\pm 16}$	-30	60
# 15 (μK)	$21.8_{\pm 162}$	-500	1210	$7.6_{\pm 22}$	-58	60
# 16 (μK)	$8.7_{\pm 66}$	-130	550	$2.0_{\pm 18}$	-60	48

Drifting Effect

Before showing the result of bath drifting, Table 4-8 showed the experimental conditions and the results calculated from a FORTRAN program (at 4.33 K). The reference resistance was measured before and after the measurement of the 16 mapping sensors. 10 points of 2048 readings were acquired each time. It took about 128 minutes to finish the mapping of the top plate, and the bath only drifted about 0.1%. Therefore, an average R_c was usually used to calculate R_m, because any error caused by this would be at least one order of magnitude lower than 0.1% (no disturbance happened by checking ΔT_{max} and ΔT_{min}). In addition, T_{Bath} for all 16 mapping sensors were within 0.01 K, suggesting they could be used as reproducible sensors to an accuracy of 0.01 K.

If bath drifting exists, the FORTRAN program uses an interpolated R_c to calculate R_m. The drifting effect was studied by a very slow pumping around 2.5 K. As shown in Figure 4-14, a 10 mK temperature change was barely affected by the big bath drifting (more than 150 mK). Table 4-9 shows average results at three different temperatures. The change of ΔT between the first and the third points is 3.20%, while the thermal conductivity change was 3.67%. The good agreement not only extends the application range of the method, but also proves the effectiveness of the pulse mode heating.

Thermal Conductivity

Sensors' responses at different temperatures between 20 Torr and 800 Torr were measured. Thermal conductivity was then calculated from eq. (4.18) assuming the thickness $h = 0.16$ cm. In the future, only the product κh will be used. Figure 4-15 shows results from two separate experiments. As a whole, the reproducibility is satisfactory. Below 100 Torr, the pressure was regulated by the VAT valve; both results were within 1% of error. Above 100 Torr, the bath temperature cannot be controlled nearly as well as it can below 100 Torr.

acquisition condition	mapping sensor	reference sensor
Number of readings per point	512	2048
Number of points per cycle	4	10
Number of cycles per run	128	2
Input signal	75	75
A/I amplifier gain	100	10
Bath drifting	**before the mapping**	**after the mapping**
R_{c1} (Ω)	1167.49	1166.07
R_{c2} (Ω)	1112.76	1111.41
R_{c3} (Ω)	1060.48	1059.22
R_{c4} (Ω)	1123.98	1122.68
Calibration heater power (mW)	4.465	
Temperature Conversion	$1/T = a_0 + a_1 (log\, R + 1/log\, R)$	
Sensor	T_{on} (K) (heater ON)	T_{Bath} (heater OFF)
1	4.423	4.333
2	4.394	4.338
3	4.360	4.341
4	4.355	4.336
5	4.447	4.339
6	4.394	4.335
7	4.382	4.339
8	4.355	4.335
9	4.436	4.338
10	4.393	4.339
11	4.363	4.335
12	4.349	4.333
13	4.422	4.335
14	4.388	4.330
15	4.366	4.337
16	4.342	4.334

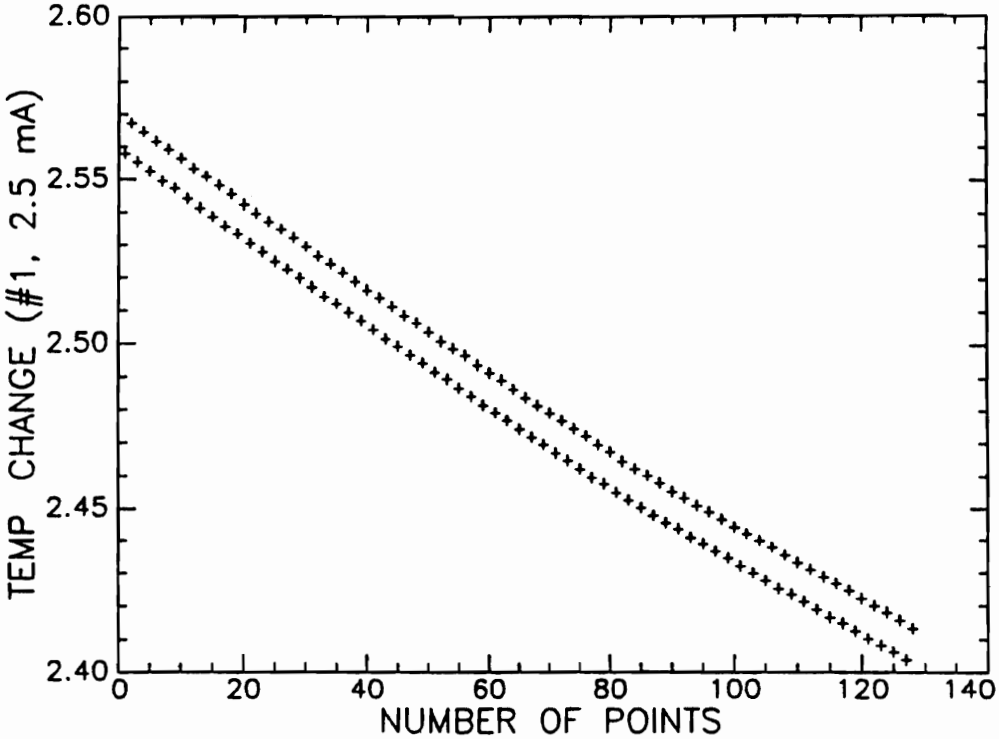

Figure 4-14: Temperature change measurement in a drifting bath

Table 4-9: Temperature changes in a drifting bath

Average Temperature (K)	Temperature change of sensor 1 (mK)
2.335	10.10
2.405	9.85
2.470	9.79

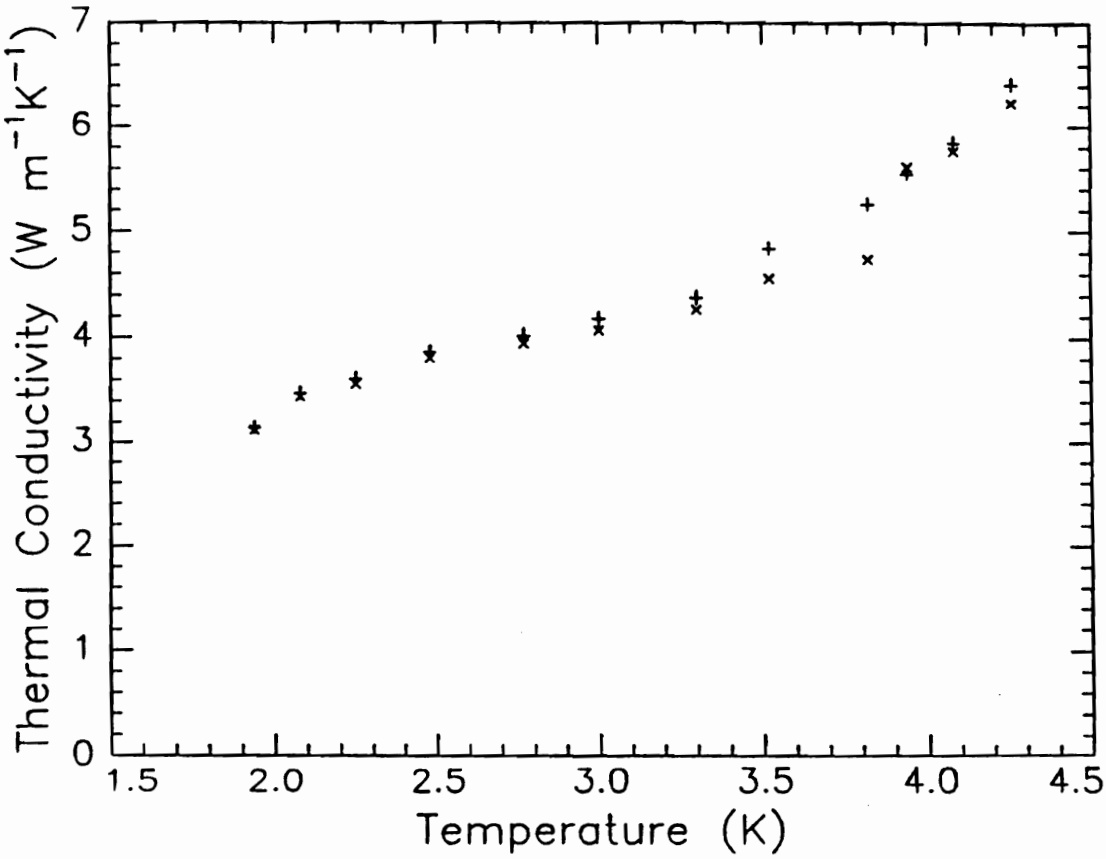

Figure 4-15: Thermal conductivity between 1.96 K and 4.31 K

Conclusion

In summary, except for a very weak signal or unstable bath, the accuracy of the calorimetric measurement reaches 1% for one cycle (within 100 s). The bath temperature fluctuation is the dominant error source. If the bath fluctuation could be reduced by one order of magnitude, the temperature resolution could easily reach 2 μK. At 20 Torr, the thermal conduction calibration was also within an error of 1%.

4.5.2 Calorimetric Measurement of RF Heating

Two types of experiments were done, as mentioned in Section 3.4. One was done in an unshielded cryostat, and residual resistance of 2.24 $\mu\Omega$ due to frozen-in magnetic flux was measured for the triaxial cavity. As will be shown below, it can be used as an example to show the agreement between the calibration heater and the RF heating. The other was done in a well shielded cryostat, which yielded a 0.4 $\mu\Omega$ surface resistance. The calorimetric measurement results not only agree with the RF measurement results, but also indicate field emission occurrence and its locations.

Calculation of Surface Resistance

The following steps were taken to calculate surface resistance by the calorimetry method:

1. Data acquisition and storage: Scanning the 16 mapping sensors when the RF power was in pulse mode; saving all the data to a file.

2. Calculating resistance for every point (averaging 128 or 512 readings), converting them to temperature, then calculating the temperature changes (eq. 4.9).

3. Using the measured κh and the temperature distribution, calculating the RF heating power P_{plate} according to the sensor's position (Section 4.2).

4. Using the maximum electric field measured by RF measurement method, calculating the surface resistance (assuming the losses were uniformly distributed, and the temperature distribution was cylindrically symmetric):

$$R_{Nb} = \frac{R_{Cu}\, E_{Cu}^2}{P_{Cu}} \frac{P_{plate}}{E_{max}^2} \tag{4.13}$$

where $R_{Cu} = 10.04$ mΩ is the surface resistance of copper at 1.5 GHz, $P_{Cu} = 2.239$ W at $E_{Cu} = 10$ MV/m; E_{max} and P_{plate} are the maximum electric field in the superconducting niobium cavity and the RF power losses on the cavity top plate. The relation $E_{max} \propto H_s$ has been used in the formula.

Measurements in an Unshielded Cryostat for Calibration

Temperature changes at different RF levels were measured with the same set of temperature sensors before the heater calibration measurement. 200 points (128 readings per point) were acquired for each run, which lasted about 5 cycles. Figure 4-16 shows the signal output of sensor 1 (r = 10 mm) at a field level of 4.64 MV/m.

As can be seen, the bath temperature was quite stable. Although the number of readings at each point was four times fewer (points more scattered), the average of all the points had the same effect. The error for the bath level was $\pm 19\,\mu$K, which was the same as before. The error from the upper level was $\pm 122\,\mu$K. This error had nothing to do with the calorimetric measurement. It was from the drifting RF power level. For better accuracy, a larger gain amplifier is needed to reduce the time constant, and a feedback loop is needed to set a constant power level. From the five cycle average, the temperature change caused by the RF losses was 4.58 ± 0.11 mK, which was dependent on the state of the RF equipment.

Fitting this temperature change and the sensor position to the curve of Figure 4-1, the P_{loss} in the top plate was 115.8 μW. Using the measured electric field 4.64 MV/m, the surface resistance was 2.41 $\mu\Omega$. This was 10% larger than the value given by the Q measurement,

which was probably caused by variations in anomalous losses such as surface contaminants. In addition, the drifting power level also affected the accuracy of the field measurement. Measurement results at different field levels are given in Table 4-10. At high field, the surface resistance was about the same, suggesting there was no field emission site, or no local heating on the top plate. As can be seen, the measurement of electric field strength has an even error when the power losses were small ($E_{max} \propto \sqrt{P\,Q}$). The last column is the ratio of the measured RF losses P_{plate} to the measured total RF losses P_{loss}. The η_{plate} is consistently larger than 0.795% (Table 3-2), which indicates there were more losses from contaminants on the top plate than on the rest of the cavity .

Figure 4-17 shows three sets of data. One was from the heater calibration (Table 4-5). The second was from the measured P_{plate} from ΔT. P_{plate} was multiplied by a reduction factor of 0.865 because these two heating configurations have different distribution factors. The RF heating only has 93% of the power contributing to the temperature change, and some of the power has a shorter path. From the models, the reduction factor between the RF power and the heater power is 0.865 at 10 mm. The third line was from the measured total power, which was multiplied by a factor of 0.74% to obtain the best fit. The theoretical model expects a factor of 0.69%, which suggests larger RF losses due to contaminants on the plate. These three lines agreed very well, which yielded three observations:

(1) The theoretical expectations for the calibration heater and the RF heating only had a difference of 7% with the measured results. This may come from variations in the anomalous losses which change the cylindrical distribution.

(2) It is known that anomalous losses affect the power loss distribution but do not affect the field distribution inside the cavity. The fact that the measure η_{plate} was larger than the expectation value suggests that the anomalous losses in the cone part were lower than those on the top plate. This ratio held approximately constant up to 11 MV/m. The difference from the P_{loss} was 11.3%, which was also related to different anomalous losses on the plate. It needs to be pointed out that P_{loss} will only be used to calculate the field.

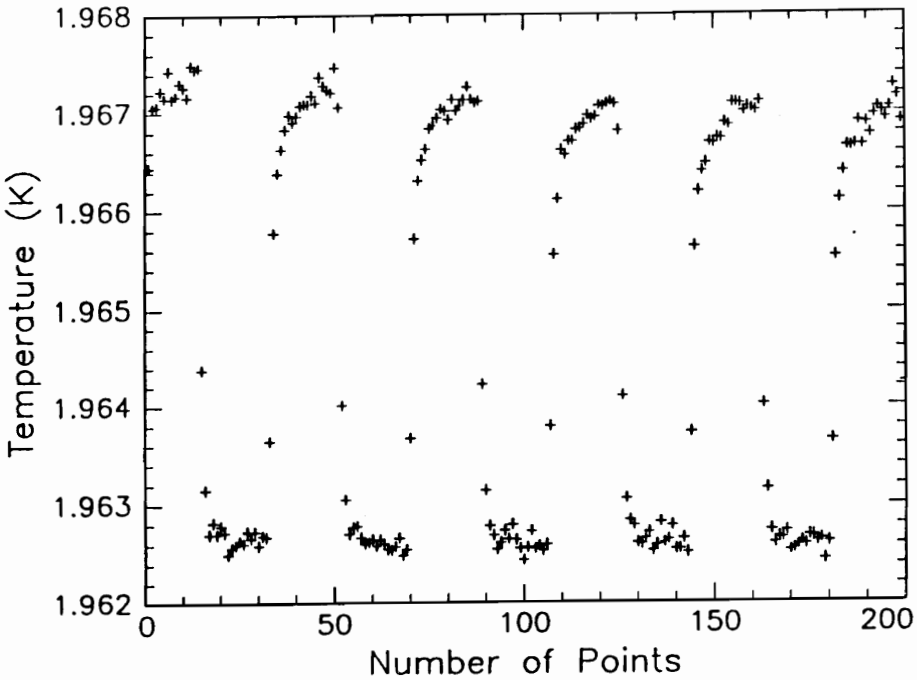

Figure 4-16: 200 points data acquisition in 5 RF cycles

Table 4-10: Surface resistance results (unshielded cryostat)

ΔT_{m1} (mK)	E_{max} (MV/m)	P_{plate} (μW)	R_s ($\mu\Omega$)	P_{loss} (mW)	η_{plate}
0.462	1.32	11.9	3.07	1.10	1.08%
1.474	2.46	38.2	2.82	3.62	1.05%
4.486	4.64	115.8	2.41	12.8	0.90%
9.126	6.69	235.8	2.36	26.2	0.90%
17.823	9.32	459.3	2.37	51.0	0.90%
28.980	11.79	748.2	2.41	80.8	0.93%

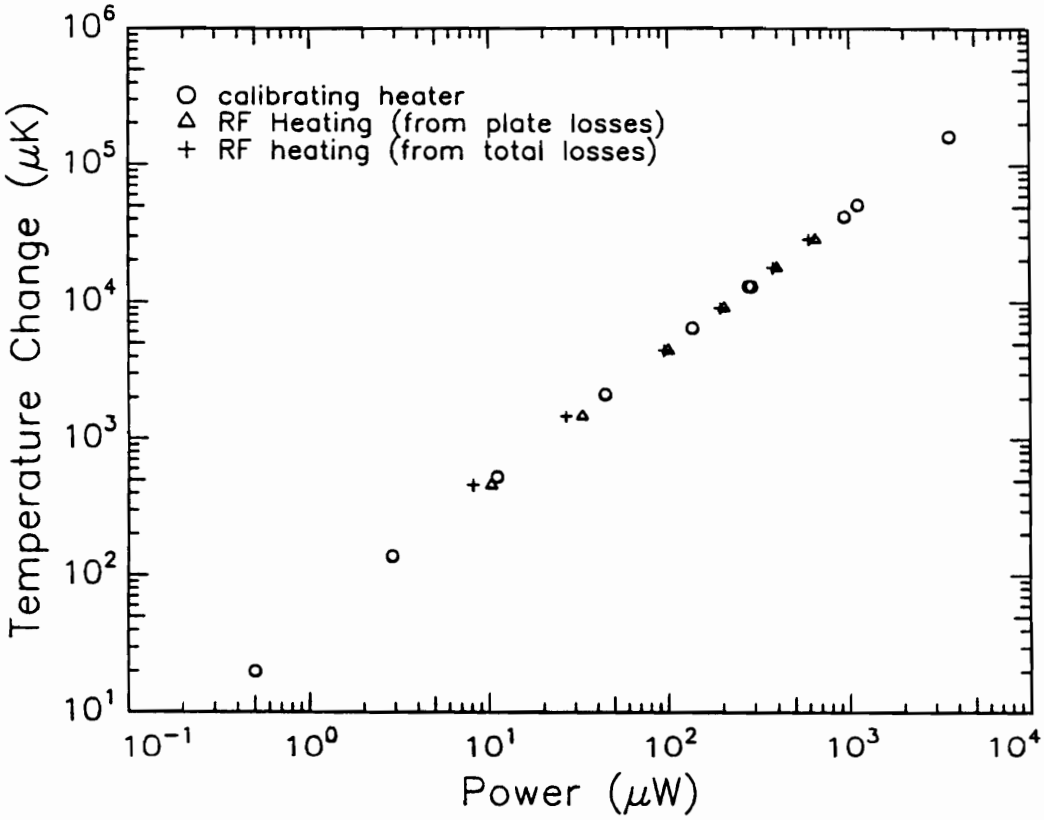

Figure 4-17: RF heating calibrated with the calibration heater

(3) The constant ratio η_{plate} suggests that there is no appreciable indium joint losses in the measurement. Moreover, the linearity of the third set of data indicates that the RF losses distributed uniformly on the cavity walls due to the large residual resistance caused by magnetically trapped flux.

(4) Both the difference in anomalous losses on the plate and the drifting RF power are causes of the deviation from the expected value, which cannot be averaged out in the measurement method. They need to be analysed and eliminated through better control and careful analysis. Compared to the accuracy of RF measurement, which is normally at least 5% to 10%, this 7% deviation (including anomalous losses) was a satisfactory result when comparing these two methods.

In summary, the heating power calibration agrees well with our model. Variations in the anomalous losses from one part of the cavity to another are responsible for the 10% larger surface resistance value than that from the Q-measurement method. There is no field emission on the top plate for a clean cavity. The uniform 0.74% loss factor of the top plate also suggests that there is no field emission at any other location.

The above experiments serve as an overall calibration for the conduction of the top plate and the calorimetric measurement system. This will save a lot of time in checking each component and each instrumentation level.

Measurements in a Shielded Cryostat

A calorimetric measurement was also done in Dewar 1 after it was magnetically shielded. As mentioned earlier, the cavity Q was 1.1×10^8, yielding an averaging surface resistance of 0.4 $\mu\Omega$. Table 4-11 gives the corresponding top plate surface resistance results. The field level measurements started from 5 MV/m, since multipacting always occurred below that level. Results from the table are:

(1) At 5.02 MV/m, R_{m9} had the smallest value of 0.52 $\mu\Omega$ among the inner ring sensors (sensor 1, 5, 9, 13). It was 30% higher than the 0.4 $\mu\Omega$ value from Q measurement, indicating the existence of a lossy spot.

(2) At lower field levels, R_{m2} was consistently larger than R_{m1}. At higher field levels ($E_{max} > 28.4$ MV/m), R_{m1} was larger than R_{m2}. In addition, R_{m9} was always the smallest. This distribution indicates that there was a field emission site near sensor 1 towards sensor 13. or that a field-dependent variation in anomalous losses on various parts of the surface was present.

(3) The theoretical model ($\int_r^{r_0} p(r)\, dr/r$) drops faster than the real temperature distribution, which causes a systematically higher surface resistance result for the outer ring sensors.

(4) Because a small change 0.17 mK was obtained only in 5 cycles (sensor 8 at 5.02 MV/m), the R_s from the outermost ring was not cited in above discussion.

As a whole, a lossy spot was observed using the calorimetric measurement. The losses of the spot were approximately proportional to E^2 at low field levels. At high field levels, it appeared to be an emission site due to the rapid change in R_s with field. Due to this lossy spot, the R_s measured by the calorimetry method is 25% higher than that measured by Q-measurement method. The higher R_s in the outer rings needs further studies to be understood.

4.5.3 Observation of Multipacting

Besides field emission, multipacting caused by adsorbed gas layers was observed. Figure 4-18 shows a disappearing process of multipacting caused by the adsorbed gas layer. The flat curve was the bath temperature measured with the germanium sensor; the other curve was the temperature with time recorded by sensor 1. The sensor sensed severe multipacting at first. Then the multipacting losses became smaller, while the stored energy or the field

Table 4-11: Surface resistance results (shielded cryostat)

Field (MV/m)	5.02	10.57	14.44	21.56	28.4	30.77
R_s ($\mu\Omega$) #1	0.668	1.042	1.098	0.975	1.456	2.734
R_s ($\mu\Omega$) #2	0.874	1.252	1.250	1.119	1.439	2.625
R_s ($\mu\Omega$) #3	0.845	1.464	1.408	1.259	1.616	2.958
R_s ($\mu\Omega$) #4	0.910	1.570	1.396	1.305	1.672	3.127
R_s ($\mu\Omega$) #5	0.637	1.123	1.169	1.050	1.274	2.073
R_s ($\mu\Omega$) #6	0.727	1.384	1.367	1.219	1.484	2.474
R_s ($\mu\Omega$) #7	0.678	1.464	1.374	1.251	1.530	2.592
R_s ($\mu\Omega$) #8	0.468	1.848	1.541	1.446	1.775	3.047
R_s ($\mu\Omega$) #9	0.518	0.811	0.882	0.798	1.054	1.852
R_s ($\mu\Omega$) #10	0.499	0.878	0.950	0.861	1.157	2.094
R_s ($\mu\Omega$) #11	0.636	0.981	1.020	0.938	1.252	2.290
R_s ($\mu\Omega$) #12	0.489	1.188	1.147	1.065	1.413	2.630
R_s ($\mu\Omega$) #13	0.529	0.874	0.961	0.859	1.294	2.552
R_s ($\mu\Omega$) #14	0.544	0.976	1.057	0.948	1.387	2.744
R_s ($\mu\Omega$) #15	0.505	0.984	1.003	0.904	1.326	2.642
R_s ($\mu\Omega$) #16	0.481	1.114	1.021	0.966	1.423	2.854

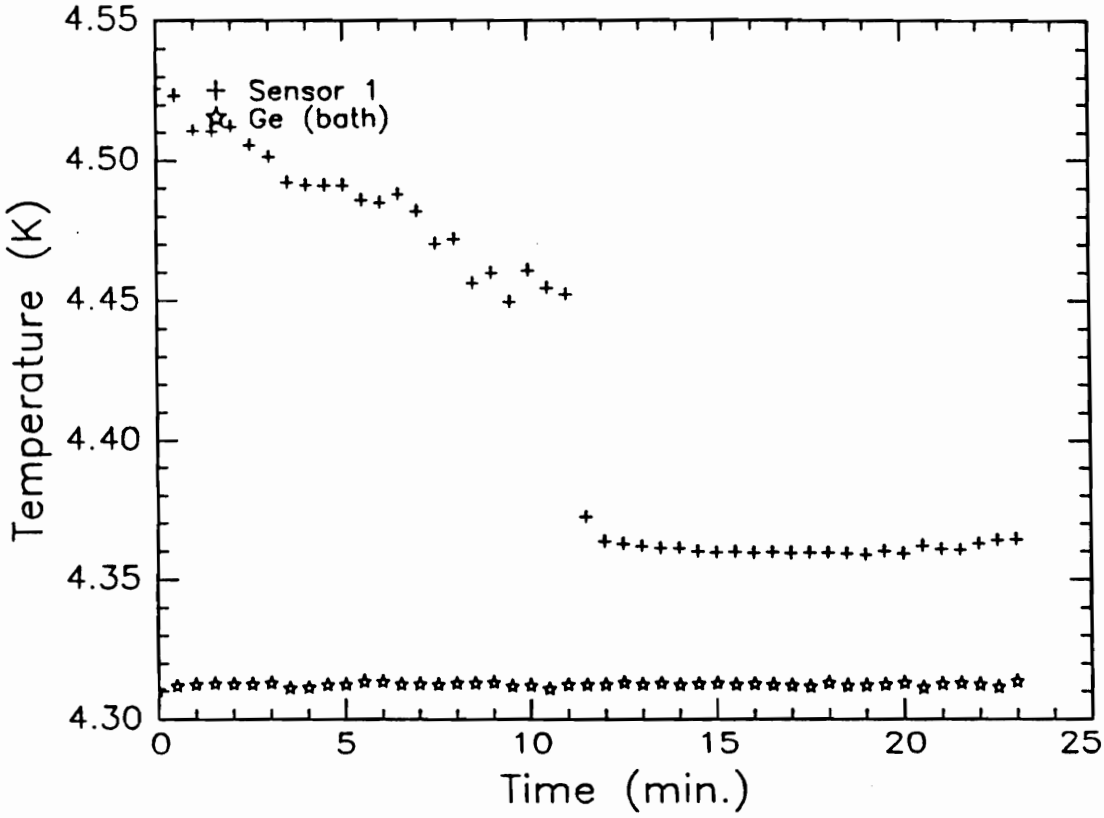

Figure 4-18: Observation and monitoring of multipacting on the cavity top plate

level became larger (P_t increased). This means the power losses on the plate decreased while the surface magnetic field increased, which leads to the conclusion of multipacting from a desorbing gas layer. After the condensed gas layer evaporated away, the temperature change stayed at a stable value. Fortunately, this kind of multipacting was not caused by clean niobium, and it could be eliminated with RF power processing. It was experimentally verified that the processing time was directly related to the vacuum pressure of the system before its cooldown.

4.6 Concluding Summary

In summary, an inexpensive scanning board has been made and used for temperature mapping of a 4 by 4 carbon resistor array. The detection limit of the temperature change is smaller than 2 μK with the present bath control conditions, and was achieved in two-hour, 128-cycle runs. If the bath is stabilized by a feedback loop, such a resolution can be achieved in a much shorter time.

The dominant *noise* source was from the bath temperature fluctuation. For a 512 readings per point, 8-point cycle run, the absolute error from the bath and the electronics is smaller than 30 μK in the normal bath condition, i.e., a 2 mK fluctuation range. This will give an accuracy of 1% for any signal larger than 3 mK, and this is done within 100 s.

When this calorimetric method was applied to the top plate of the triaxial cavity, the above results were verified with a calibration heater. The temperature change is proportional to the applied power, and the thermal conduction product $\kappa\, h$ of the top plate is measured for future RF measurements. Moreover, RF losses on the plate were also measured at different field levels. There is only a 7% difference between the two heating configurations, which partly comes from a 10% larger surface resistance due to spatial variations in anomalous RF losses. As a result, these two methods agree very well in the intermediate power range.

In the ideal case, if the highest field is 30 MV/m (surface magnetic field of 52 Oe), and the detection limit of the temperature change is 2 μK, the detectable power will be 0.05 μW and the minimum detectable surface resistance will be 0.02 nΩ (Figure 4-1).

The limitations to this fast, accurate, and convenient method come from factors not related to the method itself, i.e.: (1) the position of the sensor: the uncertainty of that is half the width of the flat surface on the sensor, or 0.4 mm, (2) the controllability of the RF power source, which is now in a free-run pulse mode and requires a feedback loop to control the power amplitude, and (3) the reduction of anomalous RF losses, so that the usage of the simple model will not cause any inconsistency. At any rate, the overall accuracy of the calorimetric measurement is comparable to that of the RF method, but it has a much better sensitivity in the measurement range of interest for planar samples, or materials which cannot be machined to a cavity shape. This will be shown in Chapter 5, which describes the measurement of high-T_c superconducting films with the niobium triaxial cavity described in Chapter 3 and the calorimetry method developed and described in this chapter.

Chapter 5

Measurement Results of High T_c Superconducting Thin Films

In Chapter 3 and Chapter 4, fundamentals of surface resistance measurement have been discussed. Results from the RF measurement method and the calorimetric measurement method have agreed with each other. In this chapter, the temperature distribution caused by a 25.4 mm diameter sample will be given (1.0 mm gap), and the measurement results will be presented and discussed.

5.1 Measurement of $YBa_2Cu_3O_7$ Thin Films

5.1.1 Temperature Distribution of RF Heating

Figure 5-1 shows the calculated heat flux distribution and temperature change distribution curves for different sample R_s's, i.e., $R_s = R_{Nb}$, $R_s = 10\,R_{Nb}$, and $R_s = 100\,R_{Nb}$. As can be seen, the losses of a 25.4 mm diameter sample on the plate are 88.7%, 98.7%, and 99.9% respectively, of the total losses on the plate. The temperature distribution for $R_s > 10\,R_{Nb}$

is almost the same as that of $R_s = 100\,R_{Nb}$ (the difference of ΔT_{max} is only 1.2%). For high-T_c superconducting samples, the curve of $R_s = 100\,R_{Nb}$ will be used as the model.

5.1.2 Measurement of High-T_c Superconducting Thin Films

Two 25.4 mm diameter $Y_1Ba_2Cu_3O_7$ thin films were tested with the triaxial cavity. One was prepared with the MOCVD method two weeks before the test (Sample I). The other was prepared by the laser ablation method (Sample II) and had been through various kinds of tests, including an irradiation test in space. The samples have a dramatic difference in surface resistance at 2 K, even though they have about the same superconducting transition around 80 K. The surface resistance reported here is the effective surface resistance, which does not make any correction for the finite thickness of the films.

Measurement with a Network Analyser

Measurements were done with a network analyzer at room temperature and at the high-T_c superconducting transition region. Table 5-1 shows the results of two samples and the URMEL calculation result. Figure 5-2 shows the resonant peak at room temperature with Sample II in the cavity (the cryostat is at 800 Torr), which shows a dramatic reduction of Q_c. The difference between 1428 MHz in the figure and 1452 MHz in the table was due to the cryostat pressure outside the cavity. In the experiment, β_1 and β_2 were chosen to be very weak so that $Q_L \simeq Q_0$. The URMEL results and the experimental results agree well in frequency. The Q drop involves many reasons, which are not of interest in this research.

The cavity Q_c' with Sample 2 at 2 K was 23000, which yielded a surface resistance of 0.15 Ω. Although superconducting transition was observed around 80 K, its quality deteriorated dramatically due to handling and aging.

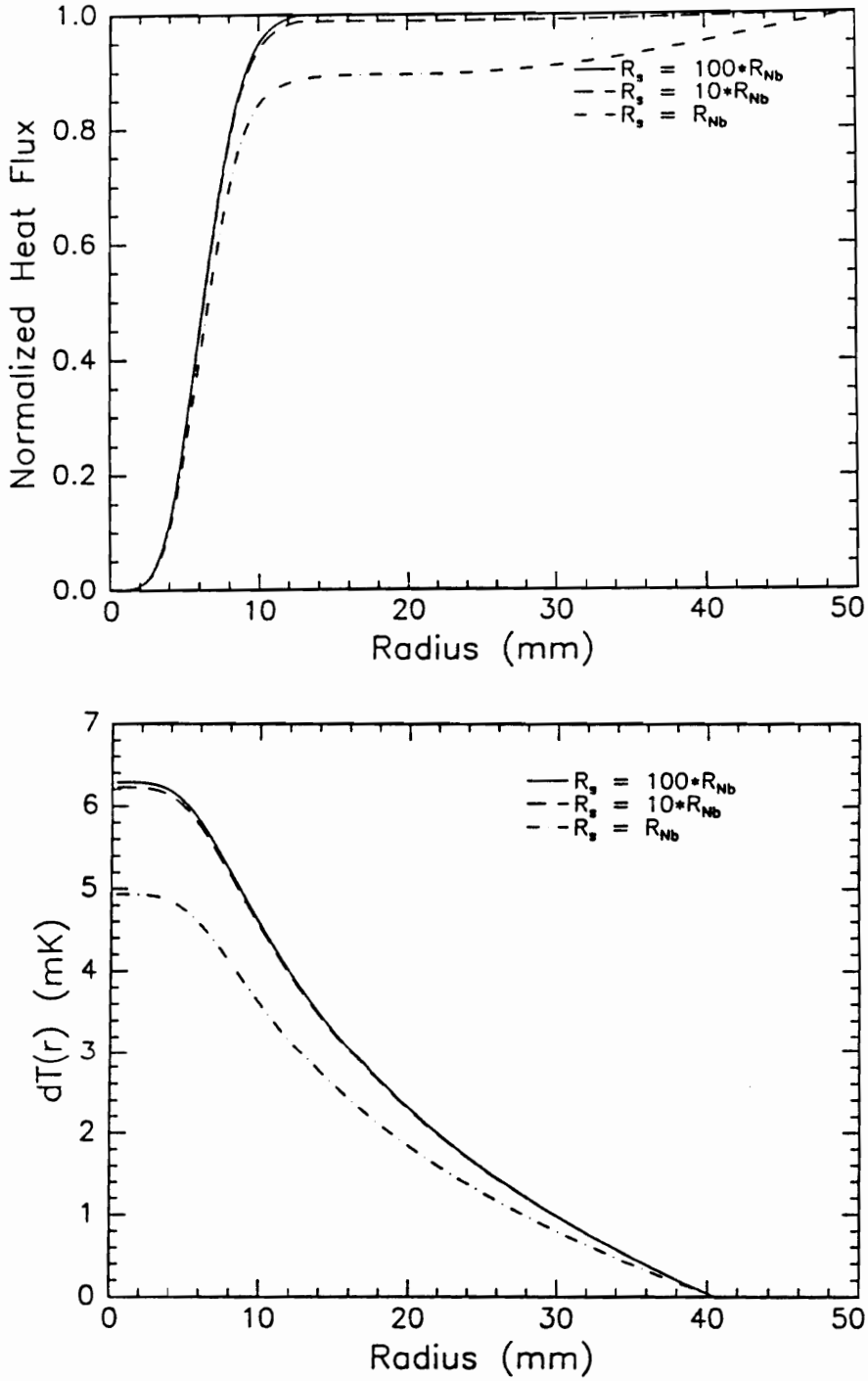

Figure 5-1: Flux distribution and temperature distribution (R_s = 1, 10, 100 R_{Nb})

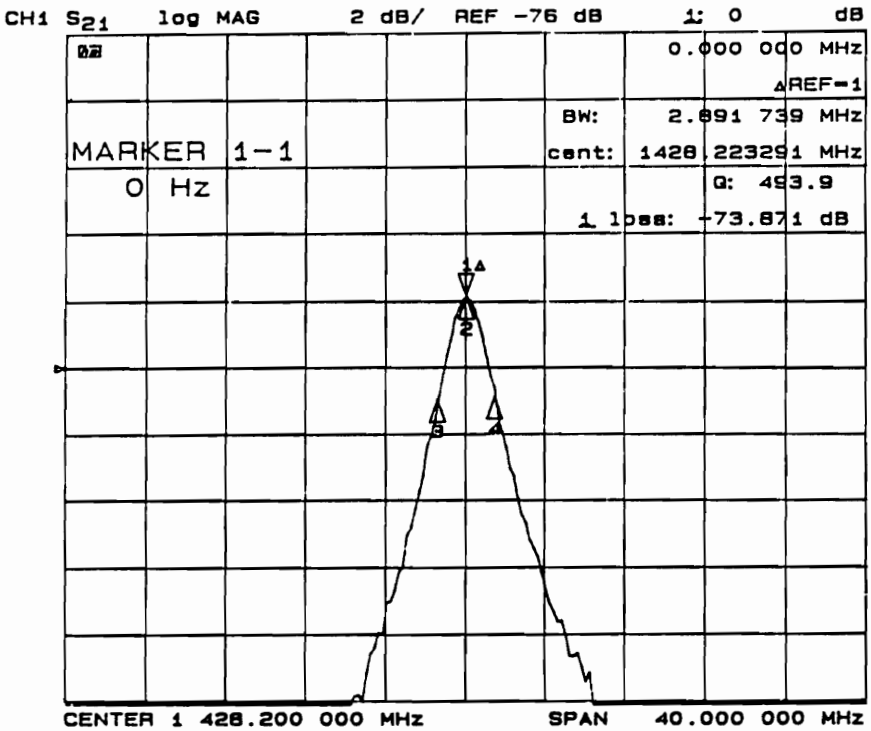

Figure 5-2: Resonant peak of the cavity with Sample II

Table 5-1: RF measurement results of YBCO films (f and Q_c)

300 K, vacuum on both sides	f (MHz)	Q_c
Meas. Results (1.5 mm gap)	1524	1600
URMEL Results (1.5 mm gap)	1552	1646
Meas. Results (Sample I)	1442	320
Meas. Results (Sample II)	1452	500
URMEL Results (1.0 mm gap)	1461	1600

Measurements at 2 K

The RF measurement principle and setup have been described in Chapter 2 and Chapter 3. Only the measurement results are presented here.

Sample I was tested after many RF tests of the empty triaxial cavity. The empty cavity Q_c in a shielded cryostat was only 1.5×10^7 due to contamination on the cavity surface. This is approximately one order of magnitude below the best Q_c achieved in a newly cleaned cavity. Severe anomalous losses were also observed over a large range of field levels. As mentioned before, one of the advantages of the calorimetric measurement is that it directly measures the RF losses on the sample. The measurement results do not depend on the condition of the parent cavity. With the sample, the Q_c' of the cavity was 8×10^6 at 2 K. Using $G = 43.50$, $\eta_{25.4mm} = 1.05\%$ (Table 3-1), and equation (2.30), the measured surface resistance was 245 $\mu\Omega$.

Figure 5-3 shows the responses of sensors in the first column (sensor 1 to sensor 4, 3.50 MV/m). The results are presented in Table 5-2, which also includes the sensors' responses at two more field levels. Results of column II are not given because there was a problem with pre-amplifier II. The results of other sensors were not affected, as can be seen from Figure 5-3. Data acquisition in Figure 5-3 was done within 3 minutes (100 points, each having 128 readings). The RF source was quite stable for such a short period. Table 5-3 shows surface resistance results calculated from Table 5-2 and the calculated ratio relative to R_{m1}.

From Table 5-2 and Table 5-3, the following results can be obtained:

(1) At 3.50 MV/m, the surface resistance measured by the 12 mapping sensors ranges from 28.1 $\mu\Omega$ to 52.7 $\mu\Omega$. Unlike the results in Table 4-11, where the outer ring resistance was constantly larger than those of the inner ring, results for Sample I are more consistent. This is because the effect of anomalous RF losses on a 35 $\mu\Omega$ sample is far less important than on a 0.4 $\mu\Omega$ niobium plate. This also suggests the results in Table 4-11 did come

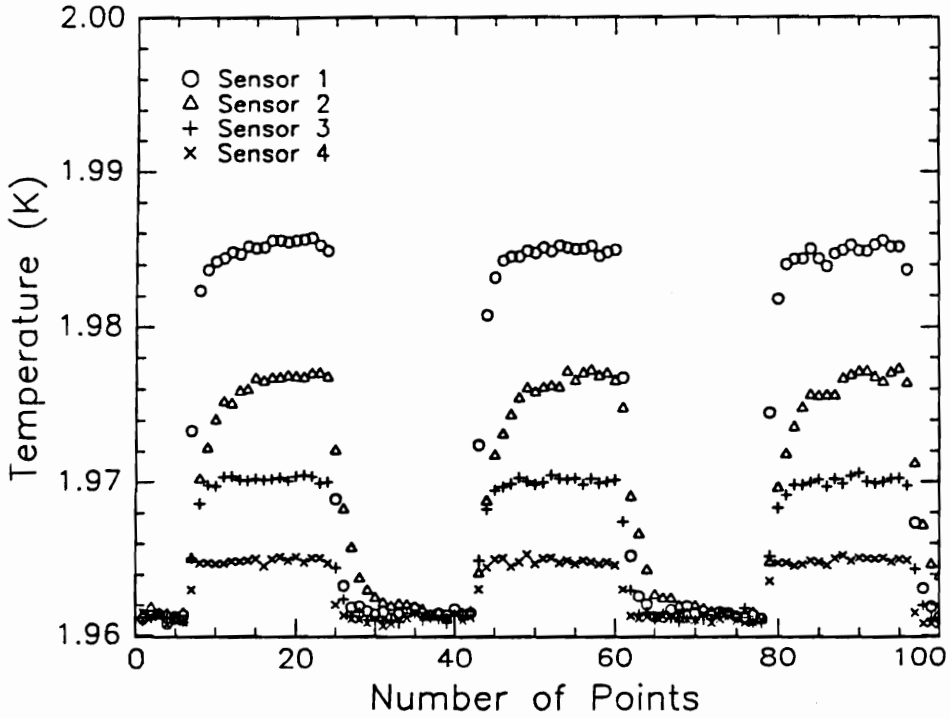

Figure 5-3: Temperature change of sensor 1 – 4 due to RF heating on Sample I

Table 5-2: Temperature changes at different field levels (YBCO)

Sensor (mK)	E_{max} (MV/m)		
	3.50	3.60	6.75
$\Delta T(r_1 = 11.8$ mm)	23.86	23.20	112.17
$\Delta T(r_2 = 18.4$ mm)	15.22	14.92	69.23
$\Delta T(r_3 = 27.9$ mm)	9.02	8.88	43.62
$\Delta T(r_4 = 34.7$ mm)	3.83	3.80	19.09
$\Delta T(r_9 = 9.1$ mm)	42.48	41.51	196.49
$\Delta T(r_{10} = 17.8$ mm)	30.70	29.92	141.56
$\Delta T(r_{11} = 28.3$ mm)	12.39	12.19	57.92
$\Delta T(r_{12} = 33.9$ mm)	6.84	6.72	30.73
$\Delta T(r_{13} = 10.2$ mm)	33.56	32.62	156.14
$\Delta T(r_{14} = 18.4$ mm)	23.52	22.81	109.30
$\Delta T(r_{15} = 27.4$ mm)	10.56	10.11	48.31
$\Delta T(r_{16} = 35.9$ mm)	5.19	5.04	25.28

Table 5-3: Surface resistance of high-T_c superconductors (YBCO)

	E_{max} (MV/m)			Normalized to #1		
	3.50	3.60	6.75	3.50	3.60	6.75
R_s ($\mu\Omega$) #1	28.4	26.1	35.8	1.00	1.00	1.00
R_s ($\mu\Omega$) #2	28.1	26.0	34.4	0.99	1.00	0.96
R_s ($\mu\Omega$) #3	34.1	31.8	44.4	1.20	1.22	1.24
R_s ($\mu\Omega$) #4	34.9	32.8	46.8	1.23	1.26	1.31
R_s ($\mu\Omega$) #9	36.4	33.3	45.6	1.29	1.28	1.28
R_s ($\mu\Omega$) #10	41.9	38.1	54.6	1.48	1.46	1.52
R_s ($\mu\Omega$) #11	42.0	38.7	52.0	1.48	1.48	1.45
R_s ($\mu\Omega$) #12	44.7	41.2	55.4	1.58	1.58	1.55
R_s ($\mu\Omega$) #13	51.6	48.0	64.9	1.82	1.84	1.81
R_s ($\mu\Omega$) #14	52.7	48.9	63.7	1.86	1.88	1.78
R_s ($\mu\Omega$) #15	35.4	32.5	44.3	1.25	1.25	1.23
R_s ($\mu\Omega$) #16	43.4	39.8	54.3	1.53	1.53	1.51

from anomalous RF losses, which raised the plate temperature as a whole and resulted in a higher ratio to the theoretically calculated temperature.

(2) When the results from the fourth ring (sensor 4, 12, and 16) are neglected and the results of sensor 13 and sensor 14 are treated as sample quality differences, the average surface resistance is $35.2 \pm 6.2\ \mu\Omega$.

(3) The surface resistance results at 3.60 MV/m are smaller than those at 3.50 MV/m. As can be seen from the temperature change table (Table 5-2), the temperature changes at 3.60 MV/m are actually smaller than those at 3.50 MV/m. The error is a result of the field measurement, which will be discussed later.

(4) At 6.75 MV/m, the resistance values increased 25% as shown by all 12 sensors. The uniformity of this increase indicates that the increase was due to an actual R_s increase rather than to field emission. The power losses on the top plate were about 2 mW at this power level.

In summary, the temperature change caused by RF heating of a $Y_1Ba_2Cu_3O_7$ thin film sample (25.4 mm in diameter, 4000 Å thick) was measured. Results among 12 sensors agreed with each other at different field levels, and they were also consistent with results measured on the niobium top plate. The measured surface resistance of the sample at 3.5 MV/m, or 6.1 Oe on the sample, was $35.2 \pm 6.2\ \mu\Omega$.

5.1.3 Experimental Error

Error from the calorimetric measurement

As mentioned earlier, the major error does not come from the measurement system (MIO-16 board plus scanning board). Nor does it come from the bath fluctuation. Both factors contributed less than a 1% error to a 3 mK change of a one-cycle measurement. Part of

the error comes from the positioning accuracy of the sensor. An estimation of the position accuracy is 0.4 mm, which yields an error of $\sim$ 4% for ΔT. This suggests that part of the spread of R_s in Table 5-3 was from the difference of the temperature distribution.

In addition, there may be a systematic error of 4% from $\kappa\, h$, which was introduced in the heater calibration due to the uncertainty of the sensor position.

Error from the RF measurement parameters

As discussed above, the error introduced by the calorimetric measurement is less than 8%. A 5% field measurement error will result in a 10% measurement error in surface resistance which cannot be averaged out even for a uniform sample. The following discussion is a rough estimate of the field measurement errors.

The field level E_{max} was determined by

$$\begin{aligned} E_{max} &= C\sqrt{P_{loss}\, Q_c} \\ Q_c &= \omega\,\tau\,(1+\beta_1) \\ P_{loss} &= P_I - P_R - P_T = c_i\, p_i - c_r\, p_r - c_t\, p_t \end{aligned} \tag{5.1}$$

where C is a constant determined by the URMEL program; p_i, p_r, and p_t are readings of the incident power, reflected power, and transmitted power on the RF power meter; c_i, c_r, and c_t are the respective cable and coupler calibration coefficients, which calibrate RF losses along the cables and reductions from directional couplers and power splitters.

The error of Q_c is determined by three factors, which results in an uncertainty of 6%:

1. Frequency measurement: at 1.96 K, the fractional frequency stability is better than 1×10^{-6}. The measurement error is in the same range and can thus be neglected.

2. Time constant measurement: In the best case, the measurement error should be within 5%, which is determined by the oscilloscope.

3. β_1 measurement: The error term is determined by $\Delta\beta_1/(1+\beta_1)$. For $\beta_1 = 0.1$, a 10% error would be the worst case. This would be only an error of 1% on Q_c.

For the power loss measurement, the reading of the power meter had a reproducibility better than 0.5%. The coefficients c_i and c_r had only 1.0% and 1.3% errors in calibration in four different runs. However, the calibration was heavily dependent on the calibration kit, which might have had a systematic error of 3 to 5%. This would result in a 10% error in the P_{loss} measurement. (Note: P_t is about three orders of magnitude smaller than P_i and P_r and can be neglected in the error estimation.)

If the gap had a 0.05 mm deviation from the design value of 1.5 mm, the error of the coefficient C would be 6%. As a result, these three factors yield a total error of 16% in E^2_{max}, or an 8% error in E_{max}. In addition, the power drifting would typically cause a 5% error, which yield a total RF parameter error of 21%.

The total error combined from E_{max} and ΔT is less than 30%. If only the random error in R_s is counted, it would be within 15% including the drift. The scattering of the surface resistance data between sensors may come from three factors: (1) the quality of the sample, (2) the substrate losses due to a film thickness comparable to the penetration depth, and (3) variations in the thermal conduction of the Apiezon grease. More studies are needed to identify these three factors.

5.2 Discussions

5.2.1 Application of the Calorimetric Measurement Method

Using the calorimetric measurement method, the surface resistance of a 25.4 mm diameter $Y_1Ba_2Cu_3O_7$ thin film (epitaxially grown by MOCVD) has been measured. The result is 35.2 $\mu\Omega$ at a surface magnetic field of 6.1 Oe (E_{max} = 3.6 MV/m) and at 2 K. Other conclusions about the result and the method are as follows.

(1) At a surface magnetic field of 6.1 Oe, the temperature change is 42.5 mK (sensor 9 in Table 5-3). For a 1 $\mu\Omega$ sample, the temperature change will be 1.17 mK, which is in the middle of the range of this measurement method. In this range, the measurement error is 30%. For other conventional existing methods, the detection limits are in the range of tens of $\mu\Omega$. The uncertainty of those methods comes not only from the RF parameters but also from the methods themselves, which could have an error of 1000%.

(2) The surface resistance from the Q measurement is strongly dependent on the condition of the cavity. Using the filling factor η_i to calculate R_s would cause a much larger error than using the electric field E_{max}.

(3) If the RF power is controlled with a feedback loop, the error of the calorimetric measurement could be reduced to about 25%. If the systematic error is ignored, the random error could be as small as 7%. It can be used to determine the relationship between the residual resistance and the magnetic field, i.e., the weak link response to the surface magnetic field. No method has sufficient accuracy and sensitivity to study the behavior of residual resistance of high-T_c superconductors except the calorimetric method.

5.2.2 Sample Quality

When compared to other reported results (e.g. Table 2-2: ref. [49] and [48]), 35.2 $\mu\Omega$ at 1.5 GHz is not the best result reported. However, it is the best result reported for such a large area sample. Using Sample II as an example, it had a similar transition to Sample I around 80 K. If it were cut into small pieces, it might have a small area which had superior surface resistance values. This suggests that for practical applications the overall performance has to be taken into account for large area samples. In addition, the reported 17 $\mu\Omega$ and 25 $\mu\Omega$ in those two references do not represent the real status of thin film fabrication technology today, because there have been no other supporting data for such superior results of $Y_1Ba_2Cu_3O_7$ samples at 77 K and $Bi_2Sr_2Ca_1Cu_2O_8$ samples.

5.2.3 Scaling of f^2

As mentioned in Chapter 1, an f^2-law is widely perceived and accepted for residual resistance. It has been common to scale results at 100 GHz down to 10 GHz. This assumes there are no constant residual losses or losses proportional to ω. It should be noted that this kind of scaling always gives optimistic results of surface resistance, and some room has to be reserved for questioning. Because it has not been proven at the present, the use of the f^2 down-scaling should be avoided as much as possible. Moreover, there is no answer to the question of how many loss mechanisms are responsible for the residual resistance yet.

On the other hand, scaling up with the f^2 relation will not cause any problems, except for the possible sacrifice of good results. When scaled to 5.66 GHz, a frequency reported in ref. [45], the 35.2 $\mu\Omega$ value at 1.5 GHz is 500 $\mu\Omega$ or 0.5 mΩ. This is quite reasonable when compared to the reported polycrystalline result of 5.6 mΩ.

5.2.4 Surface Resistance Used for Evaluation of Thin Film Qualities

Because surface resistance is the result of interaction between the electromagnetic wave and electrons in the surface layers, it is a very effective probe to test the quality of thin film samples. As a result, surface resistance measurement results have been used to show the quality of the samples or the preparation methods. In addition to the f^2 downscaling mentioned above, one has to be extremely careful in comparing R_s results measured using different methods. This is because calibration standards were usually involved, which were used for G determination of the sample in the cavity method and $tan\,\delta$ losses of the Teflon sheet in the parallel plate resonator method.

Because the parallel plate method is very convenient for thin film characterization, it is widely used by many thin film groups. Results are sometimes used to compare different thin film preparation techniques. Application to very low R_s films may go beyond the

scope of the method. As a study of the importance of calibration, the surface resistance calculation program [24] has been used to evaluate the niobium surface resistance at 12 GHz and at 4 K. The result suggests the calibration standard used in ref. [51] was one of the best results for niobium samples, indicating possible over-evaluated $tan\,\delta$ losses in the experiment (an error which cannot be checked out from the method itself). Moreover, this also suggests that one has to be careful when comparing parallel plate methods between two labs, let alone comparing the thin films and their preparation methods.

5.2.5 Limiting Factors of the Method

There are two limiting factors to the calorimetric measurement. One is the working temperature of 2 K. Besides the difficulty of using superfluid helium, the surface resistance *vs.* temperature characteristics of the high-T_c superconducting materials cannot be measured, missing the important information at the transition region. The other limitation is that it is not effective for samples whose surface resistance is extremely small at low fields and increases dramatically at moderate field levels.

5.3 Conclusions

1. A 1.5 GHz triaxial cavity has been successfully designed, fabricated, and tested. It has a compact size, a minimal edge effect for a 25.4 mm or larger diameter sample, and small losses for the indium seal joint. The major specifications have been achieved.

2. A highly sensitive calorimetry method has been implemented to measure the RF losses of the test sample. The accuracy, for the present, is limited by the RF field measurement. The measured losses exclude other extrinsic losses like indium joint losses, edge losses, etc.

3. Two high-T_c superconducting samples have been measured. One sample has an excellent residual resistance value of 35.2 $\mu\Omega$, which was achieved in a large area sample. The second

one was 0.17 Ω, which was related to its long history of different measurements and a large number of visible shiny spots.

4. Anomalous effects such as field emission and multipacting phenomena were observed during calorimetric measurements, confirming that the calorimetric measurement is a useful tool to study these field-limiting phenomena quantitively.

5. Ultralow surface resistance could be measured with the triaxial cavity. Different top plates, which are made with different materials and processed with different chemical treatment methods, can be studied with this extremely sensitive and accurate measurement method.

6. Although excellent surface resistance values have been reported by many groups, no values at low frequencies have ever been reported for large area epitaxially grown thin film samples. In the past, this was limited by existing measurement techniques. This will not be a problem in the future. Further experiments with this cavity will contribute to the understanding of the residual resistance of the high-T_c superconductors and shed light on the popularly used f^2 scaling law.

7. The calorimetric measurement results will provide extremely useful information for device development and application.

Appendix A: URMEL Output

The following six pages are the URMEL input of the triaxial cavity, its mesh division, output table, and the resonant frequencies of some azimuthally symmetric and azimuthally asymmetric modes.

The URMEL input of the triaxial cavity

```
 $FILE ITEST=0, LPLO=.T. $END
Coaxline cavity with taper end
 $BOUN $END
 $MESH NPMAX=25000
 ISTEPZ(1)=4
 ISTEPZ(2)=56
 ISTEPZ(3)=30
 ISTEPR(1)=16
 ISTEPR(2)=16
 ISTEPR(3)=8
 ISTEPR(4)=48
 ISTEPR(5)=12
 ISTEPR(6)=25 $END
 $CAVITYSHAPE
0.0
0.0      0.0
0.05     0.0
0.05     0.05
0.025    0.05
0.025    0.035
0.01     0.001
0.008    0.001
0.022    0.035
0.004    0.035
0.004    0.001
0.0      0.001
0.0      0.0
9999     9999
 $MODE MROT=0 $END
 $PLOT NPLOT=60,NARROW=400,LMECI=.T.,MODPL=2 $END
 $PRIN MODPR=2,LHFI=.T.,LER=.F.,
 LEZ=.T.,LEFI=.F.,LHR=.T. $END
```

Mesh division of the triaxial cavity

TEXT:Coaxline cavity with taper end
PLOT:MESH + CAVITY INPUT ; ID:LIANG 15-MAR9311:33:19

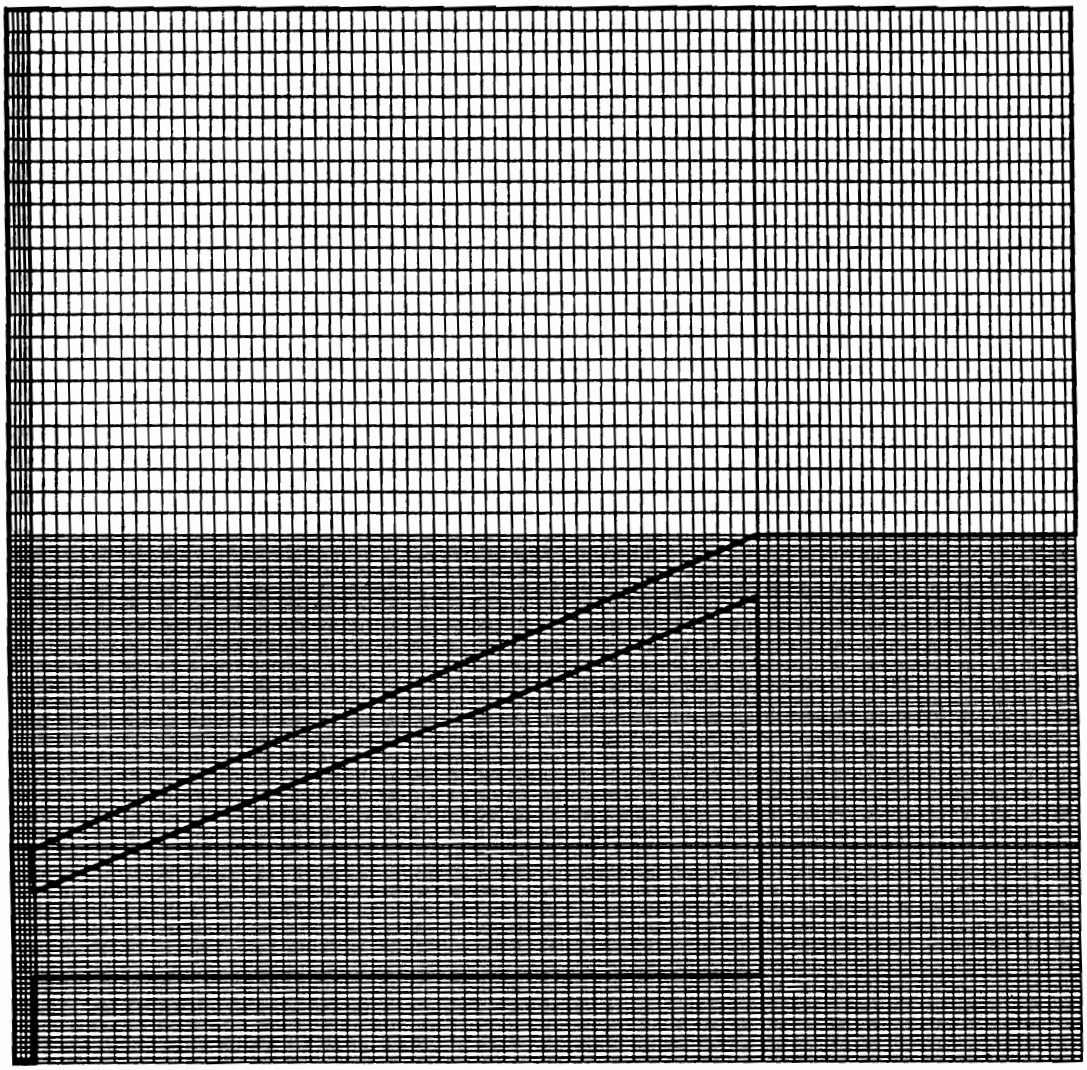

The output table of URMEL

```
++++++++++++++++++++++++++++++++++++++++++++++++++++++++
++++++++++++++++++++++++++++++++++++++++++++++++++++++++
++ RESULTS FOR THE ACTUAL CAVITY AS INPUT TO URMEL ++
++ ***** NOT ASSUMING ANY HALF CELL SYMMETRY ***** ++
++++++++++++++++++++++++++++++++++++++++++++++++++++++++
++ MODE TYPE                    =   TM0-EE-  2          ++
++ FREQUENCY                    =   1461.876      MHZ   ++
++ FREQUENCY/CUT-OFF FREQU. =  0.3185124E-02          ++
++ WAVE LENGTH OF MODE          =  0.2050737      M     ++
++ BEAM PIPE CUTOFF TM-MODE =   458970.1      MHZ   ++
++++++++++++++++++++++++++++++++++++++++++++++++++++++++
++ PARTICLE SPEED B (B=BETA)=   1.000000      C0    ++
++ INT.(     EZ            )DZ=  -2872.711      V     ++
++ INT.(     EZ*COS(K*Z/B))DZ=  -2872.268      V     ++
++ INT.(     EZ*SIN(K*Z/B))DZ=  -44.00490      V     ++
++ TOTAL STORED FIELD ENERGY=  0.9538529E-05 VAS   ++
++ K0        (=V*V/4*ENERGY) =  0.2162771      V/PC  ++
++ VOLTAGE TAKEN AT      R0  =  0.0000000E+00 M     ++
++ SKIN DEPTH                   =  0.1728426E-05 M     ++
++ Q WITH ALL END PLATES        =      4350            ++
++ Q WITHOUT LEFT  END PLATE=      4403            ++
++ Q WITHOUT RIGHT END PLATE=      4374            ++
++ Q WITHOUT BOTH END PLATES=      4427            ++
++ P WITH ALL END PLATES        =   20.13714      W     ++
++ P WITHOUT LEFT  END PLATE=   19.89830      W     ++
++ P WITHOUT RIGHT END PLATE=   20.02772      W     ++
++ P WITHOUT BOTH END PLATES=   19.78888      W     ++
++++++++++++++++++++++++++++++++++++++++++++++++++++++++
++++++++++++++++++++++++++++++++++++++++++++++++++++++++

++++++++++++++++++++++++++++++++++++++++++++++++++++++++
++++++++++++++++++++++++++++++++++++++++++++++++++++++++
++ FULL CELL RESULTS  -  ASSUMING P=V*V/2/RS  AND  ++
++ THAT THE INPUT IS THE RIGHT HALF OF A FULL CELL ++
++++++++++++++++++++++++++++++++++++++++++++++++++++++++
++ FREQUENCY                    =   1461.876      MHZ   ++
++ FREQUENCY/CUT OFF FREQU. =  0.3185124E-02          ++
++ VOLTAGE TAKEN AT      R0  =  0.0000000E+00 M     ++
++ K0        (=V*V/4*ENERGY) =  0.4324527      V/PC  ++
++ SHUNT IMPEDANCE AT R=R0  =  0.4168971      MOHM  ++
++ R/Q              AT R=R0  =   94.16253      OHM   ++
++ Q WITHOUT END PLATES         =      4427            ++
++ PEAK SURFACE E FIELD AT R=  0.3875000E-02 M     ++
++                      AND Z=  0.8750001E-03 M     ++
++ PEAK FIELD STRENGTH THERE=   3510007.      V/M   ++
++ RATIO PEAK/EFFECITVE         =   61.10165            ++
++ PEAK SURFACE H FIELD AT R=  0.4125000E-02 M     ++
++                      AND Z=  0.3469643E-01 M     ++
++ PEAK FIELD STRENGTH THERE=   2059.002      A/M   ++
++++++++++++++++++++++++++++++++++++++++++++++++++++++++
++++++++++++++++++++++++++++++++++++++++++++++++++++++++

RELATIVE ERROR OF THE MAXWELLIAN CURL LAWS: 3.4E-02
RELATIVE ERROR OF MAXWELLS LAW  <DIV(D)=0>: 4.0E-06
```

Azimuthally symmetric modes, ROT = 0

SUMMARY OF ALL MODES FOUND (FULL CELL RESULTS)

(VOLTAGE INTEGRATED AT R0= 0.000 METER OFF AXIS)

MODE TYPE	FREQUENCY / MHZ	(R/Q)/OHM AT R0	ACCURACY	CONTAMINATION
TM0-EE- 1	736.331848	******	2.6E-01	2.212917
TM0-EE- 2	1461.876465	94.163	3.8E-02	0.908829
TM0-EE- 3	2984.200684	1.041	1.3E-02	0.206963
TM0-EE- 4	4591.237793	2.229	3.0E-03	0.069107
TM0-EE- 5	5462.044922	13.469	2.8E-03	0.144414
TM0-EE- 6	5945.676758	0.280	2.7E-03	0.208441
TM0-EE- 7	6321.849609	0.003	1.9E-03	0.183750
TM0-EE- 8	7637.681152	0.156	1.2E-03	0.039074
TM0-EE- 9	8748.098633	0.866	5.1E-02	5.754519
TM0-EE- 10	9109.480469	0.145	9.5E-02	10.000000
TM0-EE- 11	9334.096680	******	1.1E-01	10.000000
TM0-EE- 12	10044.455078	1.257	3.0E-02	2.283204
TM0-EE- 13	11200.660156	******	1.3E-01	10.000000
TM0-EE- 14	11805.215820	0.071	9.7E-02	9.927246
TM0-EE- 15	12818.892578	******	1.2E-01	7.390306

Azimuthally asymmetric modes, ROT = 1

SUMMARY OF ALL MODES FOUND (FULL CELL RESULTS)

(VOLTAGE INTEGRATED AT R0= 0.001 METER OFF AXIS)

MODE TYPE	FREQUENCY (MHZ)	(R/Q) (OHM AT R0)	(R/Q)/(K*R0)**2M (OHM)	ACCURACY	CONTAMINATION
1-EE- 1	3065.831055	0.000	0.316	1.8E-03	0.026917
1-EE- 2	4366.009766	0.002	0.756	4.8E-04	0.009762
1-EE- 3	5516.249023	0.002	0.546	8.4E-04	0.032641
1-EE- 4	6159.097168	0.000	0.044	3.7E-04	0.053977
1-EE- 5	6357.871094	0.000	0.002	1.5E-03	0.314767
1-EE- 6	6503.851074	0.000	0.001	1.1E-03	0.251000
1-EE- 7	6959.291992	0.010	1.064	1.3E-03	0.106120
1-EE- 8	7944.545410	0.001	0.099	9.7E-04	0.142830
1-EE- 9	8195.243164	0.000	0.003	5.9E-04	0.102679
1-EE- 10	8887.578125	0.000	0.004	8.2E-04	0.153996
1-EE- 11	9113.327148	0.000	0.010	2.0E-03	0.431452
1-EE- 12	9861.559570	0.042	3.935	2.7E-03	0.518270
1-EE- 13	10111.335938	0.001	0.000	4.5E-03	0.949570
1-EE- 14	10633.265625	0.000	0.000	4.2E-03	0.448266
1-EE- 15	11326.253906	0.001	0.047	2.7E-02	2.144697

Azimuthally asymmetric modes, ROT = 2

SUMMARY OF ALL MODES FOUND (FULL CELL RESULTS)

(VOLTAGE INTEGRATED AT R0= 0.000 METER OFF AXIS)

ROT = 2 (2np modes)

MODE TYPE	FREQUENCY (MHZ)	(R/Q) (OHM AT R0)	(R/Q)/(K*R0)**2M (OHM)	ACCURACY	CONTAMINATION
2-EE- 1	3957.053467	0.000	0.008	1.1E-02	0.183667
2-EE- 2	5386.011236	0.000	0.018	6.3E-03	0.147376
2-EE- 3	6420.913086	0.000	0.005	4.3E-03	0.311024
2-EE- 4	6825.152344	0.000	0.002	2.9E-03	0.592965
2-EE- 5	6984.218750	0.000	0.004	2.4E-03	0.573812
2-EE- 6	8056.069336	0.000	0.034	4.1E-03	0.273545
2-EE- 7	8617.306641	0.000	0.006	2.7E-03	0.215180
2-EE- 8	9170.817383	0.000	0.016	9.8E-03	1.569670
2-EE- 9	9456.483398	0.000	0.000	1.1E-02	1.985775
2-EE- 10	10155.692383	0.000	0.044	5.9E-03	1.103353
2-EE- 11	10417.552734	0.000	0.009	4.1E-02	8.466126
2-EE- 12	10961.606445	0.000	0.008	1.5E-02	1.601833
2-EE- 13	11787.552734	0.000	0.006	2.2E-02	1.606778
2-EE- 14	12610.565436	0.000	0.001	4.6E-02	3.772539
2-EE- 15	13354.750000	0.000	0.000	4.6E-02	4.028659

Appendix B: Fabrication of RF Coupling Probes

Because this thesis was started from scratch, there were many little pieces of designing and machining work, such as the fabrication of the stainless steel RF coupling probes, the design of the probe adjustment assembly, the preparation of the carbon resistor temperature sensors, etc. As an example, the design and fabrication of the stainless steel coupling probes are described in the following.

When the coupling probe is adjusted up and down, it has to be self-aligning and compatible with ultrahigh vacuum. Therefore, a stainless steel tube and a center conductor were used to make the transmission line for the coupling probe, instead of the commonly-used semi-rigid cable. To design the transmission line, the following formula is used:

$$Z_0 = \frac{138}{\sqrt{\varepsilon}} log_{10} \frac{D}{d} \tag{7.1}$$

A 0.156″ OD, 0.016″ wall thickness stainless steel tube was used as the outer conductor and a 0.062″ ϕ stainless wire was used as the center conductor. The characteristic impedance is 41.5 Ω when the medium is vacuum.

The self-aligning feature is accomplished by making eight spring fingers to have spring contact with the inner Nb wall, which also provides electrical contact with the niobium tube. The spring contact was made using the following procedures (the unit used in this appendix is the *inch*):

— Made eight 0.50″ long, 0.010″ wide slits starting from a point 0.50″ from the end;

— To electropolish the stainless steel tube end, a polyethelene round rod was used to hold the stainless steel tube (the anode) and a copper tube (the cathode) which helps to obtain the uniformity required for the stainless steel tube. A hole was drilled in the center of the polyethelene rod for the SS tube, and several other small holes were drilled for gas release. The OD of the polyethelene piece was a little smaller than the ID of the copper tube (about 1″) and was clamped into the copper tube. The stainless steel tube and the copper tube together form a coaxial line shape. The copper tube was used as the cathode and the stainless steel tube as the anode. The polished length is about 1″. The electropolishing solution used was 75% H_3PO_4 + 25% H_2O. The current density was 0.75 A/cm^2, and the etching rate was 0.008″/hr. After one hour of etching, the wall thickness left was 0.008″. The finish was very shiny and uniform;

— Used tweezers to pull out the thinned part, which made a very good spring contact;

— Cut the tube to leave a 0.38″ long stub, which was bent to form the loop. It was soldered to the center stainless steel rod.

The other end of the tube and a welded stainless steel bellows was brazed to an adapting stainless steel piece. An SMA connector, after being welded to the center rod, was also welded to the adapting piece.

Appendix C: Example of a LabVIEW Program — "Take Raw"

This is the VI (Virtual Instrument) which accomplishes the data acquisition. As shown in the next three pages, **"Take Raw"** is the VI developed for data acquisition of the calorimetric measurement; other VIs in the hierarchy are ready-to-use VIs in LabVIEW. The *Connector Pane* shows the eight inputs and two outputs and serves as the interface of the VI. The *Front Panel* shows all the controls – inputs and outputs. The *Block Diagram* consists of three successive loops. The counter is reset to zero and ready to count in the first loop. Scanning channels, sequence, and their gains are defined by **SCAN_Setup** in loop 2. Calibration or sense mode is also defined. Data acquisition is accomplished by **SCAN_Op** in loop 3.

The VI "Take Raw" has eight inputs and two outputs. All of them are required by **SCAN_Setup** and **SCAN_Op** except a binary switch called "calib/sense". The switch selects between two different measurements: TRUE for 4 reference resistor measurements

and FALSE for 16 mapping resistor measurements. The other nine controls and outputs are self-explanatory. The inputs are *board number, time base, gain for four channels, and total number of acquisitions N.* The outputs are *scan output and acquisition error.*

The scan output of the VI is a two dimensional array $4 \times (N/4)$. The sequence is determined by the setup loop and is as shown:

$$\begin{pmatrix} V1 & V1 & -V1 & -V1 & V2 & V2 & -V2 & -V2 & \dots & V1 & V1 & \dots \\ V5 & V5 & -V5 & -V5 & V6 & V6 & -V6 & -V6 & \dots & V5 & V5 & \dots \\ V9 & V9 & -V9 & -V9 & V10 & V10 & -V10 & -V10 & \dots & V9 & V9 & \dots \\ V13 & V13 & -V13 & -V13 & V14 & V14 & -V14 & -V14 & \dots & V13 & V13 & \dots \end{pmatrix}$$

It will be processed in the following VI **Cook**.

Take therm raw data
Monday, August 31, 1992 11:00 AM

Page 1 

Position in hierarchy

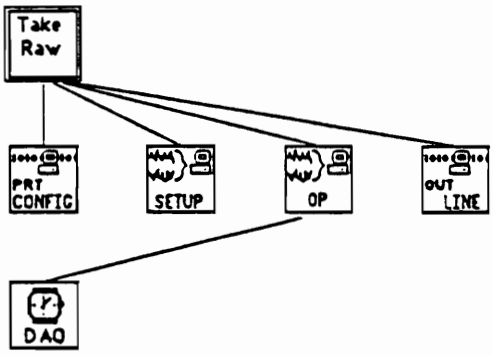

Connector Pane

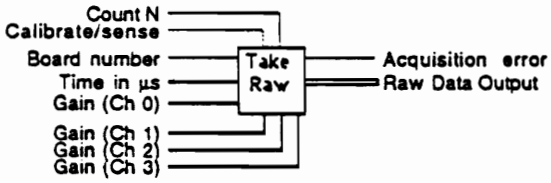

Take therm raw data

Front Panel

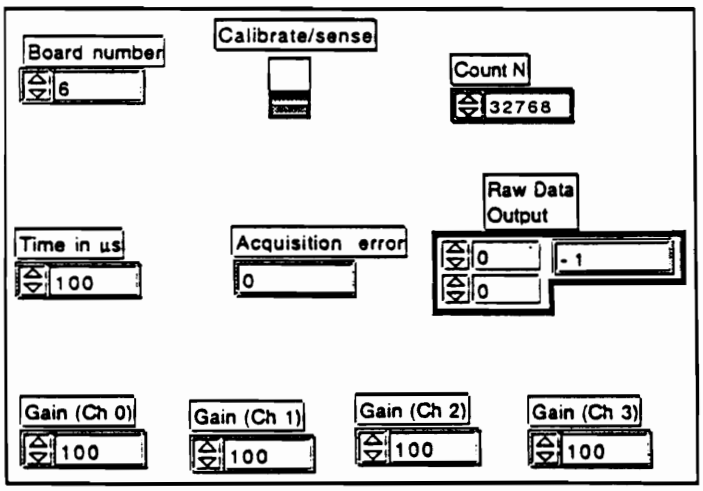

Block Diagram

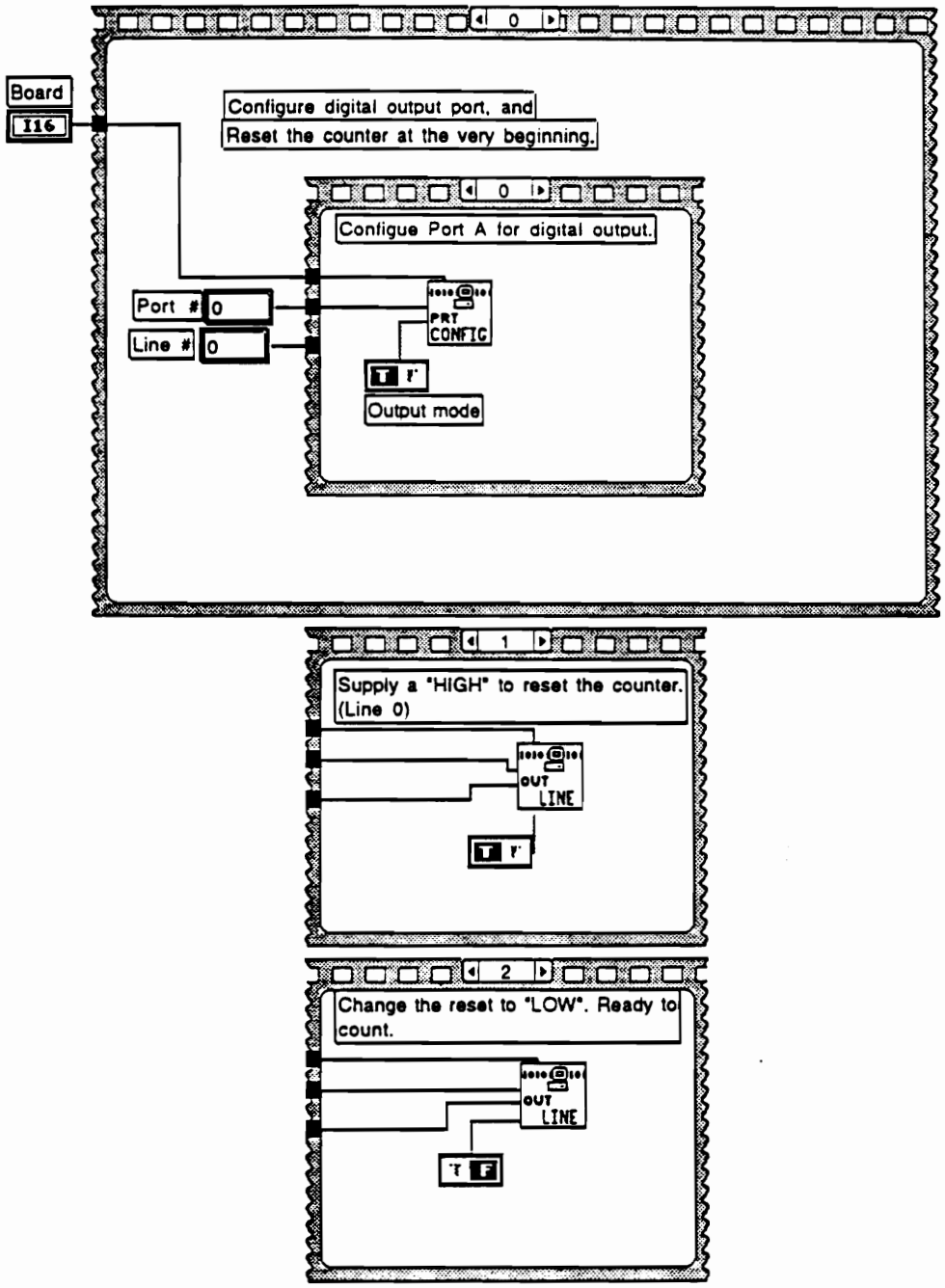

Take therm raw data
Monday, August 31, 1992 11:00 AM

Page 3 Take Raw

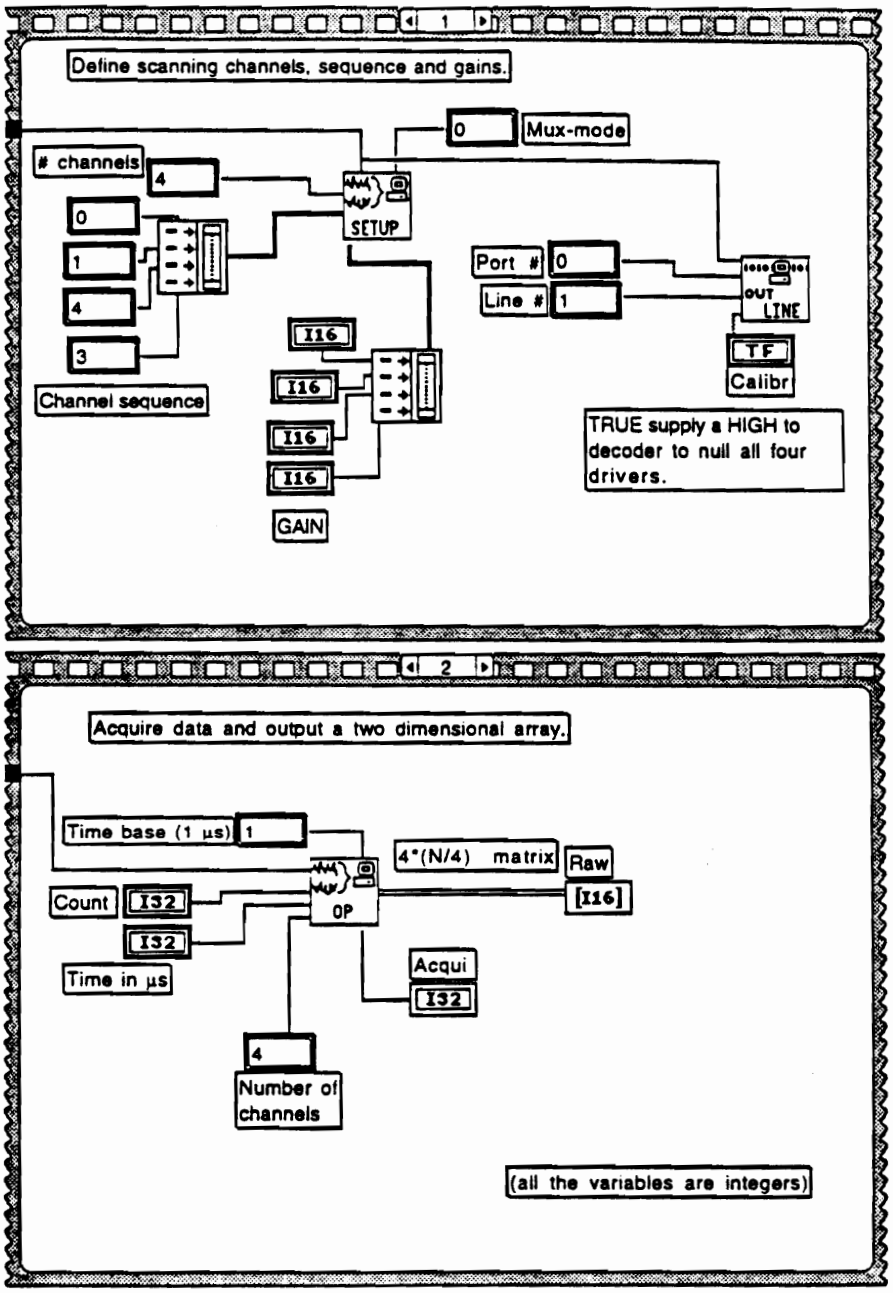

Bibliography

[1] C. K. Sinclair, *Proceedings of 1992 Linear Accelerator Conference* ed. by C. R. Hoffmann, p. 3.

[2] J. Bednorz, and K. Müller, *Z. Phys. B* **64**, 189 (1986).

[3] S. Ramo, J. R. Whinnery, and T. Van Duzer, *Fields and Waves in Communication Electronics* (Wiley, New York) 2nd ed. (1984).

[4] J. Jackson, *Classical Electrodynamics* (Wiley, New York) 2nd ed. (1975).

[5] N. Klein, H. Chaloupka, G. Müller, S. Orbach, H. Piel, B. Roas, L. Schultz, U. Klein, and M. Peiniger, *J. Appl. Phys.* **67**, 6940 (1990).

[6] H. Piel, *WUB 86-14*, Univ. Wuppertal (1986).

[7] A. B. Pippard, *IEEE Tans.* **MAG-23**, 371 (1987).

[8] J. M. Ziman, *Theory of Solids* (Cambridge University Press, Cambridge) paperback ed. (1979) p. 282 - 287.

[9] T. Van Duzer, and C. W. Turner *Principle of Superconductive Devices and Circuits* (Elsevier North Holland, New York, 1981) p.94 - 138.

[10] H. Kamerlingh Onnes, *Leiden Comm.* Univ. Leyden, Nos. 120b, 122b, 124c (1911).

[11] W. Meissner, and R Ocshenfeld, *Naturwissenschaften* **21**, 787 (1933).

[12] F. London, and H. London, *Proc. Roy. Soc. (London)* **A149**, 71 (1935).

[13] C. J. Gorter, H. B. G. Casimir, *Z. Phys.* **35**, 963 (1934).

[14] V. L. Ginzburg, L. D. Landau, *JETP* **20**, 1064 (1950).

[15] C. A. Reynolds, B. Serin, W. H. Wright, L. B. Nesbitt, *Phys. Rev.* **78**, 487 (1950); E. Maxwell, *Phys. Rev.* **78**, 477 (1950).

[16] J. Bardeen, L. N. Cooper, R. Schrieffer, *Phys. Rev.* **108**, 1175 (1957).

[17] M. K. Wu, J. R. Ashburn, C. J. Tong, P. H. Hor, R. L. Meng, L. Gao, Z. J. Huang, Y. Q. Wang, and C. W. Chu, *Phys. Rev. Lett.* **58**, 908 (1987).

[18] J. K. Hulm, J. E. Kunzler, and B. T. Matthias, *Phys. Today* **34**, 34 (1981).

[19] A. A. Abrikosov *Soviet Phys. — JETP* **5**, 1174 (1957).

[20] B. D. Josephson, *Phys. Lett.* **1**, 251 (1962).

[21] P. B. Wilson, and H. A. Schwettman, *IEEE Trans. Nucl. Sci.* **12**, 1045 (1965).

[22] H. Langer, *Proceedings of of the Second Workshop on RF-Superconductivity*, (1984); K. W. Shepard, *Proceedings of of the Third Workshop on RF-Superconductivity*, ANL-PHY-88-1 (1988).

[23] D. C. Mattis, and J. Bardeen, *Phys. Rev.* **111**, 412 (1958).

[24] J. Halbritter, *Z. Phys.* **266**, 209 (1974);
J. P. Turneaure, Ph. D. Thesis, Stanford University (1967).

[25] C. Lyneis, Ph. D. Thesis, Stanford University (1973).

[26] W. H. Hartwig, and C. Passow, in *Applied Superconductivity*, vol. 2, (Academic Press, New York), ed. Newhouse, (1975).

[27] R. G. De Gennes, *Superconductivity of Metals and Alloys* (Benjamin, New York, 1966).

[28] B. Piosczyk, P. Kneisel, O. Stoltz, J. Halbritter, *IEEE Trans.* **NS-20**, 108 (1973).

[29] M. Beasley, *Proceeding of the IEEE* **77**, 1155 (1989).

[30] H. Piel, and G. Müller *IEEE Trans.* **MAG-27**, 854 (1991);
G. Müller, *Proceedings of the Fourth Workshop on RF Superconductivity* ed. by Y. Kojima, KEK Report 89-21, p. 267;
N. Klien, *Proceedings of the Fifth Workshop on RF Superconductivity* ed. by D. Proch, DESY Report 91-M02, p. 285.

[31] A. Inam, X. D. Wu, L. Nazar, M. S. Hedge, C. T. Rogers, T. Venkatesan, R. W. Simon, K. Daly, H. Padamsee, J. Kirchgessner, D. Moffat, D. Rubin, Q. S. Shu, D. Kalokitis, A. Fathy, V. Pendrick, R. Brown, B. Brycki, E. Belohoubek, L. Drabeck, G. Gruner, R. Hammond, R. Gamble, B. M. Lairson, and J. C. Bravman, *Appl. Phys. Lett.* **56**, 1178 (1990);
N. Newman, K. Char, S. M. Garrison, and R. W. Barton, R. C. Taber, C. B. Eom, T. H. Geballe, and B. Wilkens, *Appl. Phys. Lett.* **57**, 520 (1990);
W. J. DeSisto, R. L. Henry, H. S. Newman, M. S. Osofsky, and V. C. Cestone, *Apll. Phys. Lett.* **60**, 2926 (1992);
W. L. Holstein, L.A. Parisi, C. Wilker, and R. B. Flippen, *Appl. Phys. Lett.* **60**, 2014 (1992);
A. Mogro-Campero, L. G. Turner, A. M. Kadin, and D. S. Mallory, *Appl. Phys. Lett.* **60**, 3310 (1992).

[32] D. L. Rubin, J. Gruschus, J. Kirchgessner, D. Moffat, H. Padamsee, J. Sears, Q. S. Shu, S. Tholen, E. Wilkins, R. Buhrman, S. Russek, and T. W. Noh, *Proceedings of the Third Workshop on RF - Superconductivity* ANL-PHY-88-1, ed. K. W. Shepard, p. 211 - 227 (1988).

[33] N. Klein, U. Dähne, U. Poppe, N. Tellmann, K. Urban, S. Orbach, S. Henson, G. Müller, and H. Piel, *J. Supercon.* **5**, 195 (1992).

[34] J. Halbritter, *Z. Phys.* **238**, 466 (1970).

[35] J. R. Delayen, C. L. Bohn, and C. T. Roche, *J. Supercon.* **3**, 243, (1990).

[36] H. Padamsee, J. Kirchgessner, D. Moffat, D. L. Rubin, J. Sears, and Q. S. Shu, *J. Appl. Phys.* **67**, 2003 (1989);
M. Hein, G. Müller, H. Piel, L. Ponto, M. Becks, U. Klein, and M. Peiniger, *J. Appl. Phys.* **66**, 5940 (1989).

[37] I.S. Gergis, J. T. Cheung, T. N. Trinh, E. A. Sovero, and P. H. Kobrin, *Appl. Phys. Lett.* **60**, 2026 (1992).

[38] J. M. Laurent, and H. Padamsee, *CERN/EF/RF 83-2* (1983).

[39] G. A. Loew, *SLAC-TN-68-25* (1968).

[40] T. Weiland, *IEEE Trans. Nucl. Sci.* **NS-32**, 2738 (1985).

[41] S. Sridhar, and W. Kennedy, *Rev. Sci. Instrum.* **59**, 531 (1988);
D. L. Rubin, K. Green, J. Gruschus, J. Kirchgessner, D. Moffat, H. Padamsee, J. Sears, and Q. S. Shu, *Phys. Rev. B* **38**, 6538 (1988).

[42] L. D. Chang, M. J. Moskowitz, R. B. Hammond, M. M. Eddy, W. L. Olson, D. D. Casavant, E. J. Smith, and M. Robinson, L. Drabeck, and G. Grüner, *Appl. Phys. Lett.* **55**, 1357 (1989).

[43] G. Müller, M. Hein, N. Klein, H. Piel, L. Ponto, U. Klein, and M. Peiniger, *Proc. of the European Particle Acc. Conf.* (World Scientific Pub., 1989) ed. S. Tazzari, p. 40.

[44] J. P. Carini, A. M. Awasthi, W. Beyermann, G. Grüner, T. Hylton, K. Char, M. R. Beasley, and A. Kapitulnik, *Phys. Re. B* **37**, 9726 (1988).

[45] C. Zahopoulos, W. L. Kennedy, and S. Sridhar, *Appl. Phys. Lett.* **52**, 2168 (1988);
T. W. Button, and N. McN. Alford, *Appl. Phys. Lett.* **60**, 1378 (1992).

[46] J. R. Delayen, C. L. Bohn, and C. T. Roche, *Rev. Sci. Instrum.* **61**, 2207 (1990).

[47] F. A. Miranda, W. L. Gordon, K. B. Bhasin, and J. D. Warner, *Appl. Phys. Lett.* **57**, 1058 (1990).

[48] J. A. Greer, J. Vac. Sci. Technol. A **10**, 1821 (1992).

[49] D. A. Bonn, D. C. Morgan, and W. N. Hardy, *Rev. Sci. Instrum.* **62**, 1819 (1991).

[50] H. Y. To, G. J. Valco, and K. B. Bhasin, *Supercond. Sci. Technol.* **5**, 421 (1992).

[51] R. C. Taber, *Rev. Sci. Instrum. 61*, 2200 (1990).

[52] P. Kneisel, G. Müller, C. Reece, *IEEE Trans.* **Mag-23**, 1417 (1987).

[53] K. Krafft, Ph. D. Thesis, Cornell University (1983).

[54] J. P. Budliger, and A. Laisne, *Nucl. Instrum. and Methods* **61**, 253 (1968).

[55] C. Reece, J. Susta, T. Powers, B. Almeida, *1991 IEEE Particle Accelerator Conference* **4**, 2325, (1991).

[56] R. Romijn, W. Weigarten, and H. Piel, *IEEE Trans.* **MAG-19**, 1318 (1983).

[57] L. Allen, Ph. D. Thesis, Stanford University (1987).

[58] W. L. Johnson, and A. C. Anderson, *Rev. Sci. Instrum.* **42**, 1296 (1971).

Vita

Changnian Liang was born on June 27, 1964, in Nanchang, Jiangxi, People's Republic of China, two years before the Great Cultural Revolution. In 1968, his parents were sent to countryside to have their "re-education", or "brain-washing". The re-education ended in 1974, when Changnian moved with his parents to Jinxian, Jiang Xi, where his family has lived since then. Without much work to do, his father chose to teach him at home. This was at the time when the illiterates were the most glorious and the intellectuals were the most reactionary, and all subjects were nearly abandoned in school. After Chairman Mao passed away in 1976, China started to restore her higher education in 1977. In 1978, Changnian left his parents and spent his last high school year at The First Middle School of Changsha, Hunan. In 1979, he entered Peking University, Beijing, which has been a hotbed of student movement since 1919. In 1983, he received his B.S. degree in physics, and continued to study for his master's degree. In 1986, he received his M.S. degree in physics from Peking University, and entered Virginia Polytechnic Institute and State University for his Ph.D. program. In 1987, he was introduced to his thesis advisor Ronald Sundelin by Luke W. Mo, and started his thesis research at CEBAF, the Continuous Electron Beam Accelerator Facility, which was just beginning to be built in Newport News, Virginia. He was married with Gebi Lin in 1991, and received his Ph.D degree in physics from Virginia Polytechnic Institute and State University in May, 1993.

Changnian Liang

梁昌年